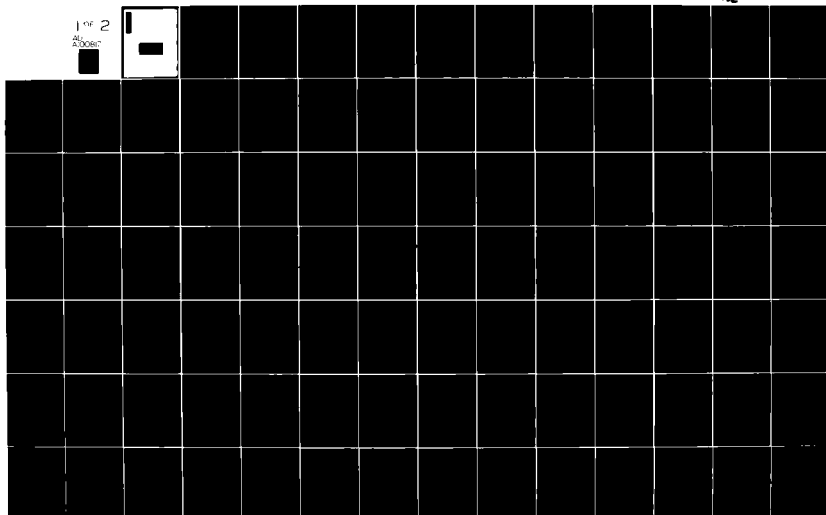


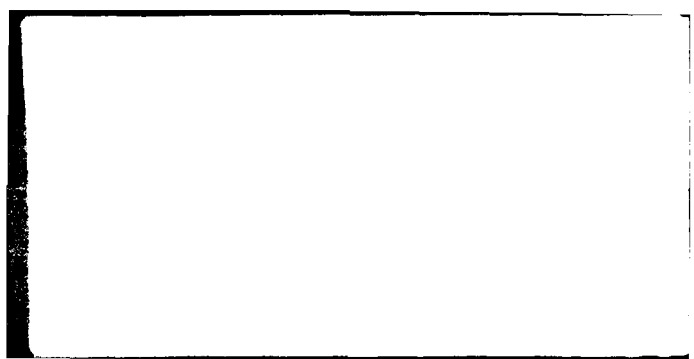
AD-A100 817 AIR FORCE INST OF TECH WRIGHT-PATTERSON AFB OH SCHOO--ETC F/6 20/4
NAVIER-STOKES SOLUTIONS FOR A SUPERSONIC COFLOWING AXISYMETRIC --ETC(U)
APR 81 G A HASEN

UNCLASSIFIED AFIT/DS/AA/81-2

NL

Inf 2
20
Scale





Accession For	
NTIS GRA&I	<input checked="" type="checkbox"/>
DTIC TAB	<input type="checkbox"/>
Unannounced	<input type="checkbox"/>
Justification	
By	
Distribution/	
Availability Codes	
Avail and/or	
Dist	Special
A	

NAVIER-STOKES SOLUTIONS FOR A SUPERSONIC
 COFLOWING AXISYMMETRIC NOZZLE WITH A
 THICK BASE ANNULUS

DISSERTATION

AFIT/DS/AA/81-2'

Gerald Hasen
 Capt USAF

DTIC
 ELECTED
 JUL 1 1981
 S D

Approved for public release; distribution unlimited

AFIT/DS/AA/81-2

NAVIER-STOKES SOLUTIONS FOR A SUPERSONIC
COFLOWING AXISYMMETRIC NOZZLE WITH A
THICK BASE ANNULUS

DISSERTATION

Presented to the Faculty of the School of Engineering
of the Air Force Institute of Technology
Air University
in Partial Fulfillment of the
Requirements for the Degree of
Doctor of Philosophy

by

Gerald A. Hasen, B.S., M.S.

Captain USAF

Approved for public release; distribution unlimited

NAVIER-STOKES SOLUTIONS FOR A SUPERSONIC
COFLOWING AXISYMMETRIC NOZZLE WITH A
THICK BASE ANNULUS

by

Gerald A. Hasen, B.S., M.S.

Captain USAF

Approved:

Gerald E. Wright 28 April 81
Chairman

Robert J. Reck 28 April 81

Michael Kyndt 28 Apr 81

Walter L. Honsey 28 Apr. 81

David A. Lee April 28, 1981

Accepted:

J.S. Prezinecki April 28, 1981
Dean, School of Engineering

ACKNOWLEDGEMENTS

This dissertation represents over three years of research conducted while I was assigned first to the Air Force Institute of Technology, and subsequently to the Computational Aerodynamics Group within the Flight Dynamics Laboratory. I wish to take this opportunity to express appreciation to the Air Force for the chance to further my education, and to the Flight Dynamics Laboratory for the outstanding support received while this research was in progress.

I am deeply indebted to my technical advisor, Dr. Wilbur L. Hankey, Jr., for his valuable advice and guidance on a daily basis. His personal interest and constructive criticism were instrumental in bringing this research to completion. Special thanks are also due to Dr. Joseph S. Shang for his guidance with the numerical algorithm portion of this research. Being associated with the members of the Computational Aerodynamics Group has been personally as well as technically rewarding.

Special thanks are extended to the members of the AFIT faculty who have served on my committee. I am indebted to my initial committee chairman, Captain John R. Shea, III, and to his subsequent replacement, Professor Harold E. Wright, for their encouragement and constructive criticism of this work. I also express appreciation to Professor David A. Lee and Captain Robert L. Roach for their guidance and good counsel.

To Miss Valerie Williams, who typed this manuscript, I give thanks for a job well done.

I wish to express my love and my deep gratitude to my wife,

Diane, for her encouragement, patience, and understanding. Her many contributions ranged from typing the rough draft of this manuscript to providing a loving home atmosphere for both myself and our new son, Christopher.

Finally, I thank my God, from whom and through whom are all things, for His direction and loving-kindness during the course of this research effort.

Gerald A. Hasen

April 1981

CONTENTS

	<u>Page</u>
Acknowledgements	iii
List of Figures	vii
List of Tables	x
Notation	xi
Abstract	xv
I. Introduction	1
Background	1
Research Objectives	11
II. Mathematical Description of the Flow Structure	14
Governing Equations	14
Boundary and Initial Conditions	21
III. Numerical Procedure	26
Coordinate System	26
Solution Algorithm	29
Convergence Criteria	39
IV. Boundary and Initial Condition Implementation	43
The Upstream Boundary	43
The Upper Boundary	46
The Downstream Boundary	49
The Centerline	50
The Nozzle Walls	52
Initial Conditions	55
V. Turbulence Modeling	56
Boundary Layer Model	57
Far Wake Model	59
Near Wake Model	61
VI. Numerical Results	69
Experimental Data Base	69
Computational Details	71
Comparison with Experimental Data	79
VII. Conclusions and Recommendations	99

Bibliography	103
Appendix A: Nozzle Wall Temperature Calculation.	107
Appendix B: Adaptive Finite Difference Mesh.	110
Appendix C: Two-Dimensional Flat Plate Far Wake Solution . . .	114
Appendix D: Two-Dimensional Wedge-Flat Plate Near Wake Solution	119
Appendix E: Axisymmetric Coflowing Nozzle Solution Simulating Nozzle Separation ($M_j = 2.60$)	128
Appendix F: Investigation of Numerical Error	132
Vita.	140

LIST OF FIGURES

<u>Figure</u>		<u>Page</u>
1	Shock Structure for a Typical Overexpanded Co-flowing Axisymmetric Nozzle.	5
2	Schematic of a Typical Mach Reflection	6
3	Hodograph Diagram Showing Shock Polar Intersections for Transition from Regular to Mach Reflection	8
4	Viscous Effects on the Mach Disc Structure	10
5	Schematic of the Axisymmetric Coflowing Jet Model Used as a Basis for the Computational Solutions.	12
6	Physical Domain for the Computational Solutions.	22
7	Finite Difference Mesh in Physical Space	28
8	Exponentially Stretched Mesh Schematic	28
9	Adaptive Finite Difference Mesh, $P_j/P_\infty = 0.150$	30
10	Computational Mesh in the Transformed Plane.	30
11	Graphical Representation of the Numerical Sweep Operators.	34
12	Base Pressure Tap Location in the Flowfield.	41
13	Typical Base Pressure Convergence, $P_j/P_\infty = 0.527$	42
14	Flowfield Schematic for a Supersonic Coflowing Axisymmetric Nozzle.	44
15	Computed Static Pressure Variation Along the Ogive Body Using a Parabolized Navier-Stokes Solver (23) . .	45
16	Upper Boundary Condition Schematic	48
17	Finite Difference Mesh Near the Nozzle Walls	54
18	Eddy Viscosity Model Domains	58
19	Eddy Viscosity Distribution Across a Boundary Layer. .	58
20	Typical Vorticity Profile Used to Compute Mixing Layer Thickness.	62

21	Maximum Velocity Defect vs Distance Behind the Trailing Edge of a Two-Dimensional Flat Plate, $M_\infty = 1.60$	63
22	Viscous Layer Structure in the Near Wake	64
23	Computed Nozzle Base Pressure vs the Position of the Mixing Region Midpoint X_m	67
24	Computed Mixing Layer Thickness Used in the Wake Turbulence Model for the Wedge-Flat Plate Case.	68
25	Adaptive Finite Difference Mesh, $P_j/P_\infty = 0.527$	72
26	Error in Computed Velocity Gradient vs Grid Coarseness for a Turbulent Boundary Layer	75
27	Axisymmetric Coflowing Nozzle Solution, $P_j/P_\infty = 0.150$. . .	81
28	Axisymmetric Coflowing Nozzle Solution, $P_j/P_\infty = 0.251$. . .	82
29	Axisymmetric Coflowing Nozzle Solution, $P_j/P_\infty = 0.527$. . .	83
30	Axisymmetric Coflowing Nozzle Solution, $P_j/P_\infty = 1.03$. . .	84
31	Axisymmetric Coflowing Nozzle Solution, $P_j/P_\infty = 1.59$. . .	85
32	Computed Mach Number Contours in the Region Near the Shock Reflection at the Centerline	86
33	Computed Velocity Profiles, $P_j/P_\infty = 0.150$	88
34	Computed Velocity Fields in the Near Wake Region of the Coflowing Nozzle.	89
35	Position of the Dividing Streamline in the Computational Coflowing Nozzle Solutions	90
36	Axial Variation in Computed Centerline Mach Number, $P_j/P_\infty = 0.150$	92
37	Shock Reflection Lengths Along the Nozzle Centerline vs Nozzle Pressure Ratio	93
38	Base Pressure Coefficient vs Nozzle Pressure Ratio . . .	96
39	Schlieren Photographs (16) Showing the Eventual Deterioration of the Mach Disc with Decreasing Nozzle Pressure Ratio	97
40	Heat Flux Balance Used to Determine the Nozzle Wall Temperature.	108

41	Adaptive Mesh Schematic.	112
42	Velocity Profile at the Trailing Edge of the Two-Dimensional Flat Plate	116
43	Computational Mesh Used in the Flat Plate Solution . . .	117
44	Computed Flat Plate Velocity Profiles.	117
45	Computational Boundary Conditions for the Two-Dimensional Wedge-Flat Plate	120
46	Computational Mesh Used for the Two-Dimensional Wedge-Flat Plate Solution.	122
47	Two-Dimensional Wedge-Flat Plate with the Computed Mach Number Contours Shown	124
48	Computed Velocity Profiles in the Near Wake of the Two-Dimensional Wedge-Flat Plate	125
49	Static Pressure Along the Line of Symmetry in the Near Wake of the Two-Dimensional Wedge-Flat Plate	125
50	Pitot Pressure Profiles in the Near Wake of the Two-Dimensional Wedge-Flat Plate (Symbols-Experimental Data (33), Solid Lines - Computational Solution)	126
51	Computed Velocity Profiles Near the Nozzle Annulus for the Separated Flow Simulation.	130
52	Computed Mach Number Contours for the Separated Flow Simulation	131
53	Comparison between the Computational Solution and the Error present in the Continuity Equation, $P_j/P_\infty = 0.150$	135
54	Extension of the Downstream Boundary Showing Computed Mach Number Contours, $P_j/P_\infty = 0.251$	137
55	Extension of the Upper Boundary Showing Computed Mach Number Contours, $P_j/P_\infty = 0.251$	138

LIST OF TABLES

<u>Table</u>		<u>Page</u>
1	Computational Grid Parameters.	73
2	Computational Jet Flow Parameters.	77
3	Comparison Between a 1-D Analysis and the Computational Solution Across the Mach Disc for $P_j/P_\infty = 0.150$	87
4	Comparison of Shock Reflection Lengths	94
5	Comparison of Mach Disc Radii.	94
6	Comparison of Base Pressure Coefficients	95

NOTATION

C	Constant used to obtain exponentially stretched mesh.
C_A	Adaptive mesh constant.
C_f	Local skin friction coefficient, $2\tau_w/\rho_\infty u_\infty^2$.
C_p	Specific heat at constant pressure.
C_v	Specific heat at constant volume.
c	Speed of sound, $\sqrt{\gamma RT}$.
E	Error vector.
e	Energy, $C_v T + (u^2 + v^2)/2$.
F	Flux vector, eqn 2-28.
F_D	Damping vector, eqn 3-30.
f	Primitive flow variable ρ , u , v , or T .
G	Flux vector, eqn 2-28.
G_D	Damping vector, eqn 3-32.
H	Flux vector, eqn 2-28.
H_o	Total Enthalpy, $C_p T + (u^2 + v^2)/2$.
h_i	Convective heat transfer coefficient, Appendix A.
h	Thickness of the two-dimensional wedge-flat plate.
i	Index for grid points in the axial direction.
IL	Total number of grid points in the axial direction.
IW	Number of grid points axially along the nozzle wall.
JL	Total number of grid points in the radial direction.
JWI	Radial index of the inner nozzle wall.
JWO	Radial index of the outer nozzle wall.
j	Index for grid points in the radial direction.
j_o	Exponent parameter equal to 0 or 1 for two-dimensional or axisymmetric flow, respectively.

K	Ratio of radial grid point heights, $r(i,3)/r(i,2)$.
K_o	Initial velocity profile constant in the wake region, eqn 4-30.
k	Thermal conductivity.
L	Length scale.
L_m	Length scale used to generate stretched mesh.
L_η, L_ξ	MacCormack difference operators in the η and ξ directions.
λ	Prandtl turbulent mixing length.
M	Mach number, $(u^2 + v^2)^{1/2}/c$.
P	Static pressure.
P_B	Base pressure.
P_{T_2}	Pitot pressure.
β_B	Base pressure coefficient, $(P_B - P_\infty)/q_\infty$.
Pr	Prandtl number, $\mu C_p/k$.
\vec{q}	Heat flux vector.
\dot{q}_x, \dot{q}_r	Heat flux in the axial and radial directions.
R	Gas constant for air.
Re	Reynolds number, $\rho(u^2 + v^2)^{1/2}L/\mu$.
r	Spatial coordinate normal to the nozzle centerline.
r_m	Mach disc radius.
S	Fluid stress tensor that includes pressure and viscous forces.
T	Absolute temperature.
t	Time.
t_{ch}	Characteristic time, eqn 3-36.
U	Conservative flow variable vector, eqn 2-28.
\vec{u}	Velocity vector.
u	Velocity component along the x axis.
u_{ch}	Characteristic velocity, eqn 3-36.

u^+	Nondimensional velocity component, $u/(\tau_w/\rho)^{1/2}$.
V	Volume.
v	Velocity component along the r axis.
x	Spatial coordinate parallel to the nozzle centerline.
x_r	Mach disc reflection length.
y	Spatial coordinate normal to the x axis in a two-dimensional flow.
y_B	Radial thickness of the nozzle base annulus.
y^+	Nondimensional height, $y(\tau_w/\rho)^{1/2}/v$.

GREEK SYMBOLS:

α_η , α_ξ	Damping coefficients in the η and ξ directions.
γ	Ratio of specific heats, C_p/C_v .
δ	Flow deflection angle, Chapter 1.
δ	Momentum boundary layer thickness.
δ^*	Momentum boundary layer displacement thickness.
δ_{ij}	Kronecker delta, equal to 0 if $i \neq j$ or equal to 1 if $i=j$.
ϵ	Turbulent eddy viscosity coefficient.
η	Transformed coordinate normal to the nozzle centerline.
Δ	Designates a finite difference when used as a prefix.
ϕ	Local flow angle, $\arctan(v/u)$.
χ	Boundary layer momentum thickness, Appendix C.
λ	Viscosity diffusion coefficient, eqn 2-37.
λ_I	Left running characteristic line.
μ	Absolute viscosity coefficient.
μ_M	Mach angle of supersonic flow, eqn 4-1.
ν	Kinematic viscosity, μ/ρ .
ξ	Transformed coordinate parallel to the nozzle centerline.
ρ	Fluid density.

σ Normal stress on an element of fluid, eqn 2-29 - 2-31.

τ_{xr} Shear stress, eqn 2-32.

ω Vorticity.

SUBSCRIPTS:

aw Adiabatic wall.

e Evaluated at the edge of the boundary layer.

i,j Grid point indices.

i,j Indicial notation, chapter 2.

j Evaluated in the jet flow.

n Normal to the nozzle wall.

s Tangent to the nozzle wall.

t Turbulent flow.

tr Transition from regular shock reflection to Mach disc reflection.

w Evaluated in the wake.

o Stagnation value.

∞ Evaluated in the external freestream.

SUPERSCRIPTS:

n Evaluated at known time, $n\Delta t$.

$n+\frac{1}{2}$ Evaluated at intermediate predictor time level, $(n+\frac{1}{2})\Delta t$.

$n+1$ Evaluated at new corrector time level, $(n+1)\Delta t$.

o Evaluated at time level $t=0$.

OTHER NOTATION:

($\bar{\cdot}$) Denotes a two-dimensional matrix.

($\bar{\cdot}$) Denotes time averaged values, chapter 2.

(\cdot)' Denotes unsteady values due to turbulence, chapter 2.

ABSTRACT

The use of computational analysis in the design of propulsive nozzle installations has recently expanded as advanced digital computers have been developed which result in lowering computational costs versus actual wind tunnel test costs. Although a range of numerical techniques has been applied in this area, only those utilizing the full Navier-Stokes equations across the flow domain have successfully simulated the viscous phenomena associated with aft-end flowfields. Navier-Stokes methods are particularly useful for predicting off-design nozzle characteristics where the overexpanded or underexpanded flowfield is more complex and where viscous regions are more prevalent than at on-design conditions. One feature typical of these off-design conditions is the appearance of a strong normal shock wave referred to as a Mach disc. Viscous nozzle flowfields containing this phenomenon have not been adequately simulated in the past. This research details the development of a numerical Navier-Stokes method capable of accurately predicting supersonic coflowing nozzle flowfields which contain both highly viscous regions and complex shock structures typified by the Mach disc formation.

Numerical solutions to the Navier-Stokes equations are obtained for a domain containing an axisymmetric coflowing nozzle with a thick base annulus ($M_\infty = 1.94$, $M_{jet} = 3.0$, $Re_\infty = 2.2 \times 10^6$). Five nozzle pressure ratio conditions ranging from a highly overexpanded case ($P_j/P_\infty = 0.15$) which exhibits a Mach disc shock formation, to a slightly underexpanded case ($P_j/P_\infty = 1.59$) are examined and solved numerically. The weak con-

servative form of the two-dimensional (axisymmetric), time dependent Navier-Stokes equations is solved using MacCormack's explicit finite difference method. This algorithm is an efficient Lax-Wendroff type differencing scheme of second order accuracy which utilizes time-splitting and two-step predictor-corrector techniques. An adaptive grid scheme is utilized in the wake of the nozzle base annulus that allows the fine mesh region of the computational grid to remain in the mixing layer containing high flow gradients as each solution progresses towards convergence. Appropriate numerical boundary conditions are applied that allow the computational domain to be restricted to a compact region surrounding the nozzle. Locally dependent eddy viscosity modelling is applied in the form of a Cebeci-Smith two layer model in the boundary layer regions on the nozzle walls, and a form of the Prandtl mixing length model in the nozzle wake region.

The numerical solutions successfully reproduced all of the essential nozzle flow features including boundary layers, corner expansions, recompression shocks, the separated recirculation region along the nozzle base wall, and the evolution of the near wake to a far wake type of flow. Correct transition from regularly reflected shock waves at the line of symmetry in the jet core to the strong Mach disc shock reflection was numerically achieved, as was the simulation of the subsonic embedded region immediately behind the Mach disc shock structure. Numerically obtained nozzle base pressure coefficients were within seven percent of the experimentally determined values for all cases where the flow obeyed the assumption of remaining attached in the divergent portion of the convergent-divergent nozzle.

Present solution times for 2,500 point grids are on the order of

two to four hours when run on a Cyber 750 computer. A fully vectorized version of the present computer code can be expected to converge within five minutes on a CRAY-1 computer for similar grids, allowing the computation of more complex nozzle geometries and better resolution in the boundary layers through the use of a finer mesh in future efforts.

CHAPTER I

INTRODUCTION

1.1 BACKGROUND

The increased importance of the aft-end drag problem associated with nozzle installations in current and future high performance aircraft has led to extensive and very costly experimental nozzle test programs. Any technique which can reduce this requirement for wind tunnel testing in the design of nozzle installations will result in a significant savings to the technical community of both time and resources.

Computational aerodynamics shows great promise as a field which can have a favorable impact on this requirement for nozzle design information. Current Navier-Stokes techniques in this area utilize advanced digital computers to simulate the flowfield surrounding the nozzle at projected flight conditions. It has been shown that boundary layer and shear layer growth, areas of separated flow, shock wave formation and interactions, and jet plume blockage and entrainment characteristic of nozzle flows can be analyzed using computational techniques. Unlike experimental testing, computational analysis is not necessarily restricted by wind tunnel Reynolds number or nozzle exhaust temperature limitations. Flowfields analyzed computationally can also eliminate the undesirable effects of support stings and test section walls that occur during experimental testing. As more advanced computers are developed, the cost of numerical analysis decreases. Since the cost of wind tunnel testing is steadily increasing, computational analysis is being utilized more extensively.

Several of the first computational solutions to include viscous

effects inherent to aft end or nozzle flowfields consisted of patching techniques that divided the field into predominantly inviscid and viscous regions. Grossman and Melnik (1), and Cosner and Bower (2) obtained transonic boattail nozzle solutions using iterative techniques that divided the flowfield into an inviscid freestream, an inviscid jet, and a viscous boundary layer and mixing layer region. The free-stream solution procedure assumed irrotational potential flow that could be solved by a relaxation algorithm applied to the potential flow equations. The rotational inviscid supersonic jet was solved using a hyperbolic marching technique. Imbedded shocks in the jet were explicitly fitted to satisfy the Rankine-Hugoniot equations. The viscous mixing region was assumed to be isobaric and was solved using integral techniques. Each region was solved separately and patched together iteratively using pressure and flow direction conditions at the common boundaries. Separation regions could not be accounted for, so equivalent fitted body blending was used to obtain reasonable flow solutions.

Pergament, Dash, and Wilmoth (3) introduced a displacement thickness correction to the inviscid plume boundary to account for the effects of jet entrainment on the inviscid external flow calculation. Their analysis also included the effects of species mixing and pressure gradients in the mixing region, but still could only account for separation regions by body blending techniques. Yeager (4) attempted to include a fourth separation region involving recirculating flow that was defined by a dividing streamline which connected separation and reattachment points. The extent of this region was determined using local control volume analyses, and it was found that reasonable reattachment points could only be predicted through the application of empirical corrections during the

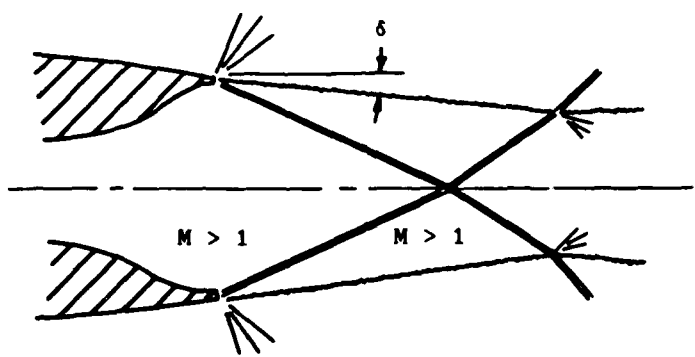
solution procedure. Although these iteratively patched solutions gave reasonable results for specific data sets, the required amount of empirical matching and explicit fitting limits the use of this type of computational method as a predictive technique.

A more adaptable method of simulating the viscous-inviscid interactions that occur in typical nozzle flowfields involves solving the time dependent, compressible Navier-Stokes equations uniformly over the entire nozzle flowfield. This approach has a direct advantage over the previously discussed iteratively patched methods where an accurate viscous-inviscid matching procedure is required in order to obtain reasonable results. In the direct approach, the predominantly inviscid and viscous flow regions are computed simultaneously with no matching required. Holst (5) used this approach to solve for supersonic flow over axisymmetric boattail nozzles with plume simulators. Although a plume simulator does not model the entrainment and blockage of a jet plume, its flowfield does contain phenomena characteristic to coflowing nozzles such as turbulent boundary layers, recompression shock waves, and separated recirculating regions of flow. Holst's solutions were obtained using MacCormack's explicit finite difference algorithm, a stretched mesh aligned with the solid body through an analytic transformation and a two layer eddy viscosity model to account for the Reynold's stresses that included a relaxation formula to model the separated flow region. Pressure distributions, skin friction coefficients and areas of separated flow were in good agreement with experimental data, particularly in the cases where a fine mesh was utilized. Mikhail (6) recently computed solutions for viscous

supersonic flow around an axisymmetric boattail nozzle with a jet exhaust flow. MacCormack's explicit method was again used as the numerical algorithm, together with a surface oriented mesh system obtained through a numerical mapping procedure. Reynold's stresses were also accounted for through the application of algebraic eddy viscosity models. Reasonable agreement with experimental surface pressure data on the boattail was obtained.

Navier-Stokes solutions are especially useful for predicting the off-design nozzle characteristics where the flowfield is in either a significantly overexpanded or underexpanded state. At these conditions the flow structure is usually more complex with viscous regions becoming more prevalent than at on-design conditions. One feature typical of these off-design conditions is the establishment of a triple-point in the jet flow, and the appearance of a strong normal shock wave referred to as a Mach disc in axisymmetric flow or a Riemann wave in two-dimensional flow (Figure 1). This strong shock formation occurs when the deflection angle of the jet flow is large enough so that the resulting shock wave is too strong for a regular reflection at the centerline to exist. Near the centerline the Mach disc must be normal, since this is the only way a shock can occur without any change in flow direction. As shown in Figure 2, both the Mach disc and the reflected shock are curved near the triple point (7). A slip line emanates from the triple point, and the flow downstream of the Mach disc and reflected shock is rotational in nature due to the curvature of the shocks. As discussed by Henderson and Lozzi (8), this region downstream of the shocks may be either totally subsonic or contain both supersonic and subsonic regions. If the incident Mach

REGULAR REFLECTION



MACH REFLECTION

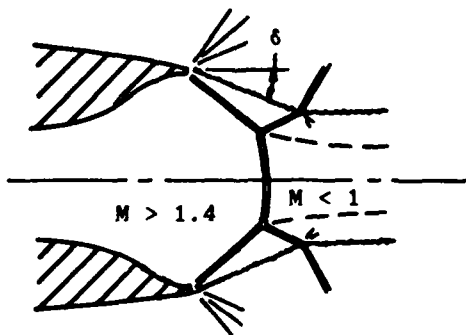


Figure 1. Shock Structure for a Typical Overexpanded Coflowing Axisymmetric Nozzle.

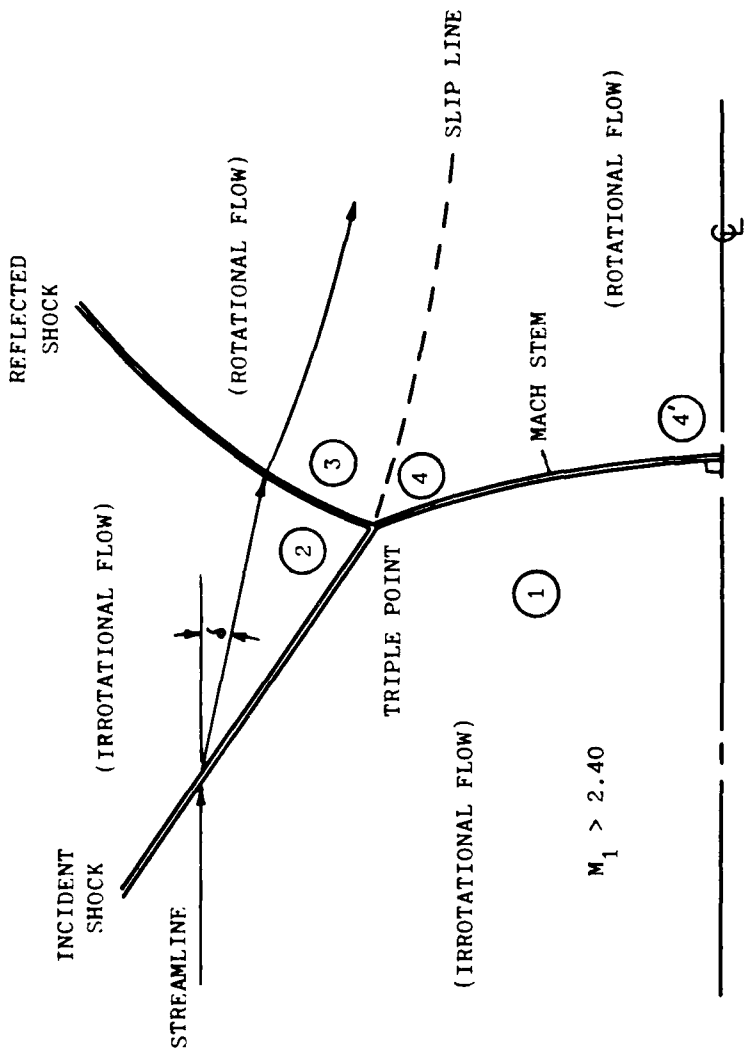


Figure 2. Schematic of a Typical Mach Reflection.

number M_1 is greater than 2.40, region 3 will be supersonic, while region 4 remains subsonic. Since the jet Mach numbers relevant to this investigation are greater than 2.40, the latter case in which a subsonic core only exists behind the Mach disc will be examined.

The transition from regular to Mach reflections can also be examined using a hodograph diagram shown in Figure 3. For deflection angles less than the transition angle (δ_{tr}), the flow can be brought to the required zero deflection at state 3 through a weak regular wave reflection. For deflection angles greater than the transition angle, the flow in region 3 cannot achieve a zero deflection state, and lies on the strong shock portion of the initial shock polar. The flow near the centerline passes through a strong normal shock to condition 4' with no deflection occurring. The flow state at the curved Mach disc then exists along the strong shock portion of the incident shock polar from a zero deflection state 4' near the centerline to a deflected state 4 near the triple point with a pressure and flow angle equal to that in region 3, but with different velocity and entropy values that generate the slip line.

The mixed supersonic-subsonic flow region surrounding the Mach disc greatly complicates the analysis of nozzle flowfields in which this shock structure is present. Flowfields containing this phenomena have not been adequately simulated in the past using viscous techniques. A variety of techniques for locating the triple point and the resulting normal shock have been presented that utilize an iterative combination of the method of characteristics and schemes involving approximate analyses such as pressure requirements downstream of the strong shock (9,10) or one-dimensional flow calculations downstream through a throat region in the flow (11,12). Although each of these methods give reason-

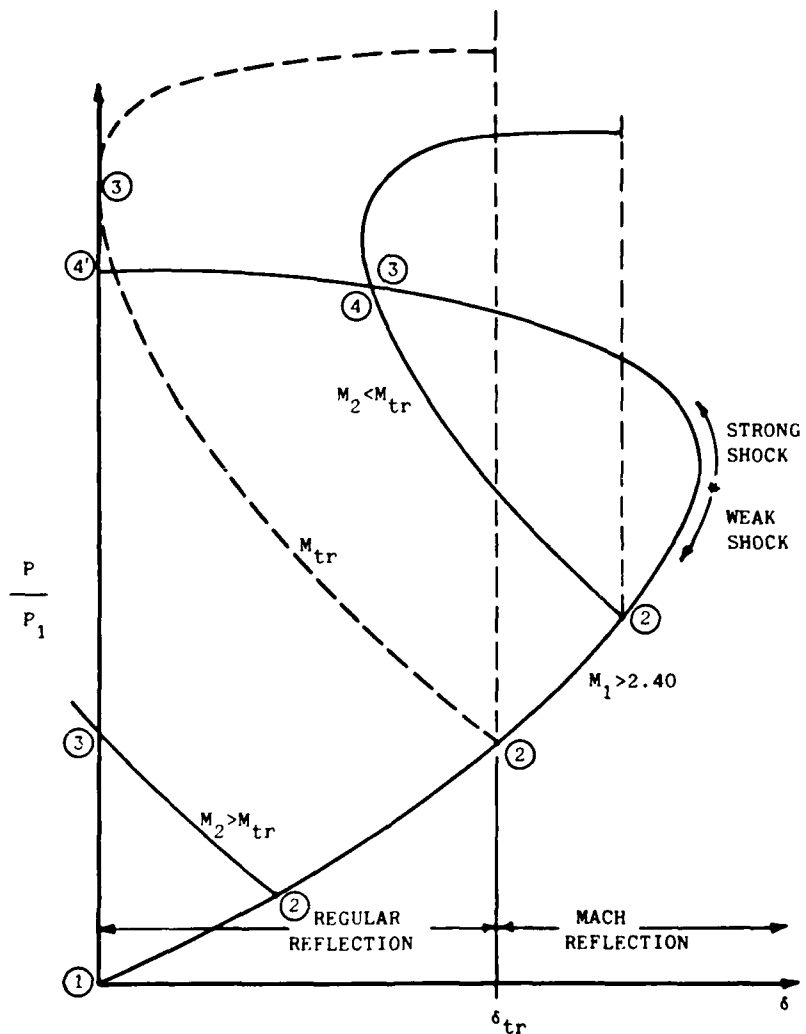


Figure 3. Hodograph Diagram Showing Shock Polar Intersections for Transition from Regular to Mach Reflection.

able results for determining the triple point location and size of the resulting Mach disc, each is only valid for a limited range of nozzle pressure ratios and jet Mach numbers. In addition, none of these techniques give a solution for the subsonic core region downstream of the normal shock. At least two time dependent inviscid techniques have been used to overcome the deficiencies of the semi-empirical methods previously mentioned. Jofre (13) performed a finite difference technique for an underexpanded jet with a Mach disc solution. A method of characteristics solution was used in the plume expansion region near the nozzle exit. This gave an upstream flow profile used in the time dependent solution further downstream. Sinha, Zakkay, and Erdos (14) analyzed a two-dimensional underexpanded jet containing a strong normal shock using a finite difference technique over the entire flowfield of interest. Both of these investigations used versions of Lax-Wendroff numerical algorithms and simple square grids. These solutions were much more adaptable than the previous semi-empirical techniques since the flow tends to adjust to its local environment so that the proper shock structure is automatically obtained as the solution develops. However, these solutions represent only a first approximation of the correct viscous solution (15), particularly in the region downstream of the normal shock as shown in Figure 4. Flow properties in this region were found to be heavily dependent on the level of damping used in the solution algorithm. For example, Jofre (13) found that an unrealistic region of reverse flow was generated immediately behind the normal shock unless heavy damping was applied in the solution procedure.

All of these inviscid solutions involved jets exhausting into a quiescent atmosphere. Solutions were not attempted for the more com-

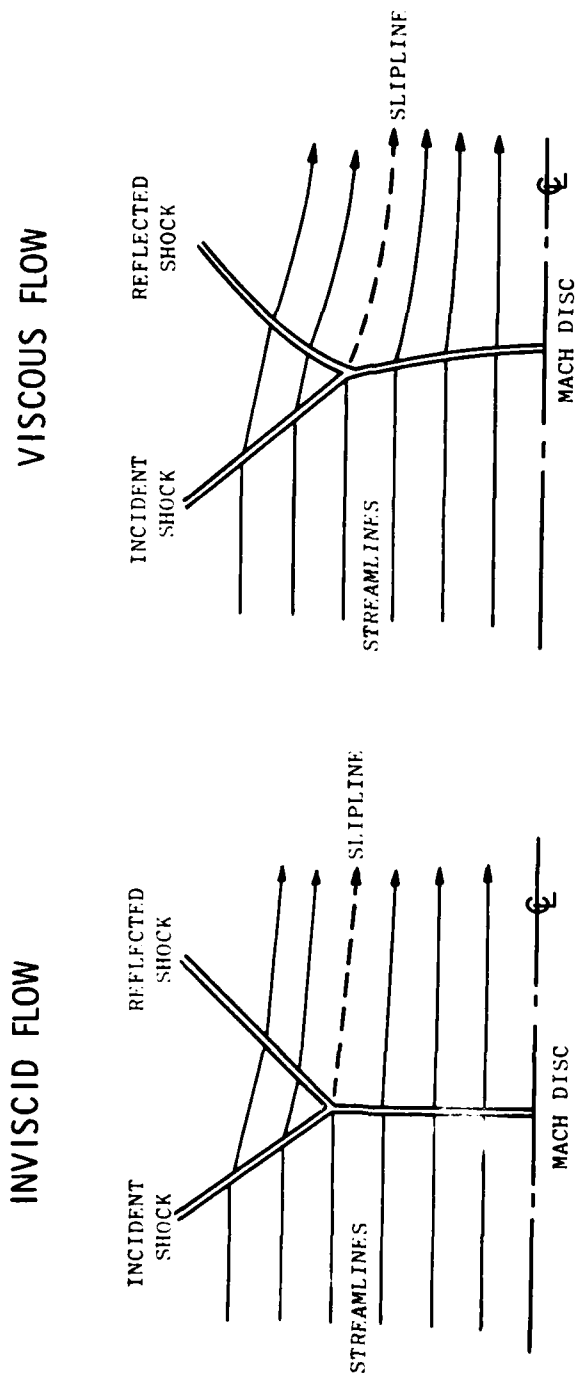


Figure 4. Viscous Effects on the Mach Disc Structure.

plex case of a coflowing nozzle where the external flow stream interacts with the jet. A full Navier-Stokes solution which accounts for the viscous effects present in the flow field at these off-design conditions is necessary in order to adequately simulate both the strong-shock structure with its resulting imbedded subsonic flow region as well as the interaction of the jet plume with the external flow field.

1.2 RESEARCH OBJECTIVES

The primary objective of this research is the development of a numerical Navier-Stokes method capable of accurately predicting supersonic coflowing nozzle flowfields which contain both highly viscous regions and complex shock structure typified by the Mach disc shock formation. Overexpanded axisymmetric nozzles will primarily be simulated, since they meet the previous criteria while possessing fairly compact flow domains which contain the flow phenomena of interest. The experimental data of Bromm and O'Donnell (16) has been chosen as a basis for comparison in this research effort. Data in this reference is given for an axisymmetric Mach three isentropic nozzle embedded in a turbulent Mach 1.94 external flowfield as shown in Figure 5. Nozzle pressure ratios ranging from a slightly underexpanded condition to a highly overexpanded condition which exhibits the Mach disc structure were obtained experimentally. This particular nozzle possesses a relatively thick base annulus which generates a strong viscous-inviscid interaction in the near wake region of the nozzle. These interactions affect the development of the primarily inviscid shock structure, and can only be analyzed properly using a full Navier-Stokes methodology.

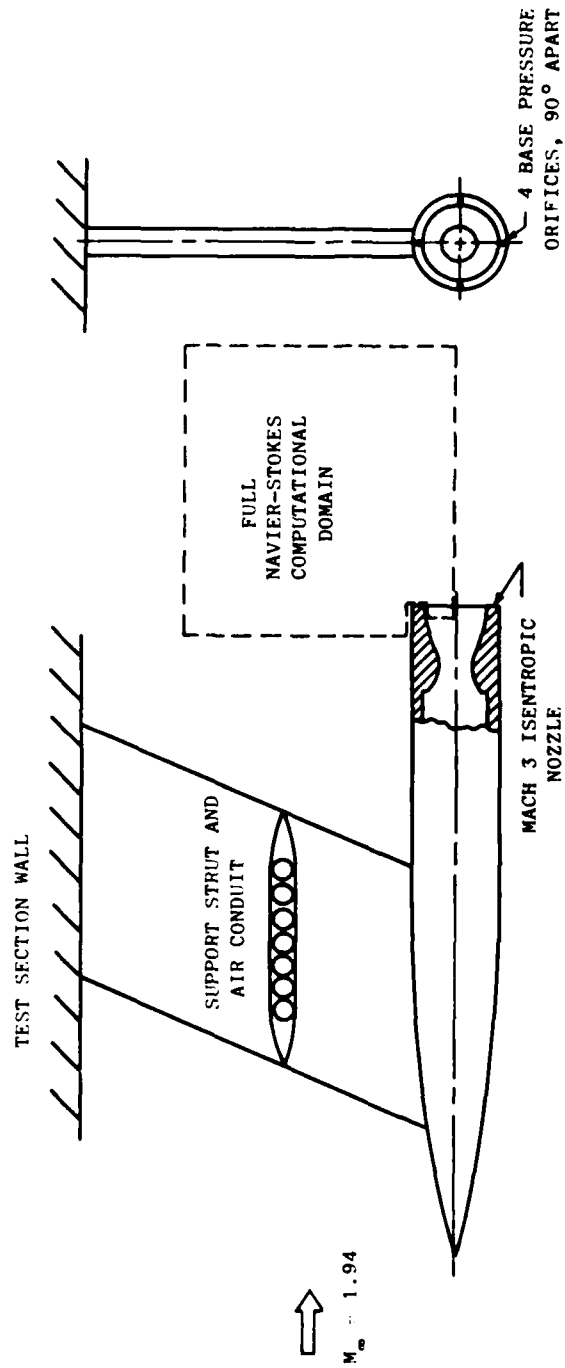


Figure 5. Schematic of the Axisymmetric Coflowing Jet Model used as a Basis for the Computational Solutions.

Although Mikhail achieved full Navier-Stokes solutions for an axisymmetric coflowing nozzle, he was not able to generate an accurate solution for the condition at which a Mach disc shock structure was shown to exist experimentally (6). Possible causes of this inability to generate the strong shock structure include boundary condition formulation, mesh spacing and turbulence modeling. These three areas will be concentrated on in the present investigation in order to achieve the desired goal of an accurate predictive technique for both on-design and off-design nozzle performance.

CHAPTER II

MATHEMATICAL DESCRIPTION OF THE FLOW STRUCTURE

2.1 GOVERNING EQUATIONS

The governing equations for flows containing the shock and viscous phenomena of interest are the conservation equations for mass, momentum, and energy known as the Navier-Stokes equations. The gases involved are assumed to be single component, have constant specific heats, and obey the perfect gas equation of state:

$$P = \rho RT \quad (2-1)$$

In computational fluid dynamics, the Eulerian method is usually applied to the problem of interest. This method involves a fixed control volume that is specified relative to a given coordinate system. Properties of the fluid are then specified as functions of both time and space. The conservation equations are approached using this methodology.

CONSERVATION OF MASS

For a given system in which matter is neither created or destroyed, the law of mass conservation can be written as

$$\iiint_V \left(\frac{\partial \rho}{\partial t} + \nabla \cdot (\rho \vec{u}) \right) dV = 0 \quad (2-2)$$

where V is an arbitrary volume fixed in space.

CONSERVATION OF MOMENTUM

For a given system, the law of momentum conservation states that the rate of change of momentum is equal to the sum of the external forces

acting on the control volume. If body forces are neglected, this law can be written as:

$$\iiint_V \left[\frac{\partial(\rho\vec{u})}{\partial t} + \nabla \cdot (\rho\vec{u}) \vec{u} \right] dV = \iiint_V (\nabla \cdot \bar{\mathbf{S}}) dV \quad (2-3)$$

The variable $\bar{\mathbf{S}}$ denotes a stress tensor involving pressure and viscous forces which acts on the fluid.

CONSERVATION OF ENERGY

The law of conservation of energy states that for a given system which does not contain any internal heat sources, the rate of change of the total energy of the system is equal to the heat added into the system plus the work done on the system by viscous and pressure forces.

This can be stated as

$$\iiint_V \left[\frac{\partial(\rho e)}{\partial t} + \nabla \cdot (\rho e) \vec{u} \right] dV = \iiint_V (\nabla \cdot \vec{u} \cdot \bar{\mathbf{S}} - \nabla \cdot \vec{q}) dV \quad (2-4)$$

Since these conservation equations are valid for any arbitrary volume V; when the integrands are continuous, these equations imply that:

$$\frac{\partial \rho}{\partial t} + \nabla \cdot \rho \vec{u} = 0 \quad (2-5)$$

$$\frac{\partial(\rho \vec{u})}{\partial t} + \nabla \cdot (\rho \vec{u}) \vec{u} - \nabla \cdot \bar{\mathbf{S}} = 0 \quad (2-6)$$

$$\frac{\partial(\rho e)}{\partial t} + \nabla \cdot (\rho e) \vec{u} + (\nabla \cdot \vec{q} - \nabla \cdot \vec{u} \cdot \bar{\mathbf{S}}) = 0 \quad (2-7)$$

It should be noted that these equations are written in conservative form where, for the two-dimensional and axisymmetric flows of interest, the applicable dependent variables are ρ , ρu , ρv , and ρe . As shown by Roache (17), this conservative form allows the finite difference equations to preserve the Gauss divergence property of the continuum equations. This form allows a balance between the flux quantities and

accumulation rates for a small control volume. Roache also states that the Rankine-Hugoniot shock relations were derived using the conservative form. Thus, shock jump conditions are automatically satisfied since the conservative variables are continuous across the shock and need no special treatment because of discontinuities. This approach is known as shock capturing or shock smearing. The conservation form of the equations then allows the finite difference formulation to satisfy the physical laws on a macroscopic scale, not merely in some academic limit as Δx , Δy , and Δt approach zero.

Since the flowfields of interest are turbulent, the solution of the conservation equations must take into account the effects of the random fluctuations of the dependent variables inherent to turbulent flows. In accounting for these effects, cartesian tensor notation will be applied. The usual conventions of a repeated subscript indicating summation over the entire range of indices and a comma representing partial differentiation will be used to make the equations compact. Cartesian tensors are used to allow working directly with the physical components, while still being applicable to the 2-D and axisymmetric systems of interest. The conservation equations (2-5) through (2-7) can then be written as:

$$\rho,_{t} + (\rho u_j),_j = 0 \quad (2-8)$$

$$(\rho u_i),_t + (\rho u_i u_j + \delta_{ij} P - \tau_{ij}),_j = 0 \quad (2-9)$$

$$(\rho e),_t + (\rho eu_j + \dot{q}_j - u_i \tau_{ij}),_j = 0 \quad (2-10)$$

where the stress tensor S_{ij} has been expanded in the form:

$$S_{ij} = -P\delta_{ij} + \tau_{ij} \quad (2-11)$$

The dependent variables in the conservation equations can be expanded into the following form:

$$u = \bar{u} + u' \quad (2-12a)$$

$$v = \bar{v} + v' \quad (2-12b)$$

$$P = \bar{P} + P' \quad (2-12c)$$

$$\rho = \bar{\rho} + \rho' \quad (2-12d)$$

$$e = \bar{e} + e' \quad (2-12e)$$

In these expansions the barred variables represent time averaging over a time interval that is long compared to turbulent eddy fluctuations, yet small compared to macroscopic flow changes. The primed variables then represent fluctuations due to the turbulent nature of the flow. As discussed by Chapman (18), this time averaging approach is valid since the frequencies of most unsteady flows of interest are a factor of 10 to 100 below the mean frequency of turbulent eddies.

If the dependent variables u , v , and e are mass averaged as described in reference (19), and ρ and P are mean (time averaged) state variables, then the conservation equations can be written in the form of mean flow equations as:

$$\bar{u}_t + (\bar{\rho}\bar{u}_j)_j = 0 \quad (2-13)$$

$$(\bar{\rho}\bar{u}_i)_t + [(\bar{\rho}\bar{u}_i\bar{u}_j) + \bar{P}_{ij} - (\bar{\tau}_{ij} - \bar{\rho}u'_i u'_j)]_j = 0 \quad (2-14)$$

$$(\bar{e})_t + [\bar{\rho}\bar{u}_j + \bar{q}_j + \bar{\rho}u'_j e' - \bar{u}_i (\bar{\tau}_{ij} - \bar{\rho}u'_i u'_j)]_j = 0 \quad (2-15)$$

where a higher order mean energy dissipation term in u'_i has been neglected in the energy equation (2-15).

The term $[-\bar{\rho}u'_i u'_j]$ is known as the Reynolds stress. It represents a momentum transfer caused by turbulent fluctuations present in the flow-field. This Reynolds stress term can be written as an apparent stress caused by the turbulent nature of the flow:

$$\tau_{ij}|_{turb} = - \overline{\rho u'_i u'_j} \quad (2-16)$$

Since air is essentially an isotropic fluid, the mean stress term can be expanded into its normal and shear stress components as:

$$\bar{\tau}_{ij} = \lambda \bar{u}_{k,k} \delta_{ij} + \mu (\bar{u}_{i,j} + \bar{u}_{j,i}) \quad (2-17)$$

The turbulent stress term can then be written in analogous form as:

$$\bar{\tau}_{ij}|_{turb} = \lambda_t \bar{u}_{k,k} \delta_{ij} + \epsilon (\bar{u}_{i,j} + \bar{u}_{j,i}) \quad (2-18)$$

where λ_t and ϵ are the turbulent viscosity coefficients of the flow.

The coefficient ϵ is known as the eddy viscosity, and is analogous to the molecular viscosity coefficient μ . However, ϵ is more a property of the dynamics of the flow, whereas μ is only a property of the fluid. Combining the mean and turbulent stress terms, an overall stress term can be written as:

$$\bar{\tau}_{ij}|_{total} = (\lambda + \lambda_t) \bar{u}_{k,k} \delta_{ij} + (\mu + \epsilon) (\bar{u}_{i,j} + \bar{u}_{j,i}) \quad (2-19)$$

In the energy equation an additional unsteady term appears. This term is by nature an apparent heat flux caused by the fluctuations inherent to turbulent flow and can be written as:

$$\dot{\bar{q}}_j|_{turb} = \overline{\rho u'_j e'} \quad (2-20)$$

If the heat flux term $\dot{\bar{q}}_j$ is defined by the Fourier heat equation as:

$$\dot{\bar{q}}_j = -k \bar{T}_{,j} = - (C_p \mu / Pr) \bar{T}_{,j} \quad (2-21)$$

then by the former analogy $\dot{\bar{q}}_j|_{turb}$ can be written as:

$$\dot{\bar{q}}_j|_{turb} = - (C_p \epsilon / Pr_t) \bar{T}_{,j} \quad (2-22)$$

where again ϵ is the eddy viscosity coefficient, and Pr_t is the turbulent Prandtl number of the flow. Combining these two heat fluxes, a total

heat flux can be written as:

$$\bar{q}_j \text{ total} = -C_p (\nu/\Pr + \epsilon/\Pr_t) \bar{T}_j \quad (2-23)$$

The mean conservation equations can then be written in the following form, where the overbars on the terms are dropped for convenience, and where the values of the shear stresses and heat fluxes are the total values:

$$\rho_t + (\rho u_j)_j = 0 \quad (2-24)$$

$$(\rho u_i)_t + [(\rho u_i)u_j + P\delta_{ij} - \tau_{ij}]_j = 0 \quad (2-25)$$

$$(\rho e)_t + [(\rho e) u_j + \dot{q}_j - u_i \tau_{ij}]_j = 0 \quad (2-26)$$

Since the flowfields of interest are either two-dimensional or axisymmetric in nature, the mean conservation equations can be written in the following compact vector form:

$$\frac{\partial U}{\partial t} + \frac{\partial F}{\partial X} + \frac{1}{r^{j_0}} \frac{\partial (r^{j_0} G)}{\partial r} = j_0 \cdot \frac{H}{r^{j_0}} \quad (2-27)$$

where $j_0 = 0$ or 1 for either the two dimensional or axisymmetric cases, respectively, and

$$U = \begin{pmatrix} \rho \\ \rho u \\ \rho v \\ \rho e \end{pmatrix}; \quad F = \begin{pmatrix} \rho u_2 \\ \rho u^2 - \sigma_{xx} \\ \rho uv - \tau_{xr} \\ \rho ue + q_x - u \sigma_{xx} - v \tau_{xr} \end{pmatrix} \quad (2-28)$$

$$G = \begin{pmatrix} \rho v \\ \rho uv - \tau_{xr} \\ \rho v^2 - \sigma_{rr} \\ \rho ve + q_r - u \tau_{xr} - v \sigma_{rr} \end{pmatrix}; \quad H = \begin{pmatrix} 0 \\ 0 \\ -\sigma_H \end{pmatrix}$$

where

$$\sigma_{xx} = -P + (\nu + \epsilon_t) \operatorname{div} \vec{V} + 2(\nu + \epsilon) \frac{\partial u}{\partial x} \quad (2-29)$$

$$\sigma_{rr} = -P + (\nu + \epsilon_t) \operatorname{div} \vec{V} + 2(\nu + \epsilon) \frac{\partial v}{\partial r} \quad (2-30)$$

$$\dot{\omega}_H = -P + (\lambda + \frac{1}{t}) \operatorname{div} \vec{V} + 2(u + \epsilon) \frac{v}{r} \quad (2-31)$$

$$\dot{\zeta}_{xr} = (u + \epsilon) \left(\frac{\partial u}{\partial r} + \frac{\partial v}{\partial x} \right) \quad (2-32)$$

$$q_x = -C_p \left(\frac{u}{Pr} + \frac{\epsilon}{Pr_t} \right) \frac{\partial T}{\partial x} \quad (2-33)$$

$$q_r = -C_p \left(\frac{v}{Pr} + \frac{\epsilon}{Pr_t} \right) \frac{\partial T}{\partial r} \quad (2-34)$$

and

$$\operatorname{div} \vec{V} = \frac{\partial u}{\partial x} + \frac{\partial v}{\partial r} + j_o \frac{v}{r} \quad (2-35)$$

The coefficient of viscosity μ for air can be assumed to vary according to Sutherland's law (19):

$$\mu = (2.27 \cdot 10^{-8}) T^{1.5} / (T + 198.6) \text{ (lbf - sec/ft}^4) \quad (2-36)$$

The second coefficient of viscosity is assumed as the following by applying Stokes Hypothesis:

$$(\lambda + \frac{1}{t}) = -2/3 (\mu + \epsilon) \quad (2-37)$$

The governing equations for the problem of interest now consist of the four conservation equations in matrix form (eq. 2-27) with four unknown dependent variables ρ , ρu , ρv and ρe . The perfect gas law is used to define the pressure in terms of these conservative variables, and a model of the dependence of the eddy viscosity on the mean flow must be introduced to overcome the "turbulent closure" problem inherent in the turbulent mean conservation equations.

For numerical computation in a transformed (ξ, η) cartesian plane, the matrix form of the conservation equations (2-27) can be written as:

$$\begin{aligned} \frac{\partial F}{\partial t} + [\zeta_x \frac{\partial F}{\partial \xi} + \frac{1}{r^{j_o}} \zeta_r \frac{\partial (r^{j_o} G)}{\partial \xi}] \\ + [\eta_x \frac{\partial F}{\partial \eta} + \frac{1}{r^{j_o}} \eta_r \frac{\partial (r^{j_o} G)}{\partial \eta}] = j_o - \frac{H}{r^{j_o}} \end{aligned} \quad (2-38)$$

where ξ and η are now the independent variables, and the transformation

derivatives ξ_x , ξ_r , η_x , and η_r are obtained numerically from a mapping procedure. Equation (2-38) is actually in weak conservation form due to the varying coefficients in front of the derivatives, and also due to the source term in the axisymmetric case.

2.2 BOUNDARY AND INITIAL CONDITIONS

Boundary and initial conditions must be given in order to solve the conservation equations which govern the flowfield. These conditions must be carefully specified, since many flow features such as shock waves, boundary layers, and recirculation areas arise from boundary conditions. For the solution of a symmetric two-dimensional or axisymmetric supersonic jet embedded in a supersonic external flowfield, the domain of interest can be defined as shown in Figure 6. Only one-half of the total nozzle flowfield needs to be considered due to the axis of symmetry on the jet centerline. The remainder of this chapter will detail the specific boundary conditions that are pertinent to this problem.

THE UPSTREAM BOUNDARY

Inflow conditions on the upstream jet boundary (AB) and the upstream external boundary in the freestream (CD) are completely specified. Velocity, pressure, and temperature profiles determined from auxiliary computations or known experimentally on this boundary fix ρ , ρu , ρv , and ρe for the duration of the problem solution at the boundary.

THE UPPER BOUNDARY

The upper boundary (DE) must accurately represent a free flight condition where mass flow is allowed across this boundary embedded in the supersonic external flowfield. Weak shock waves and Prandtl-Meyer

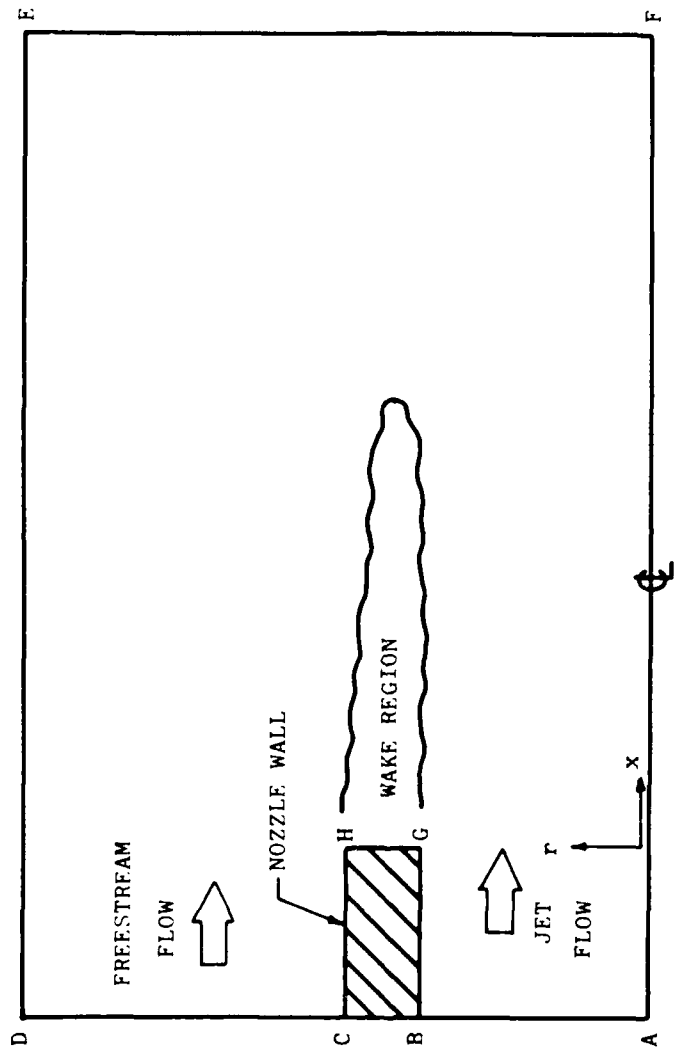


Figure 6. Physical Domain for the Computational Solutions.

expansion waves must also exit this boundary without being reflected artificially back into the domain of interest. One condition that allows this is the assumption of a simple wave solution:

$$\left. \frac{\partial U}{\partial \lambda} \right|_{DE} = 0 \quad (2-39)$$

where λ_I is the straight left running characteristic line passing through each point on the upper boundary. This characteristic line is determined only by the value of the Mach number and flow angle of the supersonic flow present near the upper boundary. This condition assumes that the flow along this boundary is inviscid and homentropic.

THE DOWNSTREAM BOUNDARY

The downstream boundary (EF) is unique in that no rigorous assumptions can be made about either the variables or their gradients unless the boundary is placed a great distance downstream. In this case a no change condition

$$\left. \frac{\partial f}{\partial x} \right|_{EF} = 0 \quad (2-40)$$

could be assumed, where f denotes the primitive variables ρ , u , v , and T . For the case where the downstream boundary is placed where gradients do exist, an extrapolation method based on this fact can be reasonably applied. One such method is to assume that a flow gradient accurate to second order can exist. This can be implemented as:

$$\left(\lambda \frac{\partial}{\partial x} \frac{\partial f}{\partial x} \right) \Big|_{EF} \approx 0 \quad (2-41)$$

In other words, gradients can occur which are parabolic with respect to x . This condition is reasonable if the gradients at this boundary are not severe as in the case where a strong shock wave exits the boundary.

THE CENTERLINE

The centerline boundary (AF) is a line of symmetry with no mass or energy flux across it. Therefore, the following boundary conditions can be applied

$$v|_{AF} = 0 \quad (2-42)$$

$$\frac{\partial}{\partial r}|_{AF} = 0 \quad (2-43)$$

$$\frac{\partial u}{\partial r}|_{AF} = 0 \quad (2-44)$$

Since the v component of velocity is zero on the centerline, this boundary is also a streamline in the jet flow. For steady, adiabatic flow with negligible volume forces, the total enthalpy along any streamline is a constant. Therefore, along the centerline,

$$H_0|_{AF} = (C_p T + \frac{u^2}{2})|_{AF} = \text{constant} \quad (2-45)$$

Since the condition at the jet exit is specified, the centerline boundary can be properly posed using this approach.

NOZZLE WALLS

The nozzle walls (BG, GH, and CH) are considered to be no-slip, impermeable boundaries. This assumption gives the conditions that:

$$u|_{\text{wall}} = 0 \quad (2-46a)$$

and

$$v|_{\text{wall}} = 0 \quad (2-46b)$$

Since the stainless steel nozzle consists of thin-walled material with a thermal conductivity much greater than that of the surrounding fluid, the nozzle walls are assumed to be at a constant temperature:

$$T|_{\text{wall}} = \text{constant} \quad (2-47)$$

This wall temperature is determined by applying a heat flux balance across the jet and freestream boundary layers as outlined in Appendix A.

The pressure on each nozzle wall is unknown, but can be approximated by applying the degenerate form of the appropriate normal momentum equation at each nozzle surface to obtain the following:

$$\frac{\partial P}{\partial n}|_{\text{wall}} = \frac{\partial t}{\partial s}|_{\text{wall}} \approx 0 \quad (2-48)$$

In this expression n is the direction normal to the wall surface, and s is the direction parallel to the surface.

INITIAL CONDITIONS

Since the governing equations contain time dependent terms, initial conditions must be specified before the solution process can begin. The specification of these initial conditions is somewhat arbitrary in nature, although steep gradients must be avoided to prevent numerical divergence during the solution process. Since the flow is predominantly supersonic in nature, the incoming flow profiles will have a dominant effect on the solution in the whole computational domain. The incoming flow conditions are imposed on the complete domain as discussed in the section on initial condition implementation of chapter 5.

CHAPTER III

NUMERICAL PROCEDURE

The numerical procedure consists of solving the governing equations with applicable boundary and initial conditions through the use of appropriate finite difference techniques on a high-speed computer. This procedure can be broken down into several elements which include the finite difference coordinate system, the solution algorithm, and the convergence criteria used in the computational solution. Each of these areas will be discussed in this chapter.

3.1 COORDINATE SYSTEM

Domain of Computation

The physical domain of computation consists of a rectangular area defined by orthogonal coordinates (x, r) as shown in Figure 7. The mesh consists of IL points on the x axis and JL points on the r axis, where IL and JL are dependent on the extent of the physical domain required for the particular jet plume case of interest.

Mesh Stretching

In order to obtain an accurate numerical solution of a viscous flow-field, the mesh spacing must be much finer in areas containing relatively high gradients of the variable properties such as velocity, density, and temperature. In the coflowing nozzle these high gradient areas include the boundary layers on the nozzle walls and the shear layer in the wake of the nozzle annulus. This stretching is accomplished through the use of a patched exponential stretching scheme of the following form:

$$r(j) = L_m \frac{c_n(j)}{(e^C - 1)} \text{ for } j = 1, N \quad (3-1)$$

where L_m and r are defined as shown in Figure 8. The constant C is determined by the minimum spacing Δr_{\min} desired for the mesh next to the wall boundary. Applying the desired Δr_{\min} to equation (3-1) gives

$$C = \frac{1}{\Delta r_{\min}} \log_e \left(1 + \frac{\Delta r_{\min}}{L_m} (e^C - 1) \right) \quad (3-2)$$

The value of C is then obtained through the use of an iterative Aitken extrapolation technique.

This mesh stretching procedure is applied in the radial direction on both sides of the nozzle wall where boundary layers are present. It is also applied in the axial direction at the end of the nozzle where the jet flow begins to expand or contract and where the near wake due to the nozzle annulus begins to form.

Adaptive Mesh

It is desireable that the fine mesh remain in the areas of relatively high velocity and temperature gradients as the solution progresses towards convergence. This is not a problem in the case of boundary layers that are adjacent to a fixed wall, but is a concern in the free shear layer area generated by the nozzle wake and the interaction between the jet and freestream flows. This shear region on the jet plume boundary will deflect to a degree that is primarily dependent on the nozzle pressure ratio. The fine mesh region should therefore also be adapted to conform to the general position of the shear region.

Hirt (21) has used a technique in the solution of free surface flows that allows the grid to adapt as the solution progresses. The following kinematic equation is applied in the region where the shear layer is present.

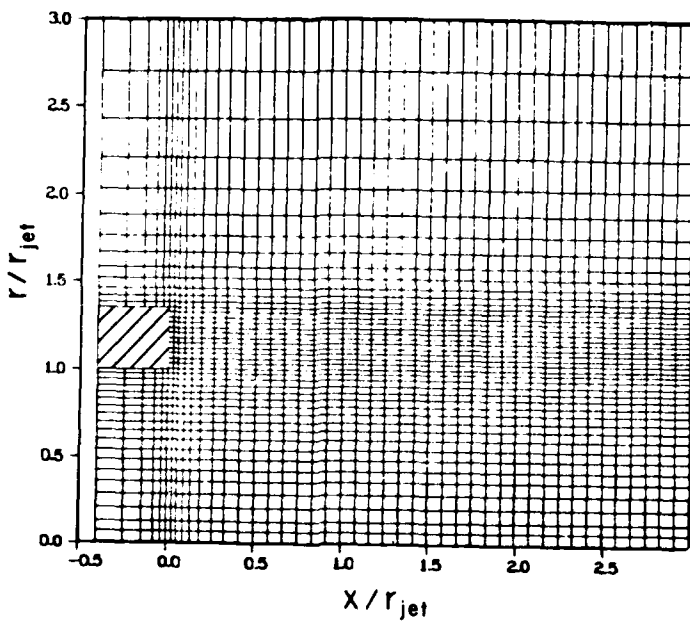


Figure 7. Finite Difference Mesh in Physical Space.

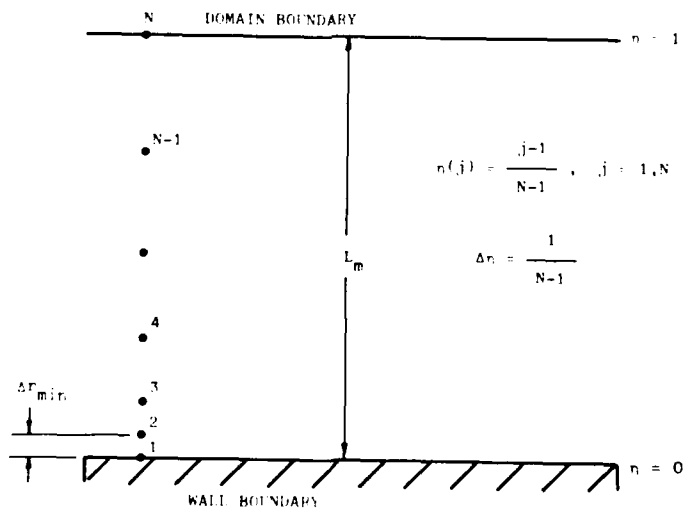


Figure 8. Exponentially Stretched Mesh Schematic.

$$\frac{\partial r}{\partial t} = C_A (v - u \frac{\partial r}{\partial x}) \quad (3-3)$$

This equation insures the condition that as the solution converges, the physical slope of the constant n finite difference cell boundaries is the same as that of the velocity vectors near each cell. When applied in a finite difference format, the grid can then adapt to the placement of the shear layer as shown in Figure 9. Details of this process are explained in Appendix B.

Coordinate Transformation

The physical domain as typically shown in Figure 9 is mapped to a unit square in the computational plane shown in Figure 10. The constant n lines are aligned parallel to the centerline and the constant ξ lines are in the direction normal to the centerline. The numerical algorithm operates on this coordinate system using the transformed conservation equations (2-32). Care must be taken in generating the physical mesh so that smoothness of the transformation coefficients (ξ_x , ξ_r , n_x , and n_r) is retained in order to reduce numerical errors caused by the mesh configuration.

3.2 SOLUTION ALGORITHM

MacCormack's Method

The weak conservative form of the two-dimensional, time-dependent Navier-Stokes Equations (eqn. 2-38) is solved using MacCormack's explicit finite difference method (22). This algorithm is an efficient Lax-Wendroff type differencing scheme of second order accuracy which utilizes time-splitting and two step predictor-corrector techniques.

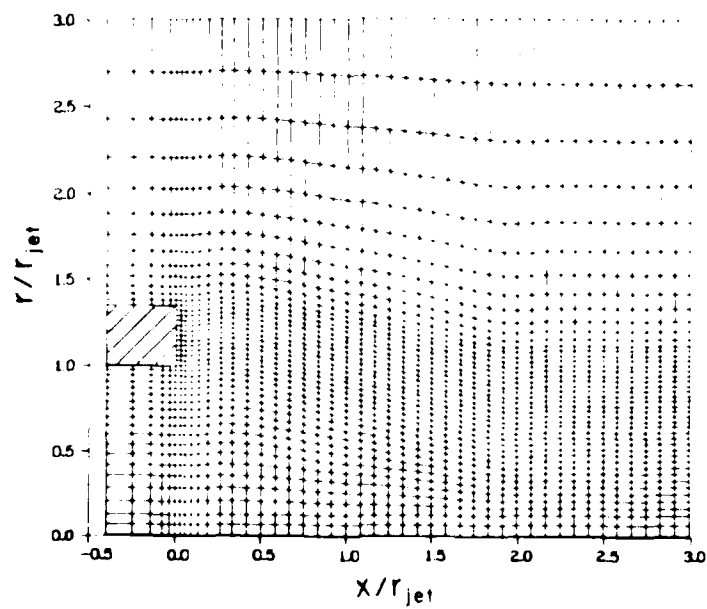


Figure 9. Adaptive Finite Difference Mesh, $P_j / P_\infty = 0.150$.

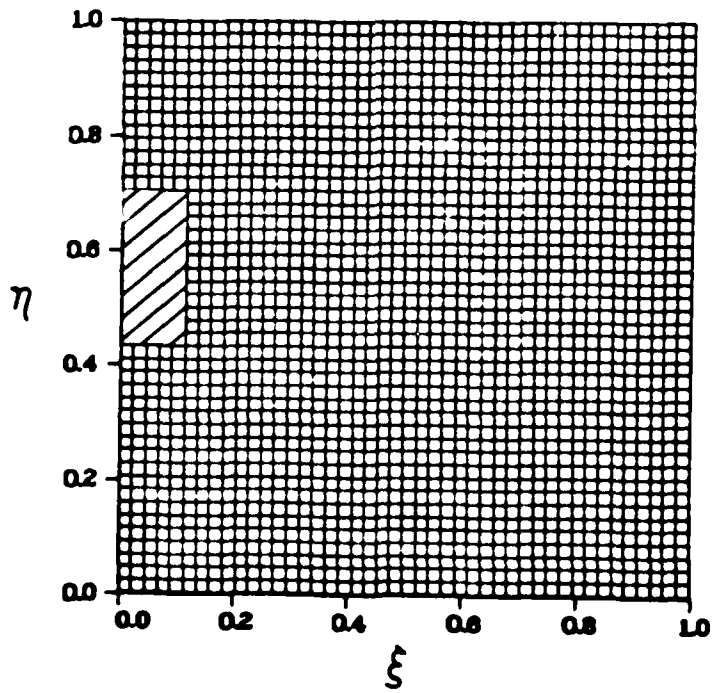


Figure 10. Computational Mesh in the Transformed Plane.

MacCormack's algorithm was chosen for application to the nozzle problem because of its previous success in computing inviscid-viscous interacting flows, its stability in supersonic flow, and its computational efficiency achieved by time-splitting the finite difference operators.

The computational solution is advanced in time by applying the numerical operator to the solution of the flowfield at time t . This can be written as:

$$U(\xi, n, t + \Delta t) = L(\Delta t) \cdot U(\xi, n, t) \quad (3-4)$$

where $L(\Delta t)$ is the two-dimensional numerical operator representing MacCormack's algorithm acting on the transformed conservation equations. Through the use of a time-splitting technique, this two-dimensional operator $L(\Delta t)$ is separated into two one-dimensional sweep operators in the ξ and n directions. The operator $L_\xi(\Delta t)$ denotes the solution of the equation:

$$\frac{\partial}{\partial t} + c_x \frac{\partial F}{\partial \xi} + \frac{1}{r^{j_o}} \xi_r \frac{\partial (r^{j_o} G)}{\partial \xi} = 0 \quad (3-5)$$

in the ξ direction by time increment Δt seconds. Similarly, the operator $L_n(\Delta t)$ represents the solution of

$$\frac{\partial}{\partial t} + c_x \frac{\partial F}{\partial n} + \frac{1}{r^{j_o}} \eta_r \frac{\partial (r^{j_o} G)}{\partial n} = j_o \frac{\partial H}{\partial r} \quad (3-6)$$

in the n direction by a time increment Δt seconds. The dependent variable vector $U(\xi, n, t)$ can then be advanced in time as

$$U(\xi, n, t + \Delta t) = [L_\xi^{M/2}(\Delta t/M) \cdot L_n^{M/2}(\Delta t/M)] \cdot U(\xi, n, t) \quad (3-7)$$

with

$$\Delta t = \Delta t_\xi \text{ if } \Delta t_\xi < \Delta t_n$$

or as

$$U(\xi, n, t + \Delta t) = [L_n^{N/2}(\Delta t/N) \cdot L_\xi(\Delta t) \cdot L_n^{N/2}(\Delta t/N)] \cdot U(\xi, n, t) \quad (3-8)$$

with

$$\Delta t = \Delta t_n \text{ if } \Delta t_n < \Delta t_\xi$$

In these equations M and N are the smallest even integers of the quotients $(\Delta t_n / \Delta t_\xi)$ and $(\Delta t_\xi / \Delta t_n)$, respectively, and Δt_ξ and Δt_n are the maximum allowable time steps in the ξ and n directions as determined by the Courant-Friedrichs-Lowy (CFL) limit discussed in the next section on stability. The values of M and N are usually equal to two for the grid distribution used in the solution of the nozzle problem. This sets up a truly alternating direction procedure that is desirable when gradients exist in more than one direction.

The finite difference forms of the sweep operators consist of a predictor-corrector procedure which increases the accuracy of the time-dependent term evaluations. This method utilizes one-sided differencing in the direction of sweep, but central differencing in the direction perpendicular to the sweeping coordinate. At the completion of the predictor-corrector process, this method is equivalent to a second order central differencing scheme in two dimensions.

The $L_\xi(\Delta t)$ sweep operator represents the following numerical procedure. A predicted intermediate value is computed by the expression:

$$\begin{aligned} U_{i,j}^{n+1} &= U_{i,j}^n - \frac{\Delta t}{\Delta \xi} [(\xi_x)_{i,j} (F_{i,j}^n - F_{i-1,j}^n) \\ &\quad + \frac{1}{r_{i,j}^{j_0}} (\xi_r)_{i,j} (r_{i,j}^{j_0} G_{i,j}^n - r_{i-1,j}^{j_0} G_{i-1,j}^n)] \end{aligned} \quad (3-9)$$

where $U_{i,j}^n$ is the known value at time t , and $U_{i,j}^{n+1}$ is the intermediate predictor value. The actual computed value at time $(t+\Delta t)$ is then calculated by applying the following corrector algorithm:

$$U_{i,j}^{n+1} = 1/2 \{ U_{i,j}^n + U_{i,j}^{n+1} - (\frac{\Delta t}{\Delta \xi}) [(\xi_x)_{i,j} (F_{i+1,j}^{n+1} - F_{i,j}^{n+1}) \\ + \frac{1}{r_{i,j}^{j_0}} (\eta_r)_{i,j} (r_{i+1,j}^{j_0} G_{i+1,j}^{n+1} - r_{i,j}^{j_0} G_{i,j}^{n+1})] \} \quad (3-10)$$

In this ξ sweep predictor-corrector algorithm, the matrices F and G are functions of the following difference quotients:

$$F_{i,j}^m, G_{i,j}^m = f(U_{i,j}^m, \frac{U_{i+1,j}^m - U_{i,j}^m}{\Delta \xi}, \frac{U_{i,j+1}^m - U_{i,j-1}^m}{2\Delta \eta}) \quad (3-11)$$

This scheme can be depicted graphically as shown in Fig. 11.

The $L_{\eta}(\Delta t)$ numerical sweep operator is formulated in a similar manner. The intermediate predictor value is given by the expression:

$$U_{i,j}^{n+1} = U_{i,j}^n - (\frac{\Delta t}{\Delta \eta}) [(\eta_x)_{i,j} (F_{i,j}^n - F_{i,j-1}^n) \\ + \frac{1}{r_{i,j}^{j_0}} (\eta_r)_{i,j} (r_{i,j}^{j_0} G_{i,j}^n - r_{i,j-1}^{j_0} G_{i,j-1}^n)] + \frac{j_0 \Delta t H_{i,j}^n}{r_{i,j}^{j_0}} \quad (3-12)$$

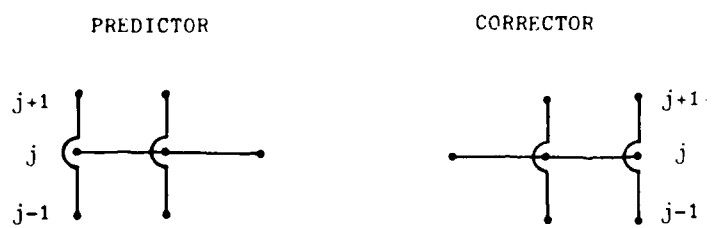
The corrector value at time $(t+\Delta t)$ is then given by:

$$U_{i,j}^{n+1} = 1/2 \{ U_{i,j}^n + U_{i,j}^{n+1} - (\frac{\Delta t}{\Delta \eta}) [(\eta_x)_{i,j} (F_{i,j+1}^{n+1} - F_{i,j}^{n+1}) \\ + \frac{1}{r_{i,j}^{j_0}} (\eta_r)_{i,j} (r_{i,j+1}^{j_0} G_{i,j+1}^{n+1} - r_{i,j}^{j_0} G_{i,j}^{n+1})] + \frac{j_0 \Delta t H_{i,j}^{n+1}}{r_{i,j}^{j_0}} \} \quad (3-13)$$

The matrices F and G are now functions of the following difference quotients:

$$F_{i,j}^m, G_{i,j}^m = f(U_{i,j}^m, \frac{U_{i+1,j}^m - U_{i-1,j}^m}{2\Delta \xi}, \frac{U_{i,j+1}^m - U_{i,j-1}^m}{2\Delta \eta}) \quad (3-14)$$

ξ SWEEP



η SWEEP

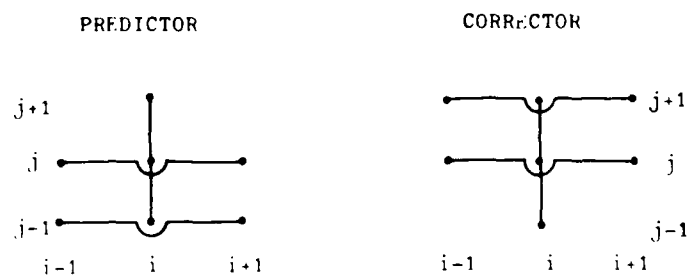


Figure 11. Graphical Representation of the Numerical Sweep Operators.

This scheme is also depicted graphically in Figure 11.

The MacCormack algorithm satisfies the requirements of stability, consistency, and accuracy if the following conditions are met: It is stable if the time step limit satisfies the CFL stability condition given in the next section. It is consistent if the sum of the time steps for each of the sweep operators is equal, and the algorithm is second order accurate if the sequence of sweep operators is symmetric.

STABILITY CONDITION

Although the stability of the finite difference equations cannot be analyzed when applied to the complete set of Navier-Stokes equations, MacCormack and Baldwin (23) have shown that considerable insight can be gained by separately analyzing the inviscid, diffusion, and mixed derivative parts of these equations. Stability criteria are determined by calculating the eigenvalues of the associated amplification matrix for each part. If this eigenvalue procedure is applied to the inviscid terms of the Navier-Stokes equations for flow in a Cartesian coordinate system, the following stability conditions emerge:

$$\Delta t_x \leq \frac{\Delta x}{|u| + c} \quad (3-15)$$

and

$$\Delta t_r \leq \frac{\Delta r}{|v| + c} \quad (3-16)$$

where c is the local speed of sound. Consideration of only the diffusive terms which contain $\partial^2 u / \partial x^2$ and $\partial^2 u / \partial r^2$ in the complete Navier-Stokes equations gives the conditions:

$$\Delta t_x \leq 1/2 \cdot \frac{\Delta x^2}{\frac{1}{r} \left(\frac{\mu}{Pr} + \frac{\epsilon}{Pr_t} \right)} \quad (3-17)$$

and

$$\Delta t_r \leq 1/2 \frac{\Delta r^2}{\lambda \left(\frac{u}{Pr} + \frac{\epsilon}{Pr_t} \right)} \quad (3-18)$$

Finally, analysis of the mixed derivative terms found in the Navier-Stokes equations gives the condition:

$$\Delta t_x = \Delta t_r \leq \frac{\Delta x \Delta r}{\frac{1}{c} [-(\lambda + \lambda_t) (\mu + \epsilon)]^{1/2}} \quad (3-19)$$

For the finite difference equations applied to the complete set of Navier-Stokes equations, the stability criteria can then be estimated as:

$$\Delta t \leq \min_{i,j} (\Delta t_x, \Delta t_r) \quad (3-20)$$

where

$$\Delta t_x \leq \frac{\Delta x}{|u| + c + \frac{1}{c} \left\{ \frac{2\gamma}{\Delta x} \left(\frac{\mu}{Pr} + \frac{\epsilon}{Pr_t} \right) + \frac{1}{\Delta x} [-(\lambda + \lambda_t) (\mu + \epsilon)]^{1/2} \right\}} \quad (3-21)$$

and

$$\Delta t_r = \frac{\Delta r}{|v| + c + \frac{1}{c} \left\{ \frac{2\gamma}{\Delta r} \left(\frac{\mu}{Pr} + \frac{\epsilon}{Pr_t} \right) + \frac{1}{\Delta x} [-(\lambda + \lambda_t) (\mu + \epsilon)]^{1/2} \right\}} \quad (3-22)$$

For the present non-Cartesian jet flow cases that were computed, the maximum time step was calculated as:

$$\Delta t = \min_{i,j} (\Delta t_x, \Delta t_n) \quad (3-23)$$

where

$$\Delta t_n = \frac{\Delta S_\xi}{|u_\xi| + c + \frac{1}{c} \left\{ \frac{2\gamma}{\Delta S_\xi} \left(\frac{\mu}{Pr} + \frac{\epsilon}{Pr_t} \right) + \frac{1}{\Delta S_n} [-(\lambda + \lambda_t) (\mu + \epsilon)]^{1/2} \right\}} \quad (3-24)$$

and

$$\Delta t_n = \frac{\Delta S_n}{|u_n| + c + \frac{1}{c} \left\{ \frac{2\gamma}{\Delta S_n} \left(\frac{\mu}{Pr} + \frac{\epsilon}{Pr_t} \right) + \frac{1}{\Delta S_n} [-(\lambda + \lambda_t) (\mu + \epsilon)]^{1/2} \right\}} \quad (3-25)$$

where

$$\Delta S_z = [(x_{i,j} - x_{i-1,j})^2 + (r_{i,j} - r_{i-1,j})^2]^{1/2} \quad (3-26)$$

$$\Delta S_\eta = [(x_{i,j} - x_{i,j-1})^2 + (r_{i,j} - r_{i,j-1})^2]^{1/2} \quad (3-27)$$

$$u_s = \text{Maximum } (u_{i,j}, v_{i,j}, u_{i-1,j}, v_{i-1,j}) \quad (3-28)$$

$$u_n = \text{Maximum } (u_{i,j}, v_{i,j}, u_{i,j-1}, v_{i,j-1}) \quad (3-29)$$

The actual time step used in the numerical procedure was less than this estimated maximum. Factors varying between 0.35 and 0.80 were used during the computations. Flow solutions involving relatively large viscous wakes containing recirculation regions required much smaller allowable time-steps with CFL factors on the order of 0.35-0.40.

NUMERICAL DAMPING

Strong shocks imbedded in a flowfield being solved computationally can often cause numerical oscillations (17) which may lead to program failure due to physically unrealistic values of computed pressure, density or temperature. These oscillations are caused by numerical truncation errors and can be reduced by refining the grid in the areas of shock locations. However, this can be impractical when the oscillations are of a transient nature caused by computational start-up or re-start procedures, or where the shock location varies for different experimental cases and mesh refinement for each individual case is undesirable. In this situation, a fourth order pressure-gradient damping concept as introduced by McCormack and Baldwin (23) can be applied to increase the stability of the numerical algorithm.

This damping scheme is applied in both the ξ and η directional

sweeps. In the ξ numerical sweep, damping is implemented by replacing $F_{ii,j}$ by $(F_{ii,j} + F_{D_{ii,j}})$ and $G_{ii,j}$ by $(G_{ii,j} + G_{D_{ii,j}})$ in equation (3-5). The predictor and corrector steps in this case are represented by $ii = i$ and $ii = i+1$, respectively. The damping terms F_D and G_D are in the following form:

$$F_{D_{ii,j}} = \alpha_\xi (|u_{ii,j}| + c_{ii,j}) \frac{|P_{i+1,j} - 2P_{i,j} + P_{i-1,j}|}{(P_{i+1,j} + 2P_{i,j} + P_{i-1,j})} \cdot (U_{i+1,j} - U_{i,j}) \quad (3-30)$$

and

$$G_{D_{ii,j}} = \alpha_\eta (|v_{ii,j}| + c_{ii,j}) \frac{|P_{ii,j+1} - 2P_{ii,j} + P_{ii,j-1}|}{(P_{ii,j+1} + 2P_{ii,j} + P_{ii,j-1})} \cdot (U_{ii,j+1} - U_{ii,j-1}) \cdot r_{ii,j}^{j_0} \quad (3-31)$$

In the η sweep, a similar procedure is implemented by replacing $F_{i,jj}$ by $(F_{i,jj} + F_{D_{i,jj}})$ and $G_{i,jj}$ by $(G_{i,jj} + G_{D_{i,jj}})$ where

$$F_{D_{i,jj}} = \alpha_\xi (|u_{i,jj}| + c_{i,jj}) \frac{|P_{i+1,jj} - 2P_{i,jj} + P_{i-1,jj}|}{(P_{i+1,jj} + 2P_{i,jj} + P_{i-1,jj})} \cdot (U_{i+1,jj} - U_{i-1,jj}) \quad (3-32)$$

and

$$G_{D_{i,jj}} = \alpha_\eta (|v_{i,jj}| + c_{i,jj}) \frac{|P_{i,j+1} - 2P_{i,j} + P_{i,j-1}|}{(P_{i,j+1} + 2P_{i,j} + P_{i,j-1})} \cdot (U_{i,j+1} - U_{i,j-1}) \cdot r_{i,jj}^{j_0} \quad (3-33)$$

In this case the predictor and corrector steps are represented by $jj = j$ and $jj = j+1$, respectively. For both sweeps α_ξ and α_η are damping constants where normally

$$\alpha_\xi = \alpha_\eta = 0.5 \quad (3-34)$$

This damping technique produces fourth order viscosity like terms of the form

$$a_\xi \Delta t \Delta \xi^3 \frac{\partial}{\partial \xi} \left[\frac{|u|+c}{4P} \left| \frac{\partial^2 P}{\partial \xi^2} \right| \frac{\partial U}{\partial \xi} \right] + a_\eta \Delta t \Delta \eta^3 \frac{\partial}{\partial \eta} \left[\frac{|v|+c}{4P} \left| \frac{\partial^2 P}{\partial \eta^2} \right| \frac{\partial U}{\partial \eta} \right]$$

which are added to the difference equations. The magnitude of these damping terms is proportional to the second derivative of pressure and is significant only in regions of pressure oscillation where the truncation error is already adversely affecting the solution.

3.3 CONVERGENCE CRITERIA

Convergence, as applied in this section, refers to iteration convergence as opposed to truncation convergence, which involves the convergence of the solution of the FDE to the solution of the PDE as Δx , Δr , and $\Delta t \rightarrow 0$. Iteration convergence refers to the arrival at a solution to the discretized Navier-Stokes equations within some acceptable tolerance through the use of an iterative process. As stated by Roache (17), there are no definitive criteria for iteration convergence. A somewhat subjective judgement of convergence must be made based upon an examination of the iterative behavior of the solution flow variables. Different flow variables, as well as variables at different locations, converge at different rates. If the slowest converging variable in the flow-field is known, it should be the most closely examined for convergence.

In the present case for a coflowing supersonic nozzle with a relatively thick base annulus, an examination of the flow variables revealed that the slowest converging variable was the base pressure of the nozzle annulus. The location of this base pressure is within

the subsonic flow area involving recirculation in the wake of the nozzle annulus as shown in figure 12. The flow variables in this subsonic region converged much more slowly than did those in the predominantly supersonic jet and freestream flows.

Since the coflowing nozzle problem primarily involves high Reynolds number flow, the advective terms in the conservation equations dominate the viscous diffusion terms. A characteristic time for a disturbance to cross the flowfield may then be characterized by:

$$\tau_{ch} = \frac{L}{u_{ch}} \quad (3-35)$$

where L is the length of the flowfield in the direction parallel to the characteristic velocity u_{ch} . For the jet problem u_{ch} was represented by u_∞ . Since in general the magnitude of u_∞ was less than u_{jet} , this gave a more conservative estimate of the characteristic time.

The convergence criteria was then established by the following procedure. The numerical solution was either initially started, or restarted from a previous case. As the solution converged, the base pressure was monitored until its magnitude varied less than $\pm 1\%$ for one characteristic time period. At the end of this characteristic time period the solution was stopped as convergence was achieved. Visual comparison of Mach Number and density profiles over the flowfield confirmed the convergence of the solution using this procedure. A sample base pressure convergence plot is shown in figure 13.

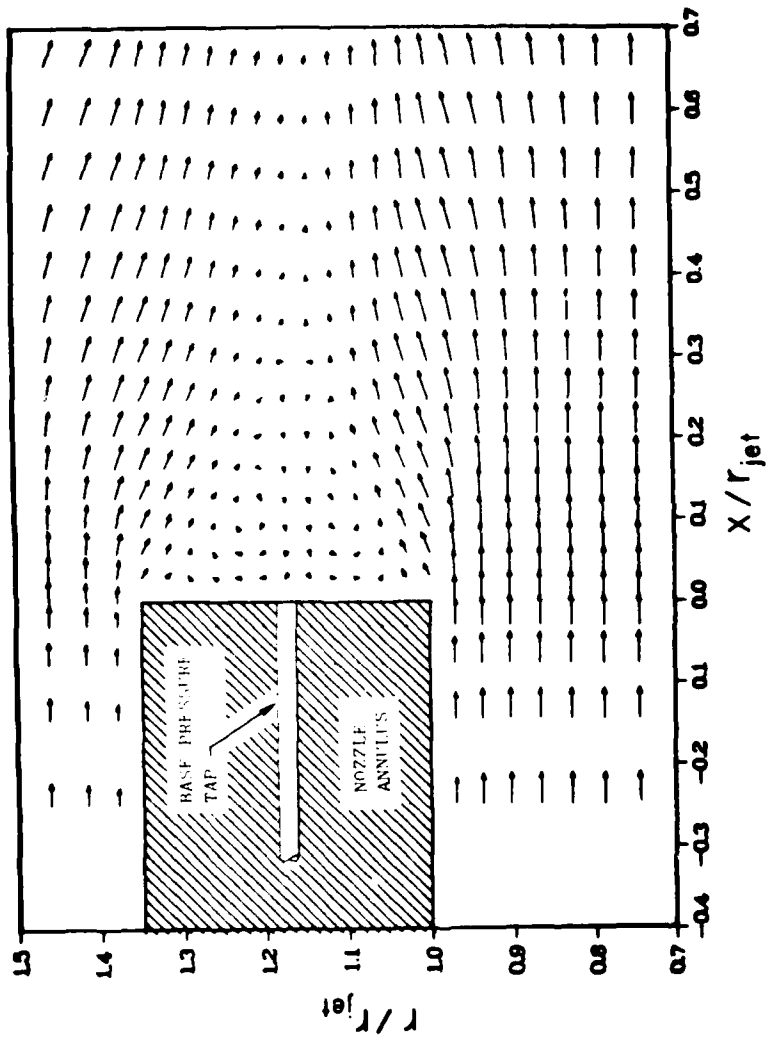


Figure 12. Base Pressure Tap Location in the Flowfield.

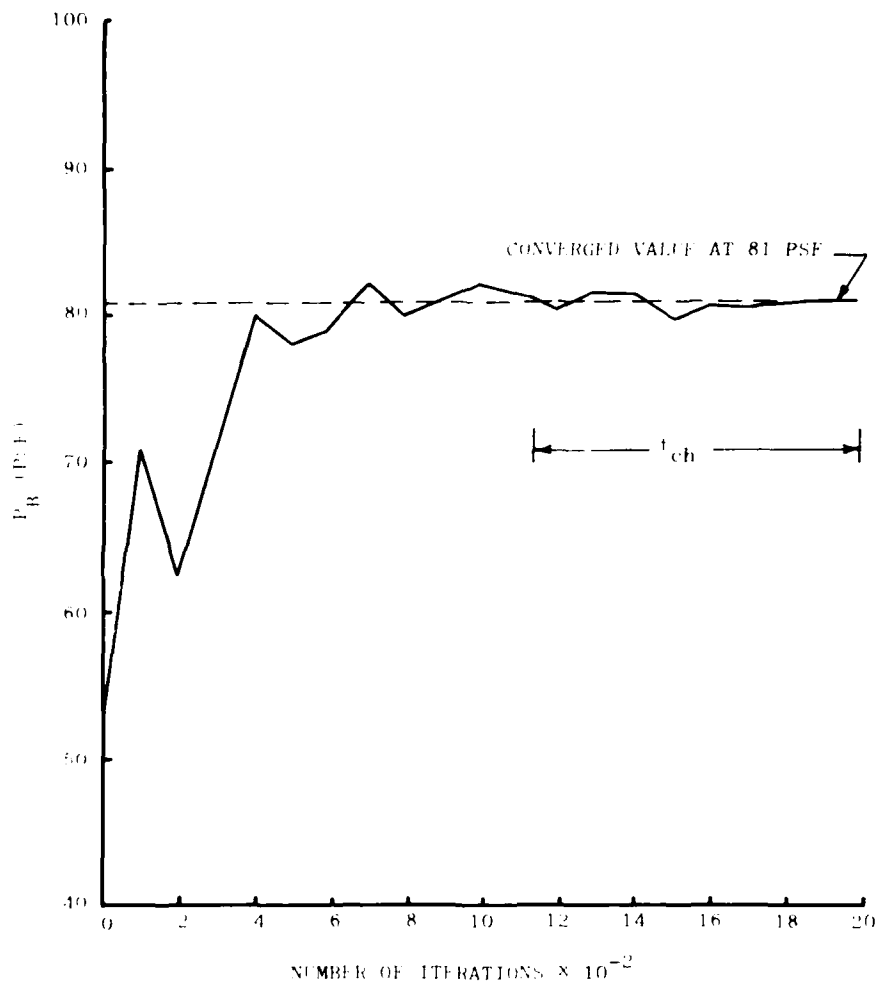


Figure 13. Typical Base Pressure Convergence, $P_j/P_\infty = 0.527$.

CHAPTER IV

BOUNDARY AND INITIAL CONDITION IMPLEMENTATION

As in chapter two, boundary and initial conditions must be defined in order to solve the conservation equations which govern the flowfield. Values of the dependent variables for points on the boundaries of the computational domain must be specified in order for the numerical operators to solve the flowfield correctly. This section presents the numerical formulation of the boundary and initial conditions used for the solution of the coflowing nozzle. The conditions were presented in a mathematical context in chapter two.

4.1 THE UPSTREAM BOUNDARY

The flow properties on the upstream boundary (AB and CD of Figure 6) are held fixed for the duration of the computational solution. The values of these properties were derived in the following manner. In the external flowfield, a parabolized Navier-Stokes solution (24) was computed for the ogive body used in the experimental coflowing nozzle tests as shown in Figure 14. This solution determined that the pressure gradient at the inflow boundary in the external flow stream is negligible, and that the static pressure at the inflow boundary is 99% of that in the undisturbed flow in the wind tunnel. The static pressure along the ogive body surface shown in Figure 15 was then used as an input to a two-dimensional turbulent boundary layer code (25, 26) along with the other specified freestream conditions (M_∞ , $T_{0\infty}$, Re_∞ , T_w) to produce

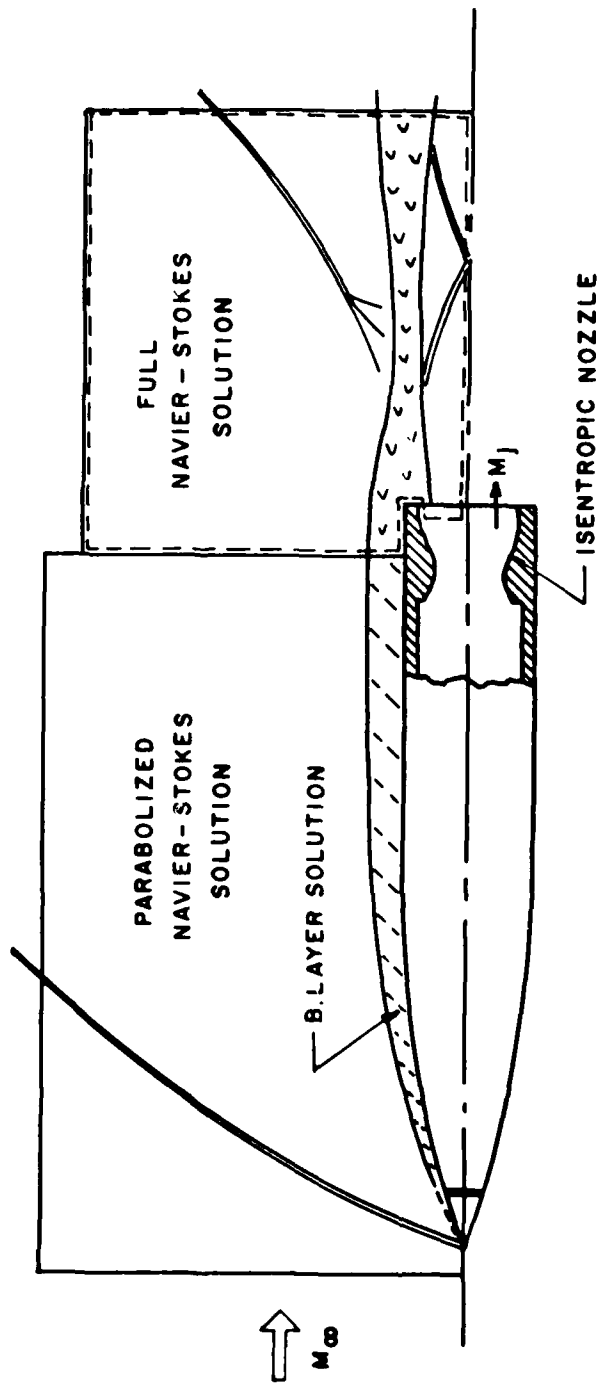


Figure 14. Flowfield schematic for a supersonic flowing axisymmetric nozzle.

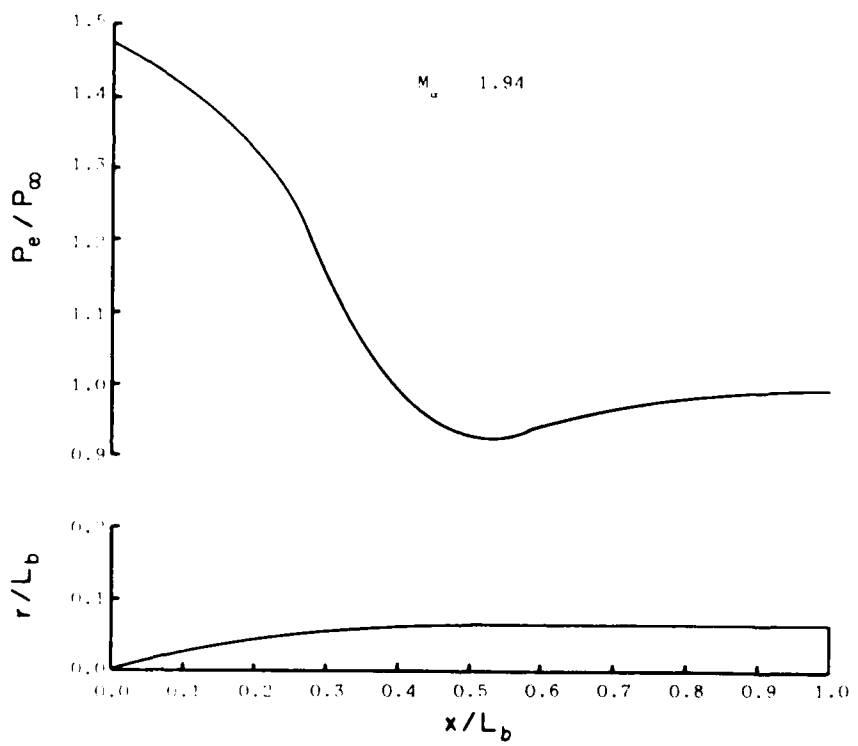


Figure 15. Computed Static Pressure Variation along the Ogive Body using a Parabolized Navier-Stokes Solver (23).

input velocity component and temperature profiles at the upstream boundary. The conservative variables on this boundary (CD) are then calculated using these profiles and the static pressure along the boundary. Flow variables on the upstream boundary in the jet flow (AB) are determined in a similar manner. The same boundary layer code is applied using the jet exit conditions and the length from the nozzle throat to the nozzle exit plane as the boundary layer starting length. Again, profiles for the velocity components and temperature are obtained along the boundary. Values for the conservative variables are then computed using these profiles and the value of the pressure at the jet exit. Since the value of the vertical velocity component is zero on the centerline boundary, a polynomial fit is used to set the vertical velocity profile from the edge of the boundary layer to the centerline.

4.2 THE UPPER BOUNDARY

The upper boundary, labeled DE on Figure 6, utilizes the simple wave procedure outlined by Roache (17, pp 282-283). This procedure assumes that properties are constant along a straight, left-running characteristic line passing through each point on the upper boundary. The position of this line running through a boundary point (i, JL) is determined by the angle ($\mu_M + \phi$), where

$$\mu_M = \arcsin (1/M_{i,j}) \quad (4-1)$$

is the local Mach angle for supersonic flow, and

$$\phi = \arctan (v/u) \quad (4-2)$$

is the local flow direction. The properties on this characteristic

line are determined by linear interpolation involving the properties at points $(i-1, JL)$, $(i-1, JL-1)$, and $(i, JL-1)$ as shown in Figure 16. Points $(i-1, JL-1)$ and $(i, JL-1)$ are points interior to the computational domain, and point $(i-1, JL)$ is either a point on the inflow boundary ($i = 1$) or a previously defined point on the upper boundary resulting from the left to right sweep along the boundary using this technique.

As shown in Figure 16, one of two possible interpolation schemes is applied depending on the local values of the quantities $(\mu_M + \epsilon)$ and $(\Delta r / \Delta x)$. For the case of $\tan(\mu_M + \epsilon)_{i-1, JL-1} > \Delta r / \Delta x$, the position of the characteristic line lies between the points $(i-1, JL-1)$ and $(i, JL-1)$. The properties at the point p , and thus at point (i, JL) , can then be determined by:

$$f_{i,JL} = f_p = f_{i-1,JL-1} + \left(\frac{\ell}{\Delta x}\right)(f_{i,JL-1} - f_{i-1,JL-1}) \quad (4-3)$$

The value of ℓ , and thus the position of the point p , can be determined by the following procedure. If the quantity w is defined by:

$$w = \tan[90^\circ - (\mu_M + \epsilon)] \quad (4-4)$$

then by geometry:

$$w_p = (\ell x - s) / \Delta r \quad (4-5)$$

If the interpolation procedure of equation (4-3) is applied, then

$$w_p = w_{i-1,JL-1} + \left(\frac{\ell}{\Delta x}\right)(w_{i,JL-1} - w_{i-1,JL-1}) \quad (4-6)$$

Equating (4-5) to (4-6) and solving for s gives:

$$s = \frac{(\ell x / \Delta r) - w_{i-1,JL-1}}{(w_{i,JL-1} - w_{i-1,JL-1}) / \Delta x + (1 / \Delta r)} \quad (4-7)$$

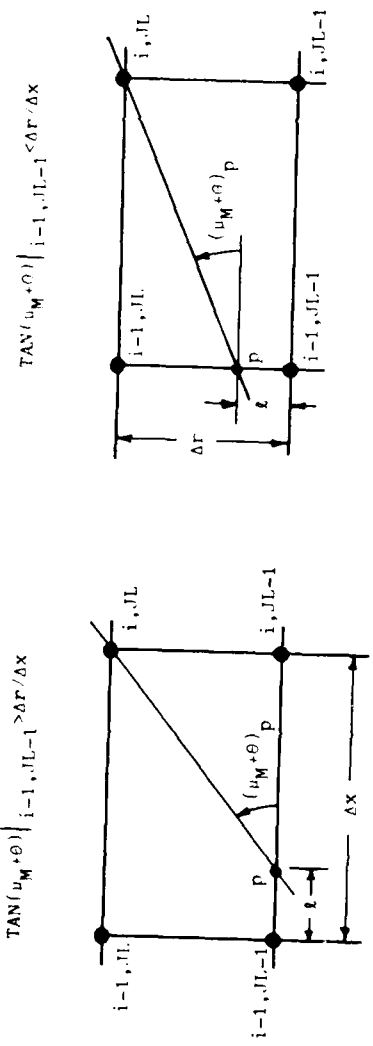


Figure 16. Upper Boundary Condition schematic.

For the alternate case of $\tan(\beta_m + \beta)_{i-1, JL-1} < (\Delta r / \Delta x)$ the position of the characteristic line lies between the points (i-1, JL-1) and (i-1, JL). The properties at p are then determined by the equation:

$$f_{i, JL} = f_p = f_{i-1, JL-1} + (\beta / \Delta r)(f_{i-1, JL} - f_{i-1, JL-1}) \quad (4-8)$$

In this case, the quantity w is defined as

$$w = \tan(\beta_m + \beta) \quad . \quad (4-9)$$

and by geometry

$$w_p = (\Delta r - \beta) / \Delta x \quad (4-10)$$

The interpolation scheme for w_p now gives the expression:

$$w_p = w_{i-1, JL-1} + (\beta / \Delta r)(w_{i-1, JL} - w_{i-1, JL-1}) \quad (4-11)$$

Again, equating (4-10) to (4-11) and solving for β gives:

$$\beta = \frac{(\Delta r / \Delta x) - w_{i-1, JL-1}}{(w_{i-1, JL} - w_{i-1, JL-1}) / \Delta r + (1 / \Delta x)} \quad (4-12)$$

Applying the computed values of the interpolation length to the respective interpolation equation (either (4-3) or (4-8)) gives the proper value of the desired flow variable at the boundary point (i, JL).

4.3 THE DOWNSTREAM BOUNDARY

The downstream boundary (EF) is placed in a region where gradients in the flow variables are expected to exist. A quadratic extrapolation can be used on this boundary that lets $\partial^2 f / \partial x^2$ and $\partial^2 f / \partial x^2$ be nonzero, thus satisfying this gradient condition. Assuming a constant grid spacing Δx near this boundary, Taylor series expansions can be performed in the following manner from a point (IL, j) on the boundary to the following three points interior to the boundary:

$$f_{IL-1,j} = f_{IL,j} + \Delta x \frac{\partial f}{\partial x} \Big|_{IL,j} + \frac{\Delta x^2}{2} \frac{\partial^2 f}{\partial x^2} \Big|_{IL,j} + O(\Delta x^3) \frac{\partial^3 f}{\partial x^3} \Big|_{IL,j} \quad (4-13)$$

$$f_{IL-2,j} = f_{IL,j} + 2\Delta x \frac{\partial f}{\partial x} \Big|_{IL,j} + 2\Delta x^2 \frac{\partial^2 f}{\partial x^2} \Big|_{IL,j} + O(\Delta x^3) \frac{\partial^3 f}{\partial x^3} \Big|_{IL,j} \quad (4-14)$$

$$f_{IL-3,j} = f_{IL,j} + 3\Delta x \frac{\partial f}{\partial x} \Big|_{IL,j} + \frac{9\Delta x^2}{2} \frac{\partial^2 f}{\partial x^2} \Big|_{IL,j} + O(\Delta x^3) \frac{\partial^3 f}{\partial x^3} \Big|_{IL,j} \quad (4-15)$$

If the assumption is made that the last term in each equation can be neglected, i.e.

$$\Delta x^3 \frac{\partial^3 f}{\partial x^3} = 0 \quad (4-16)$$

then equations (4-13) through (4-15) can be solved simultaneously to give the following expression for the boundary point (IL, j) in terms of the interior points:

$$f_{IL,j} = 3f_{IL-1,j} - 3f_{IL-2,j} + f_{IL-3,j} \quad (4-17)$$

This condition works well as long as large pressure gradients do not exist at this boundary, as in the case when a normal shock wave exits the boundary. If this does occur, the term involving $\partial^3 f / \partial x^3$ is no longer negligible. Equation (4-17) then can become numerically unstable.

Numerical divergence did occur when the previous extrapolation condition was applied to regions of subsonic flow present at this outflow boundary. Therefore, the following first order, zero gradient condition was applied at points (IL, j) when the Mach number at points (IL-1, j) was found to be subsonic:

$$f_{IL,j} = f_{IL-1,j} \quad (4-18)$$

4.4 THE CENTERLINE

The centerline boundary (AF in Figure 6) is a line of symmetry

with no mass or energy flux across it. The vertical velocity component condition (eqn 2-36) is applied by setting:

$$v_{i,1} = 0 \text{ for } 1 \leq i \leq IL \quad (4-19)$$

The symmetry conditions for the density and u component of velocity (eqns 2-37 and 2-38) which are valid only at the centerline are applied in the following manner. Taylor series expansions are performed for ρ and u from a centerline boundary point $(i,1)$ to points $(i,2)$ and $(i,3)$ which are distances Δr and $K\Delta r$, respectively, above the centerline boundary. The series expansions to these points give the following equations for density:

$$\rho_{i,2} = \rho_{i,1} + \Delta r \frac{\partial \rho}{\partial r} \Big|_{i,1} + \frac{\Delta r^2}{2} \frac{\partial^2 \rho}{\partial r^2} \Big|_{i,1} + O(\Delta r^3 \frac{\partial^3 \rho}{\partial r^3}) \Big|_{i,1} \quad (4-20a)$$

$$\rho_{i,3} = \rho_{i,1} + K\Delta r \frac{\partial \rho}{\partial r} \Big|_{i,1} + \frac{K^2 \Delta r^2}{2} \frac{\partial^2 \rho}{\partial r^2} \Big|_{i,1} + O(\Delta r^3 \frac{\partial^3 \rho}{\partial r^3}) \Big|_{i,1} \quad (4-20b)$$

If the centerline symmetry condition (2-37) is applied and the higher order term in each equation is neglected, these two equations can be solved simultaneously to obtain:

$$\rho_{i,1} = \frac{\kappa^2 \rho_{i,2} - \rho_{i,3}}{(\kappa^2 - 1)} \quad (4-21a)$$

A similar expression can be obtained for the u component of velocity:

$$u_{i,1} = \frac{\kappa^2 u_{i,2} - u_{i,3}}{(\kappa^2 - 1)} \quad (4-21b)$$

The previous extrapolation boundary conditions for the density and the horizontal velocity component were applied only to regions of supersonic flow at the centerline. Undesirable pressure wiggles occurred if these conditions were applied to regions of subsonic flow. The following first order zero gradient condition was applied at the centerline points

(i,1) when the Mach number at points (i,2) was found to be subsonic

$$c_{i,1} = c_{i,2} \quad (4-22a)$$

$$u_{i,1} = u_{i,2} \quad (4-22b)$$

Since the v component of velocity is zero on the centerline, this boundary can be considered as a streamline. As discussed in chapter 2, the stagnation enthalpy is then constant on this boundary.

Since the total enthalpy at the inflow boundary is known, then

$$H_o|_{i,1} = H_o|_{1,1} \text{ for } 1 < i \leq IL \quad (4-23)$$

Since the value of $u_{i,1}$ has been previously determined by equation (4-22), the definition of the stagnation enthalpy can be expanded to determine the value of temperature at each boundary point (i,1):

$$T_{i,1} = T_{1,1} + [(u_{1,1})^2 - (u_{i,1})^2]/2C_p \quad (4-24)$$

The values of the primitive variables ρ , u , v , and T have now been determined for each centerline boundary point, so that the required values of the conservative variables can be computed along this boundary.

4.5 THE NOZZLE WALLS

The nozzle walls (BG, GH, and CH in Figure 6) are treated as no-slip, impermeable boundaries. The no-slip condition is imposed on the three wall faces by imposing the following conditions (see Figure 17):

Inner wall

$$u_{i,JWI} = v_{i,JWI} = 0 \text{ for } 1 < i \leq IW \quad (4-25a)$$

Outer wall:

$$u_{i,JWO} = v_{i,JWO} = 0 \text{ for } 1 < i \leq IW \quad (4-25b)$$

Base (vertical) wall:

$$u_{IW,j} = v_{IW,j} = 0 \text{ for } JWI < j < JWO \quad (4-25c)$$

As discussed in chapter 2, a constant wall temperature is imposed on the nozzle walls. This condition is applied simply as:

$$T_{i,JWI} = T_{i,JWO} = T_W \text{ for } 1 < i \leq IW \quad (4-26a)$$

and

$$T_{IW,j} = T_W \text{ for } JWI < j < JWO \quad (4-26b)$$

A first order pressure gradient condition derived from equation (2-42) is applied on each wall. This is imposed as:

$$p_{i,JWI} = p_{i,JWI-1} \text{ for } 1 < i < IW \quad (4-27a)$$

$$p_{i,JWO} = p_{i,JWO+1} \text{ for } 1 < i < IW \quad (4-27b)$$

$$p_{IW,j} = p_{IW+1,j} \text{ for } JWI < j < JWO \quad (4-27c)$$

Since the points (IW, JWI) and (IW, JWO) are positioned at sharp corner points, the simple pressure condition applied in equation (4-27) is not applicable. An averaging scheme was therefore used to allow the pressure to adjust at the corners. This averaging is applied as:

$$p_{IW,JWI} = (p_{IW,JWI-1} + p_{IW+1,JWI})/2 \quad (4-28a)$$

and

$$p_{IW,JWO} = (p_{IW,JWO+1} + p_{IW+1,JWO})/2 \quad (4-28b)$$

The primitive variables u , v , P , and T have now been defined

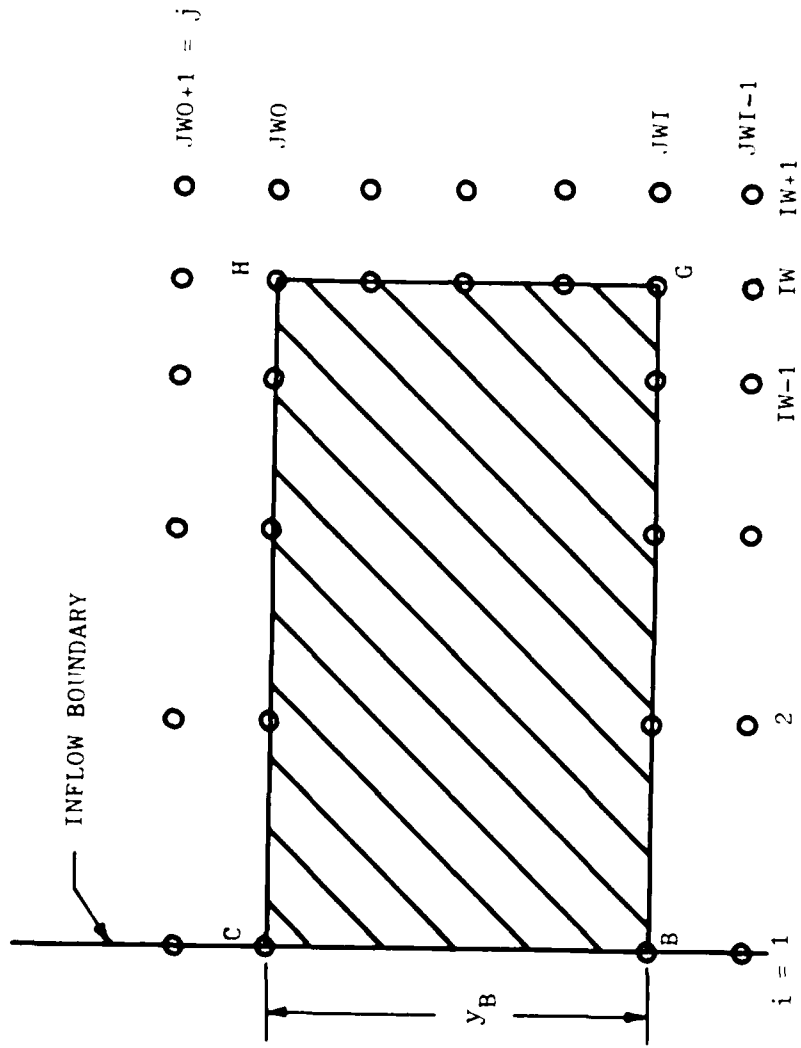


Figure 17. Finite Difference Mesh Near the Nozzle Walls.

on the wall boundaries. The required values of the conservative variables can then be computed on this boundary.

4.6 INITIAL CONDITIONS

As discussed in chapter 2, initial values of the conservative variables must be imposed over the computational domain. Since the incoming flow variables are fixed in time, they are initially imposed over the complete computational domain as follows:

$$U_{i,j}^{\circ} = U_{1,j}^{\circ}, \quad j \leq JWI \text{ and } JWO \leq j \quad (4-29)$$

The value of the u component of velocity in the wake region ($JWI \leq j \leq JWO$) would be zero from the input profile. Therefore, the u component in the wake is set to grow exponentially using the following equation:

$$u_{i,j}^{\circ} = k_o(1 - e^{[(x_{IW,j} - x_{i,j})/y_B]}) \quad (4-30)$$

where

$$k_o = u_{1,JWI-1}^{\circ} + (u_{1,JWO+1}^{\circ} - u_{1,JWI-1}^{\circ}) \frac{(r_{1,j} - r_{1,JWI-1})}{(r_{1,JWO+1} - r_{1,JWI-1})} \quad (4-31)$$

for $IW \leq i \leq IL$ and $JWI \leq j \leq JWO$. Use of this scheme allows the velocity in the far wake to be close to that of the two streams, thus accelerating convergence.

Once an initial case of the coflowing nozzle had numerically converged to a valid solution, each succeeding case was initialized by imposing a new jet input profile on the inflow boundary of the preceding converged solution. This technique allowed the new solution to converge at a much greater rate, since the subsonic recirculation zone in the near wake was already in existence from the previous solution.

CHAPTER V

TURBULENCE MODELING

The experimental tests used as a basis for the computational solutions were conducted at a Reynolds number of 2.2×10^6 , based on the ogive body length and the external flow conditions. The external flow in the region of the nozzle is thus expected to be of a fully turbulent nature. Reynolds numbers in the interior jet flow covered a range from 1×10^5 to 1.7×10^6 , based on nozzle exit conditions and the nozzle throat to exit plane length. Considering the effects of compressibility and the existence of a favorable pressure gradient in the divergent portion of the nozzle, a transition Reynolds number of 5×10^5 was used to determine the condition at which the jet flow possessed turbulent characteristics (27).

The turbulent nature characteristic of these flows can be accounted for in the computational solution by a variety of eddy viscosity models ranging from locally dependent algebraic models to the more complex higher-order closure models such as the turbulent kinetic energy methods. Although the higher order methods can account for the time history of the turbulence in a flow, they require that accurate initial profiles of the turbulent shear stress be known or reliably calculated (28). If this initial profile condition cannot be satisfied, then this type of prediction method cannot be effectively utilized. Since this proved to be the case for the jet problem under consideration, locally dependent eddy viscosity models were carefully applied over the computational domain.

As shown in Figure 18, the computational domain contains three distinct regions in which various eddy viscosity models are applied. These regions consist of an area containing boundary layers, a far wake region downstream of the nozzle exit, and a near wake region close to the nozzle exit plane.

5.1 BOUNDARY LAYER MODEL

In the first region, the dominating flow features are the boundary layers along the nozzle walls. Since the experimental boundary layer thicknesses are at least an order of magnitude smaller than the nozzle radius, a two-dimensional turbulence model was judged to be sufficient for the axisymmetric cases. The eddy viscosity model applied in this region is a two layer Cebeci-Smith model (29). The inner layer of this model accounts primarily for the laminar sublayer adjacent to the wall, with the outer layer accounting for the remainder of the boundary layer region.

The expression for the inner model is based on Prandtl's mixing-length theory, which can be written as:

$$\epsilon_i = \rho_i^2 \left| \frac{\partial u_t}{\partial r_n} \right| \quad (5-1)$$

where u_t is the local tangential velocity parallel to the wall surface, and r_n is the normal distance measured from the wall. The mixing length in this model is adapted from Van Driest's sublayer model, and is expressed as:

$$l_i = 0.4 r_n (1 - e^{-\frac{r_n \sqrt{\rho t_w}}{26\mu}}) \quad (5-2)$$

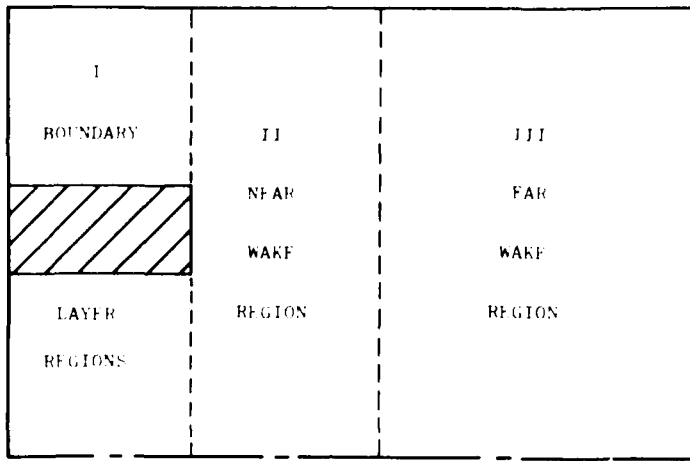


Figure 18. Eddy Viscosity Model Domains.

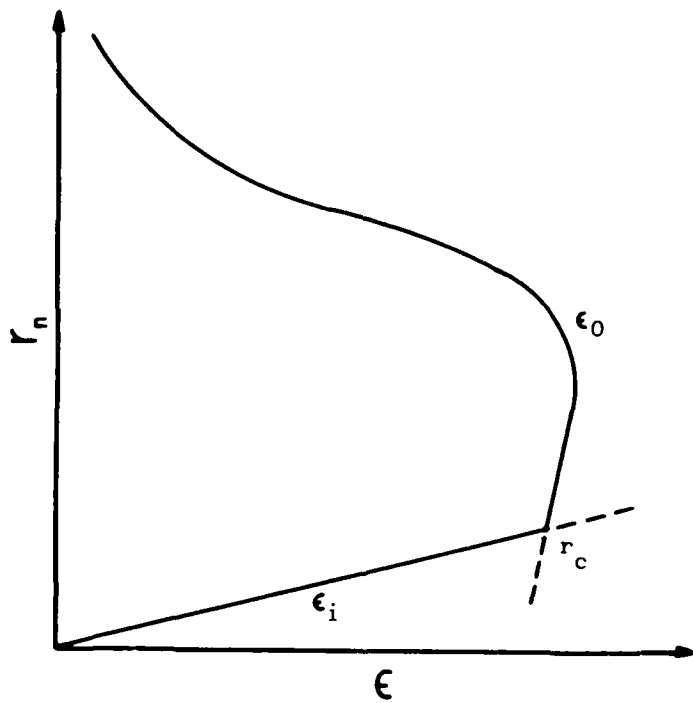


Figure 19. Eddy Viscosity Distribution Across a Boundary Layer.

This inner model assumes the flat plate pressure condition ($dp/dx = 0$), but could be modified to account for a pressure gradient in the direction parallel to the wall within the sublayer.

The outer region eddy viscosity model consists of a Clauser-type displacement thickness model defined by the equation:

$$\epsilon_o = 0.0168 \cdot u_e \cdot \delta^* \gamma_1 \quad (5-3)$$

where u_e is the appropriate tangential velocity at the boundary-layer edge and

$$\delta^* = \int_0^\delta \left(1 - \frac{u_t}{u_e}\right) dr_n \quad (5-4)$$

is the incompressible displacement thickness. This model also includes Klebanoff's intermittency factor γ_1 defined by the following equation:

$$\gamma_1 = [1 + 5.5 \cdot (y/\delta)^6]^{-1} \quad (5-5)$$

The inner and outer regions of each boundary layer are defined by the requirement that the eddy viscosity remain continuous across the entire layer. This is accomplished by applying the inner model outward from the wall until $\epsilon_i = \epsilon_o$ at a value r_c . The outer model is then applied from r_c outward across the remainder of the flowfield. In the boundary layer region. Figure 19 shows a typical eddy viscosity profile across this region.

5.2 FAR WAKE MODEL

In the region downstream of the nozzle exit, the initial boundary layers on the nozzle walls merge to form a shear layer containing an imbedded wake region. This region in the flowfield can be further divided into two separate areas: the near wake region close to the nozzle exit that contains flow features such as the corner expansions, a "deadwater" zone, recompression shocks, and the far wake region further

downstream where the flow eventually tends to a similar free shear layer type of flow. The eddy viscosity model for the far wake region will be discussed in this section, and then be extended for the near wake region in the next section.

The eddy viscosity in the far wake region is in the form of the following Prandtl mixing length model:

$$\varepsilon = \rho^2 |\omega| \quad (5-6)$$

where ω is defined as the vorticity

$$\omega = \nabla \times \vec{u} = \frac{\partial u}{\partial y} - \frac{\partial v}{\partial x} \quad (5-7)$$

and the mixing length ℓ uses the same formulation as that of Dash, et al (30,31) in their wake mixing length model for the core region of a co-flowing nozzle:

$$\ell = 0.065 \delta_w \quad (5-8)$$

In this model, δ_w is the representative thickness of the shear layer at any axial position in the wake. This model accounts for the variation in eddy viscosity across the mixing layer through its dependence on the local value of vorticity. As in the eddy viscosity model utilized by Baldwin and Lomax (32), the vorticity profile across the mixing layer can be utilized to determine the thickness parameter δ_w . This eliminates the somewhat complicated process of finding the outer edges of the shear layer based on velocity profiles for each axial position in the computational flowfield.

For the axisymmetric coflowing nozzle cases that were solved numerically, the maximum absolute value of vorticity in the wake was found to be in the following range:

$$1 \times 10^5 < |\omega_{max}| < 1 \times 10^6 \text{ sec}^{-1} \quad (5-9)$$

The cutoff value used to define a representative edge of the mixing layer was:

$$|\omega_{\text{edge}}| = 1 \times 10^4 \text{ sec}^{-1} \quad (5-10)$$

This value gave a reasonable value of δ_w as shown by a typical vorticity profile in Figure 20. The absolute value of vorticity typically dropped to less than one percent of $|\omega_{\max}|$ within one gridpoint outside of the cutoff point.

A flat plate validation case was computed using the far wake model to check its accuracy in a known turbulent flowfield. The data of Toyoda and Kuriyama (33) for a flat plate in turbulent flow at a Mach number of 1.6 was used as the basis for a computational solution. The velocity defect in the wake obtained both experimentally and numerically is shown in Figure 21. As shown by this figure, the results generated by the numerical turbulence model compared very well with the thin flat plate data. Further details of this computation are listed in Appendix C.

5.2 NEAR WAKE MODEL

The accuracy of a Prandtl type mixing length turbulence model is substantially dependent on the use of length scales that are truly representative of the flow in a given region. In the far wake region where a single mixing layer exists, the previous definition of the length scale involving δ_w is valid. However, for the case of a coflowing nozzle with a thick base annulus, several length scales need to be defined in the near wake region. As shown in Figure 22, the existence of the subsonic, recirculating "dead water" region adjacent to the nozzle base wall complicates the flow simulation. In the near wake, the length scales must transition from the appropriate boundary layer thickness

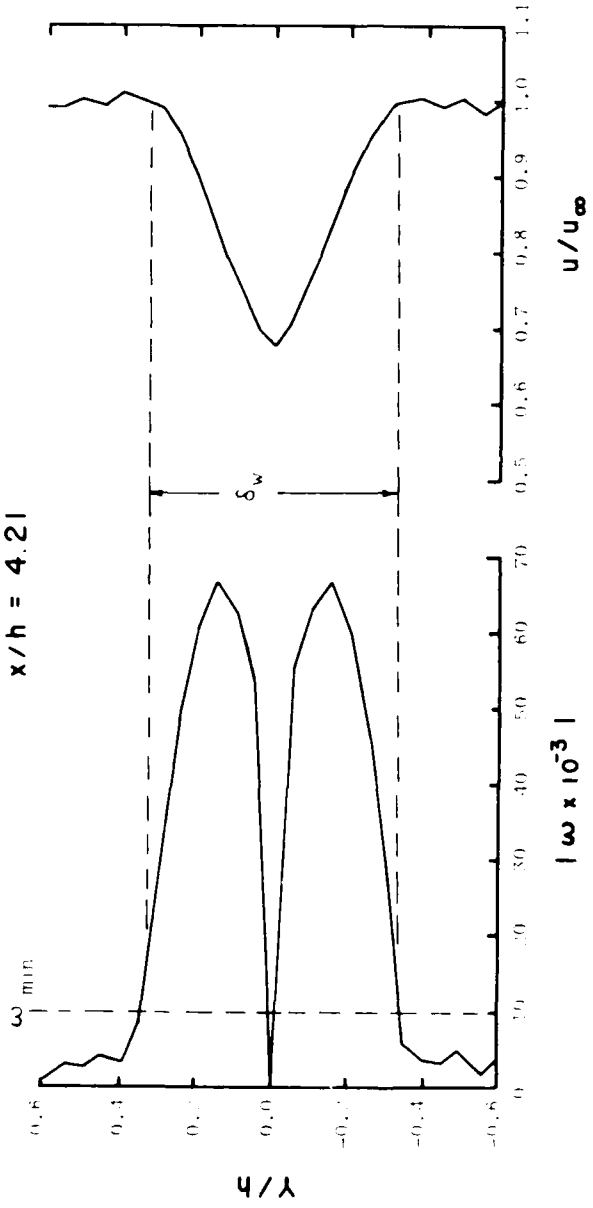


Fig. 1. u/u_{∞} , Typical Velocity Profile Used to Compute Mixing Layer Thickness.

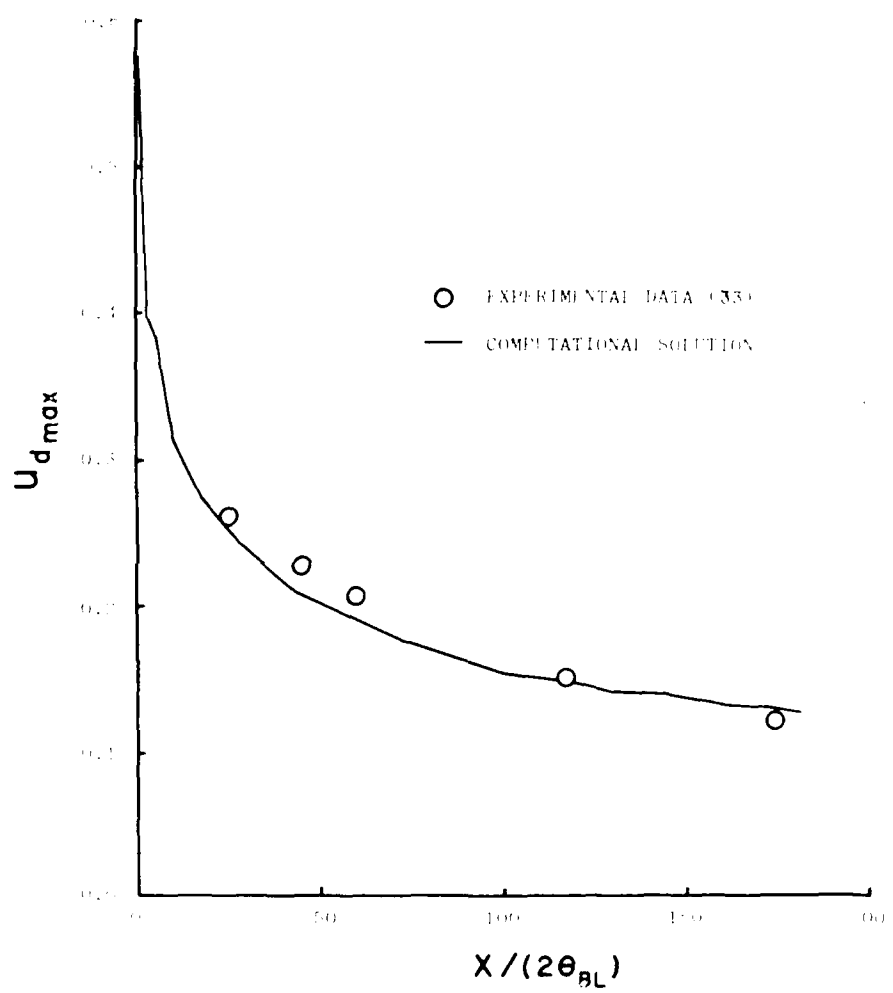


Figure 21. Maximum Velocity Defect vs. Distance Behind the Trailing Edge of a Two-Dimensional Flat Plate, $M_\infty = 1.60$.

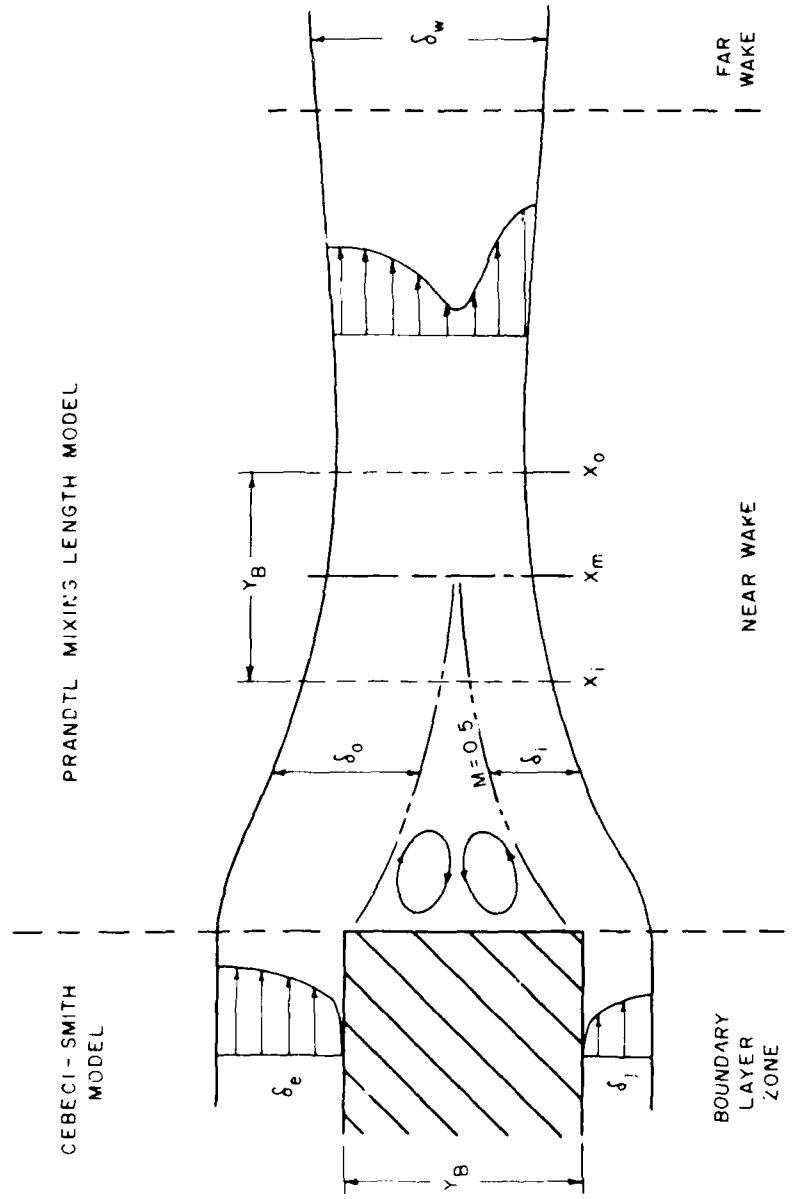


Figure 22. Viscous Layer structure in the Near Wake.

at the nozzle exit plane to the single mixing layer thickness (δ_w) that exists in the far wake region.

This transition is accomplished using the following procedure. The exterior edges of the mixing layers in the near wake are determined using the vorticity limits previously defined for the far wake. The interior edges of the dual shear layers are then defined by the Mach 0.5 contour line surrounding the "dead water" region as shown in Figure 22. The vorticity turbulence model defined by equations 5-6 and 5-8 is then applied in the near wake region from the end of the boundary layer zone to the start of the initial mixing zone with

$$\delta = \delta_o \text{ in the free stream flow}$$

$$\delta = \delta_i \text{ in the jet stream flow}$$

$$\delta = 0.5 (\delta_o + \delta_i) \text{ inside the Mach 0.5 contour of the "dead water" region}$$

An initial mixing zone, one base height in length, is used to smoothly adjust the thickness of the dual shear layers (δ_o and δ_i) that exist in the expansion and recompression zones of the near wake region to that of the single shear layer (δ_w) in existence further downstream. The following exponential equation is applied in this region:

$$\delta(x) = \delta_w|x_{x_0} - (\delta_w|x_{x_0} - \delta_o \text{ or } j|x_{x_i}) e^{-k_1} \quad (5-11)$$

where k_1 is determined by the expression

$$k_1 = 2 \left(\frac{x_m}{y_B} - \frac{x}{y_B} - 0.5 \right) \quad (5-12)$$

and the value of x lies in the following range:

$$x_m - 0.5y_B < x < x_m + 0.5y_B$$

The point x_m is centered in the mixing region. It was determined that the position of the midpoint x_m must be specified. If allowed to float,

the near wake eddy viscosity region stretched to unrealistic lengths and gave erroneous values of nozzle base pressure. Using the very slightly underexpanded experimental case ($P_j/P_\infty = 1.03$) as a basis, the midpoint x_m was varied to obtain its effect on nozzle base pressure. As shown in Figure 23, the value

$$x_m/y_B = 2.0$$

gave the best agreement with the experimental data. This value was then fixed for the entire series of flow calculations at the various pressure ratios.

A two-dimensional wedge-flat plate validation case was computed in order to obtain the accuracy of the turbulence model in the near wake and transition zone to the far wake. The data of Rom, Seginer, and Kronzon (34, 35) for a one centimeter thick wedge-flat plate in turbulent flow at a mach number of 2.25 was used as the basis for a computational solution.

All of the near wake features were accurately reproduced by the computational solution, and are discussed in Appendix D. Both the static pressure axially along the line of symmetry and the pitot pressure profiles in the near wake are in good agreement with the experimental data. The variation in the mixing length (δ) used in the turbulence model is shown in Figure 24. This figure exhibits the correct physical behavior of the growth of δ as the flow expands around the corner and the subsequent decrease in δ as the flow recompresses in the near wake region. The exponential growth in the transition region is also evident. This case confirms that the eddy viscosity model used in the coflowing nozzle is a reasonable one that should account for the turbulence effects in a correct manner.

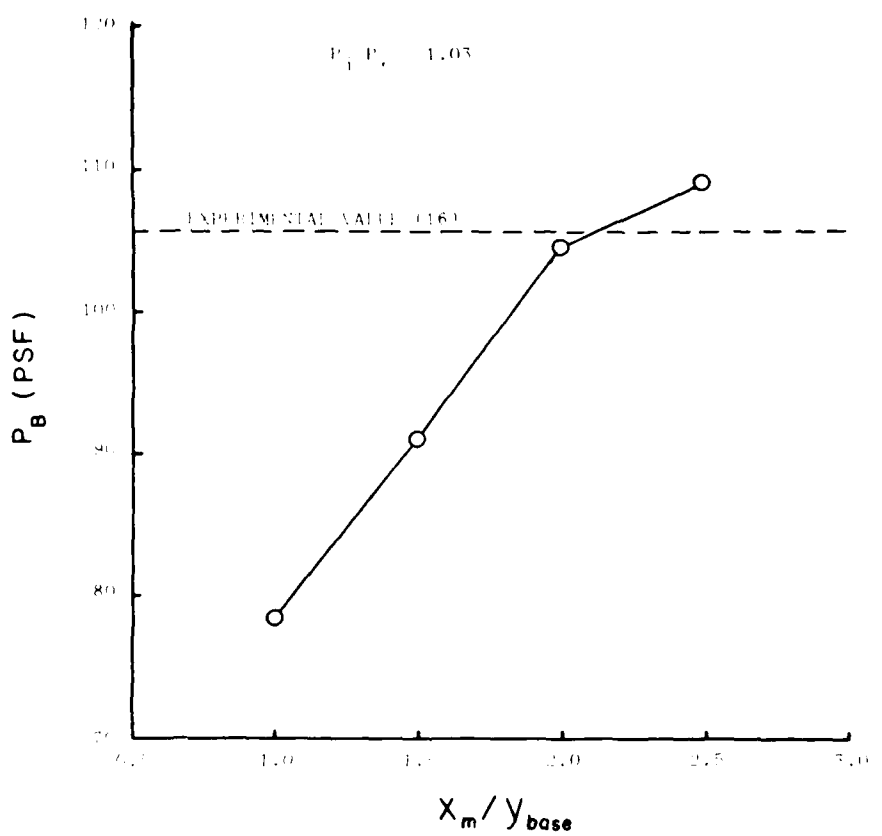


Figure 23. Computed Nozzle Base Pressure vs the Position of the Mixing Region Midpoint x_m .

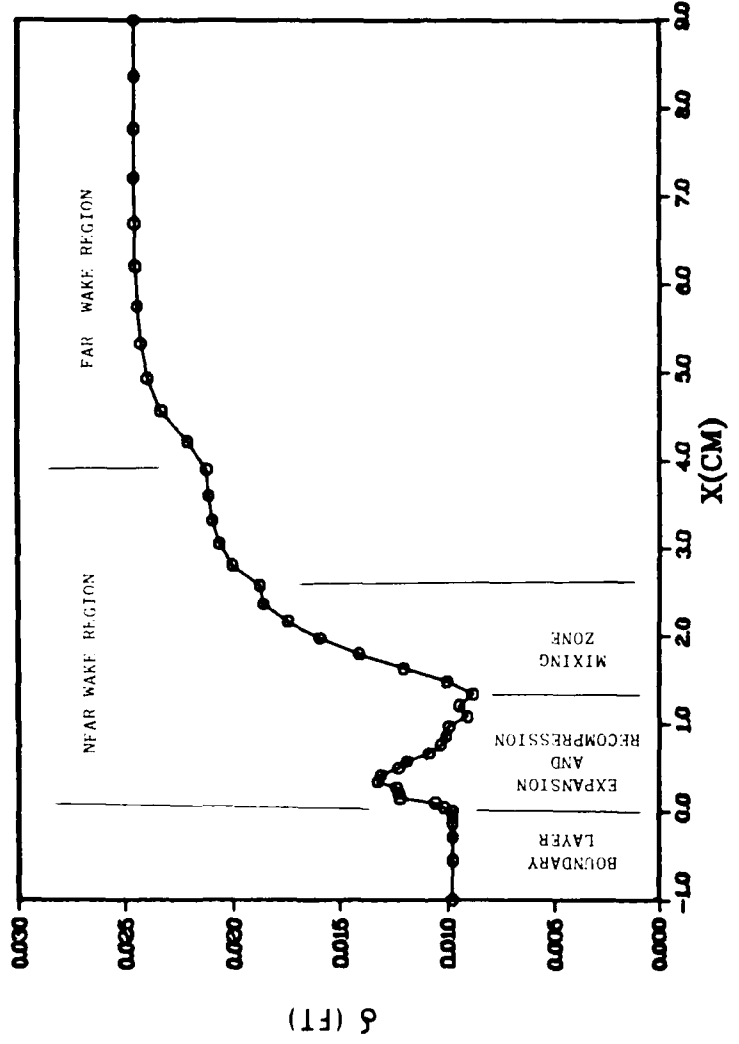


Figure 24. Computed Mixing Layer Thickness Used in the Wake Turbulence Model for the Wedge-Flat Plate Case.

CHAPTER VI

NUMERICAL RESULTS

This chapter will discuss the numerical results of the computational solutions using the algorithm, boundary conditions, and turbulence modeling detailed in previous chapters. The first section of this chapter will discuss the experimental cases taken as the basis for comparison with the numerical solutions for the coflowing nozzle. The next section discusses details involved in the actual computational procedure. The last section covers the comparison between the experimental and computational solutions, including some analyses of the accuracy of the simulations and discrepancies between the numerical solutions and the experimental data.

6.1 Experimental Data Base

As outlined in Chapter 1, the data of Bromm and O'Donnell (16) is used as the experimental basis for this research effort. Supersonic fields of flow generated experimentally contain both highly viscous flow regions as well as shock structures ranging from weak regularly reflected shock waves to the strong Mach disc shock formation. Five different experimental nozzle pressure ratio conditions are used as the basis for the computational solutions. Nozzle base pressure measurements and schlieren photographs are the basis for experimental versus computational comparisons.

Model

The model, a stainless steel body of revolution, consisted of

a 16.25 inch ogive forebody and a one inch diameter cylindrical afterbody (see Figure 15). The total length of the model was 7.5 inches. The model was supported by a 10% thick hollow side strut that acted as a conduit for the air flow to the jet as shown in Figure 5. The effects of this strut were found to be negligible on the flow field downstream. This model was fitted with a nozzle which gave essentially isentropic flow with an exit Mach number of 3.00. The inner diameter of this nozzle at the exit plane was 0.742 inches, and the length from the nozzle throat to the exit plane was 1.20 inches. Four base pressure orifices were used to obtain the base pressure measurements as shown on Figure 5.

External Flow

The external flow conditions were generated in the NASA Langley 9-inch supersonic wind tunnel. The free stream Mach number was set at 1.94, and the free stream Reynolds number was fixed at 2.2×10^6 based on the body length of the model. A turbulent boundary layer on the model at these conditions was insured through the use of a transition strip near the nose. The tests were conducted at a tunnel stagnation pressure of one atmosphere (assumed to be 2116 psf). Using these given conditions, the stagnation temperature of the free stream was calculated to be equal to 580.5°R.

Jet Flow

The flow just upstream of the jet exit plane was given to be at a Mach 3, zero divergence angle condition. The total pressure in the jet flow was varied to obtain the desired nozzle static pressure

ratio. The jet static pressure at the nozzle exit plane was not measured directly, but was calculated using the given nozzle area ratio and the jet total pressure. A total temperature in the jet flow was not given experimentally, but was assumed to be equal to the freestream stagnation temperature (580.5°R).

6.2 Computational Details

Solutions were computed for the coflowing nozzle at the following five nozzle static pressure ratios: $P_j/P_\infty = 0.150, 0.251, 0.527, 1.03$ and 1.59 . These solutions were all performed on a CDC Cyber 175 digital computer located at Wright-Patterson AFB, Ohio. The average rate of data processing was 0.0015 second per grid point per iterative time increment. In this section further details of these computations will be discussed.

Grid Parameters

Important parameters of the computational grid including the number of grid points and axis length utilized in both the axial and radial directions are listed in Table 1 for each nozzle pressure ratio condition. The value of the axial field length includes a length increment of 0.4 upstream of the nozzle exit plane, with the exit plane at a value of $x/r_{jet} = 0.0$. A compact 45×45 point grid was used in the two most highly overexpanded cases ($P_j/P_\infty = 0.150, 0.251$). Twelve additional grid points were then added in the axial direction downstream of the original grid to form a 57×45 grid for the next case where $P_j/P_\infty = 0.527$ (Figure 25). This methodology gave a consistent cell length in the axial direction for each of these

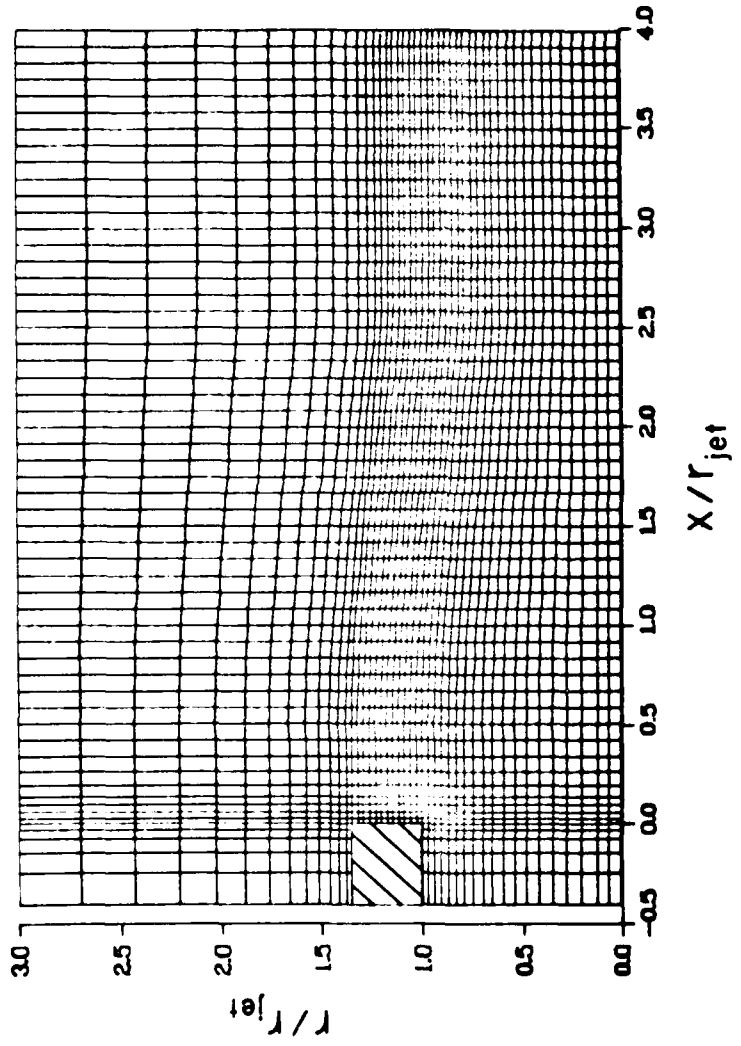


Figure 25. Adaptive Finite Difference Mesh, $P_j/P_\infty = 0.527$.

three cases in which both a regular shock reflection ($P_j/P_\infty = 0.527$) and Mach discs ($P_j/P_\infty = 0.251, 0.150$) should occur. The computational domain was then stretched using the 57×45 point grid to the degree necessary to cover the phenomena of interest for the two underexpanded cases.

Minimum grid spacing in both the axial and radial directions occurred adjacent to the nozzle walls, and was set at:

$$\Delta x/r_{jet} = \Delta r/r_{jet} = 0.030$$

The patched exponential stretching outlined in chapter 3 was then applied to form each grid initially for the various cases. The adaptive grid procedure was applied in the radial direction during the solution procedure as discussed in Chapter 3 and Appendix B to obtain the final grid geometry for each case.

Table 1. Computational Grid Parameters

P_j/P_∞	IL	JL	XLT/r _{jet}	YLT/r _{jet}
0.150	45	45	3.4	3.0
0.251	45	45	3.4	3.0
0.527	57	45	4.4	3.0
1.03	57	45	6.4	3.0
1.59	57	45	8.4	4.0

Coarse Grid Effects on Boundary Layer Resolution

The numerical solution of the Navier-Stokes equations can involve significant truncation errors in regions containing high velocity gradients such as within turbulent boundary layers when relatively coarse computational grids are employed. Errors in computed velocity gradients involved in shear force terms at the wall can result in erroneous values of the pressure gradient along the wall. The extent of

these errors can be realized by assuming the existence of a turbulent boundary layer possessing a velocity profile in the following form (36):

$$u^+ = y^+ \quad 0 < y^+ \leq 11 \quad (6.1a)$$

$$u^+ = 2.50 \ln(y^+) + 5.10 \quad 11 < y^+ < y_{BL \text{ edge}}^+ \quad (6.1b)$$

where

$$u^+ = u_s \sqrt{\tau_w} \quad \text{and} \quad y^+ = \sum_j \Delta y_w / c_j$$

Since the dominant term in the shear stress is the gradient $\frac{\partial u}{\partial y}$, a comparison of the value obtained using this profile can be made with that obtained using the numerical algorithm. MacCormack's algorithm computes this gradient using a first order finite difference in the direction of the sweep for the predictor step. At the wall this gradient is computed as:

$$\left. \frac{\partial u}{\partial y} \right|_w = u_{i,jw+1} / \Delta y_w \quad (6.2)$$

where $jw+1$ is the first grid point above the wall, and Δy_w is the grid spacing adjacent to the wall. If a nominal Reynolds number of 1×10^6 based on body length is applied to the previous turbulent velocity profile, the ratio of actual wall velocity gradient given by the previous profile to that computed using equation 6-2 can be displayed as a function of the ratio of u velocity component at the first point above the wall to the freestream velocity as shown in Figure 26. For grid spacing substantially greater than the sublayer ($u_1/u_e \approx 0.475$), excessive error in the computed velocity gradient occurs. Since in the coflowing jet solutions the previously stated minimum grid spacing gives values of $(u_1/u_e)_{in} = 0.72$ and $(u_1/u_e)_{jet} = 0.90$, a correction is needed. This is accomplished by applying the value of C_f given by a

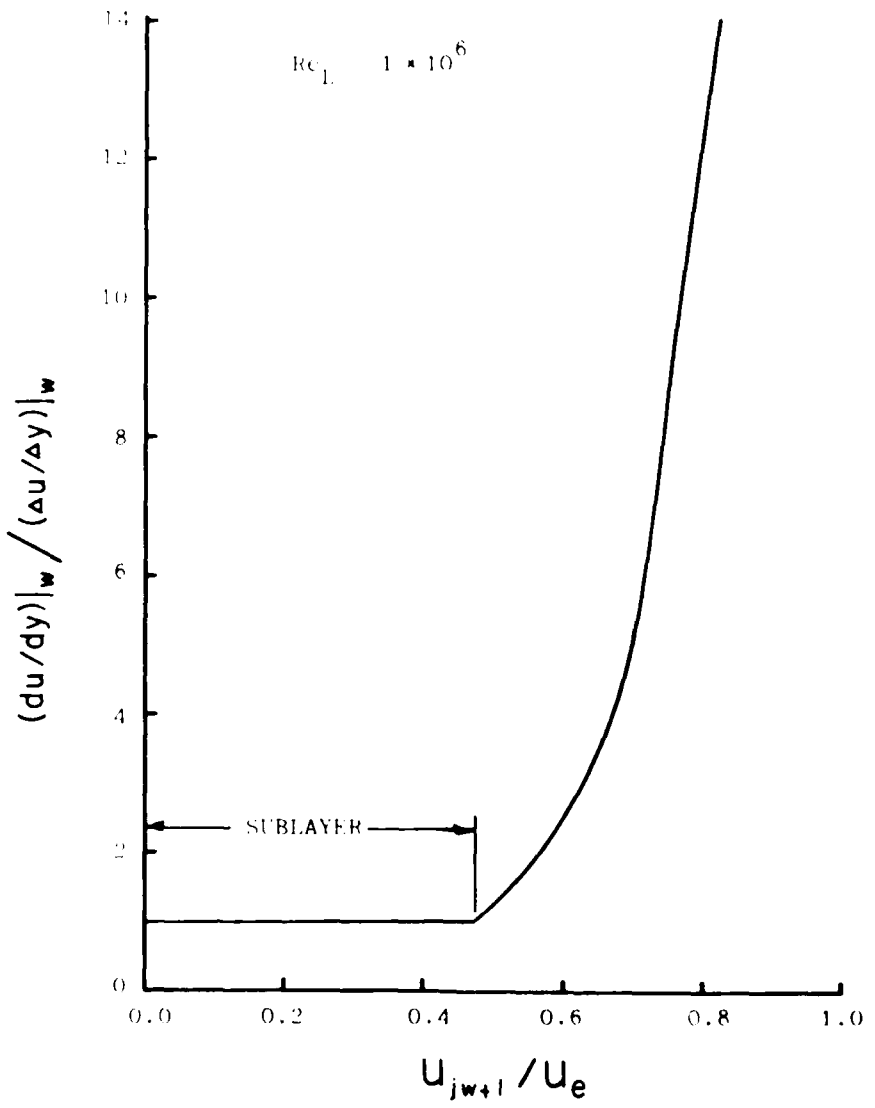


Figure 36. Error in Computed Velocity Gradient v: Grid Coarseness for a Turbulent Boundary Layer.

a boundary layer analysis at the inflow boundary along the nozzle wall when $j = j_w$, instead of using the standard differencing procedure in the algorithm. This procedure has resulted in smooth pressure profiles near the inflow boundary instead of slight pressure jumps previously observed in coarse mesh cases. This concept is analogous to the wall functions described by Launder and Spalding (37) and employed by Peery and Forester (38).

External Flow Parameters

Values for the external flow variables were input numerically by applying the experimental values of M_∞ , P_{∞} , T_{∞} , and the boundary layer profiles generated for use on the inflow boundary. A value for the turbulent skin friction coefficient of $C_f = 0.00286$ was obtained from the boundary layer input profiles and was applied on the external nozzle wall as discussed in the last section. A wall temperature of $551^\circ R$ was calculated using the analysis in Appendix A. The wall temperature was given a constant value for all five cases since the analysis showed that this temperature should not vary more than one degree over the range of simulated flow conditions.

Jet Flow Parameters

The numerical jet field of flow was determined by applying the experimental values of the jet Mach number and total temperature given in the previous section along with the values of the jet total pressure and skin friction coefficient listed in Table 2. Since the nozzle wall temperature was considered to be constant, the value for the internal nozzle wall was also set at $551^\circ R$. As shown in the table, the state of the jet boundary layer in all of the cases except the lowest nozzle pressure ratio condition ($P_j/P_\infty = 0.150$)

was considered to be turbulent at the nozzle exit plane. Since the case where $P_j/P_\infty = 0.251$ possessed a Reynolds number below the previously set transition point, a solution using a laminar jet boundary layer was also obtained. At this pressure condition, both the laminar and turbulent jet boundary layers gave nearly identical values for the nozzle base pressure and normal shock position. However, the laminar case exhibited a mild shear layer oscillation for the duration of the solution procedure. For this reason the results of the turbulent case are presented. It is interesting to note that no mixing layer oscillations were observed in the other laminar jet condition ($P_j/P_\infty = 0.150$).

Table 2. Computational Jet Flow Parameters

P_j/P_∞	P_{jet}^0 (psf)	$Re_j \times 10^{-5}$	Bound. Layer Character	$C_f \times 10^3$
0.150	1636.	1.61	Laminar	1.60
0.251	2738.	2.70	Turbulent	3.39
0.527	5747.	5.67	Turbulent	2.84
1.030	11230.	11.08	Turbulent	2.50
1.540	17340.	17.11	Turbulent	2.30

Boundary Condition Application

The specific numerical boundary conditions given in chapter four were applied to the computational domain in order to achieve solutions for the following nozzle. No significant problems were encountered with the application of the upstream boundaries, the upper boundary, or the nozzle wall boundaries. Difficulties were encountered with both the downstream boundary and the centerline boundary when a

AD-A100 817 AIR FORCE INST OF TECH WRIGHT-PATTERSON AFB OH SCHOOL--ETC F/G 20/4
NAVIER-STOKES SOLUTIONS FOR A SUPERSONIC COFLOWING AXISYMETRIC --ETC(U)
APR 81 G A HASEN
UNCLASSIFIED AFIT/OS/AA/81-2

2 OF 2
A1
A2
A3
A4

HL

END
DATE
FILED
7-81
DTIC

significant portion of the flow along each boundary was subsonic in nature. This condition only occurred for the highly overexpanded case ($P_j/P_\infty = 0.150$), where a substantial embedded subsonic region exists downstream of the Mach disc shock structure.

The quadratic extrapolation given by equation 4-17 produced very reasonable results for those cases where the outflow was either entirely supersonic, or only subsonic at a very few points in the nozzle wake. For the case where a substantial area of subsonic flow existed behind a Mach disc structure and extended to the downstream boundary, numerical divergence occurred when equation 4-17 was applied. A second order zero gradient condition was then applied in regions of subsonic flow along this boundary. Application of this condition did not produce numerical divergence, but did give unrealistic pressure jumps at this boundary. A first order zero gradient condition given in equation 4-18 was then successfully applied to subsonic regions on this boundary with reasonable results.

An almost identical situation occurred along the centerline boundary for subsonic regions containing fairly strong radial flow gradients close to the centerline. Both the extrapolation condition given by equation 4-21 and a second order zero gradient condition produced unrealistic radial oscillations in the numerical solution (called "wiggles") within these regions of subsonic flow. The application of a first order zero gradient condition given by equation 4-22 helped reduce these oscillations to achieve a reasonable solution.

Two solutions were also computed where first the downstream

boundary, and subsequently, the upper boundary were repositioned greater distances from the nozzle as discussed in Appendix E. No changes were detected in either the shock structure or the nozzle base pressure coefficient. These test cases validate the effectiveness of these boundary conditions at the positions utilized in the actual nozzle solutions.

Convergence

As stated in chapter 3, the numerical solutions were either initially started using only the boundary layer profiles across the computational domain, or restarted from a previous solution by applying new input profiles at the jet inflow boundary. Solution times based upon the convergence criteria discussed in chapter three varied significantly for the two methods of initial startup. Solution times on the Cyber 175 using only the boundary layer profiles to form the initial conditions were approximately 3.0 hours for the 45 x 45 point mesh and 3.8 hours for the 57 x 45 point mesh. Solution times for cases restarted from previous solutions were approximately 1.7 hours for the 45 x 45 mesh and 2.1 hours for the 57 x 45 mesh. The large difference in these solution times is mainly attributed to the length of time required for the subsonic recirculation region in the near wake to form and achieve a steady state condition.

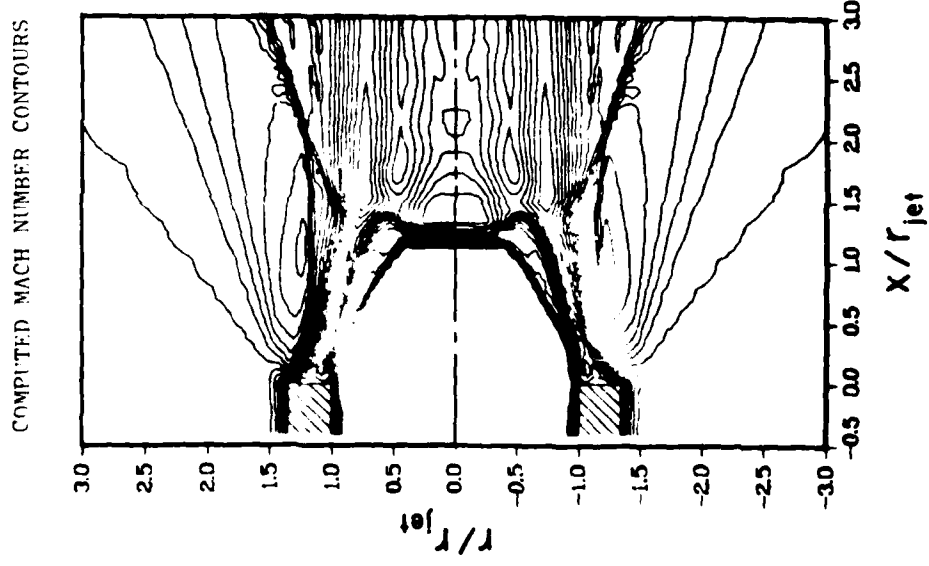
6.3 Comparison with Experimental Data

Comparisons between the numerical solutions and the experimental data can be made both qualitatively and quantitatively. Figures 27 through 31 give a good visual comparison between the numerical solutions

depicted as Mach number contours and the experimental schlieren photographs. In these figures the computed solutions above the centerline were reflected to give a total nozzle flowfield to compare with the schlieren photographs. All features typical of afterbody types of flows such as the shock structure internal to the jet core flow, external recompression shocks, and shear layer development are readily discernible and in very good agreement with the experimental data.

As shown by the previous figures, the pressure condition at which the jet flow shock structure transitions from a regular reflection on the centerline to the Mach disc formation lies between the two cases where $P_j/P_\infty = 0.527$ and $P_j/P_\infty = 0.251$. Although the shock structure near the centerline appears similar in the computational solutions for these two cases, an enlargement of this region as shown in Figure 32 reveals several differences. The shock strength (related to the Mach number jump across the shock) is much greater in both of the strong Mach disc cases ($P_j/P_\infty = 0.150$ and 0.251) than in the regularly reflected case ($P_j/P_\infty = 0.527$). The sonic lines in this region are displayed as dashed lines in Figure 32 in order to easily identify regions of subsonic flow. Both Mach disc cases contain areas of subsonic flow downstream of the shock along the centerline, whereas the minimum Mach number behind the regularly reflected shock is approximately equal to 1.65.

A check was made on the solution to the highly overexpanded case ($P_j/P_\infty = 0.150$) to determine if the numerical solution correctly simulated the flow conditions across the strong normal shock in the



SCHLTEREN PHOTOGRAPH

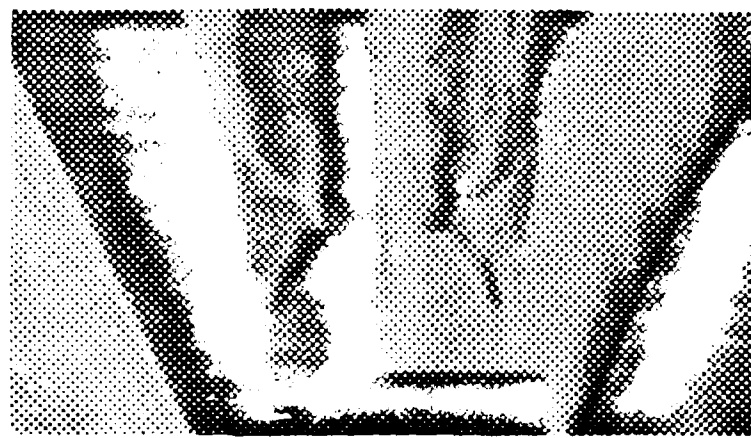
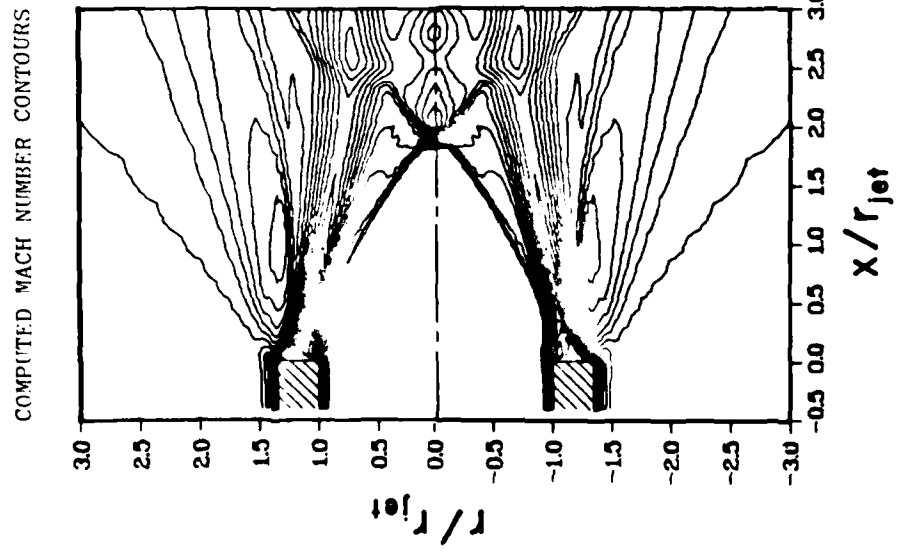


Figure 27. Axisymmetric Coflowing Nozzle Solution, $P_j/P_\infty = 0.150$.



SCHLIFEREN PHOTOGRAPH

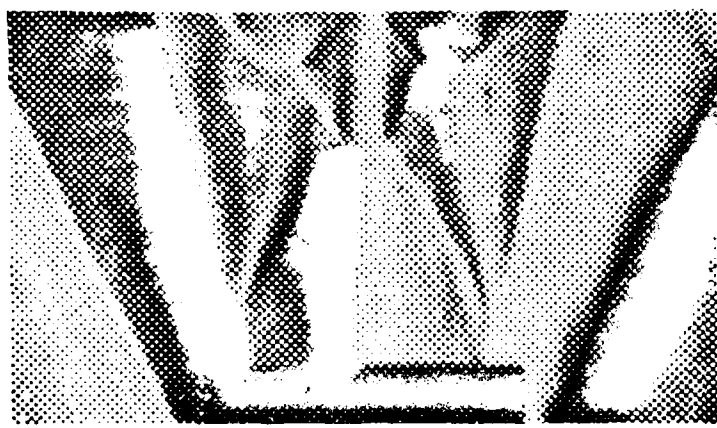
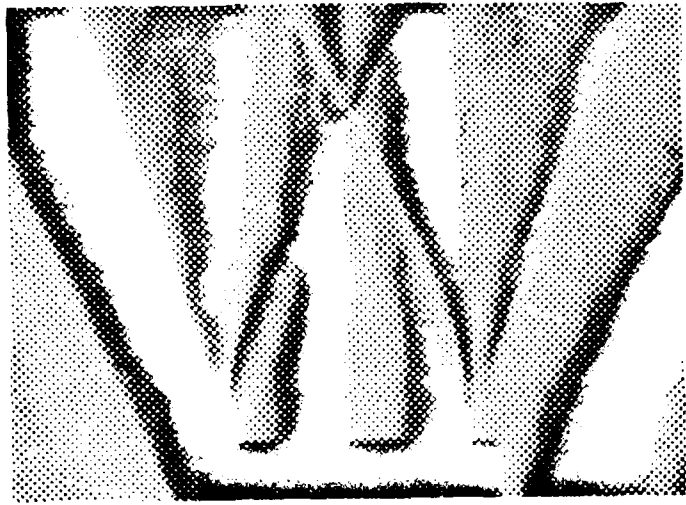


Figure 28. Axisymmetric Coflowing Nozzle Solution, $P_j/P_\infty = 0.251$.

SCHLIETEREN PHOTOGRAPH



COMPUTED MACH NUMBER CONTOURS

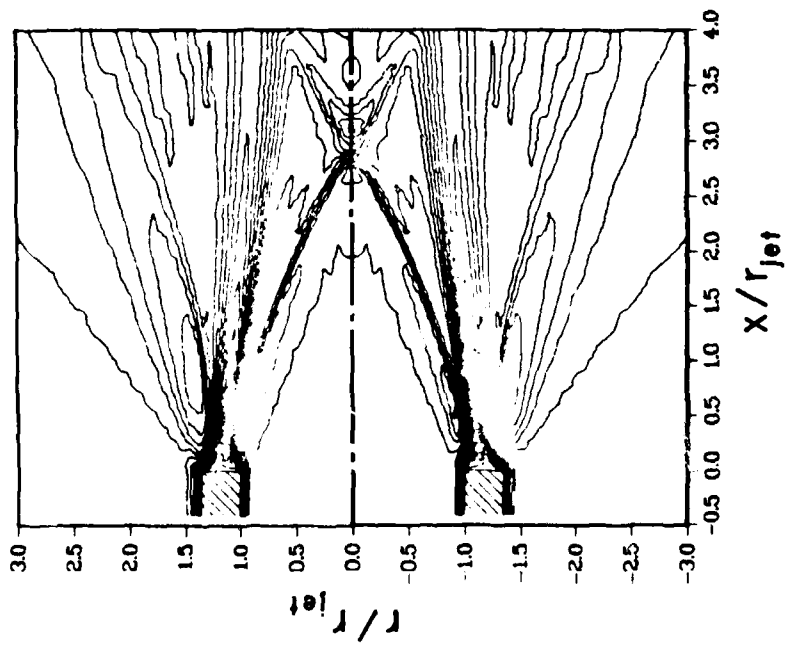


Figure 29. Axisymmetric Coflowing Nozzle Solution, $P_j/P_\infty = 0.527$.

SCHLIEREN PHOTOGRAPH



COMPUTED MACH NUMBER CONTOURS

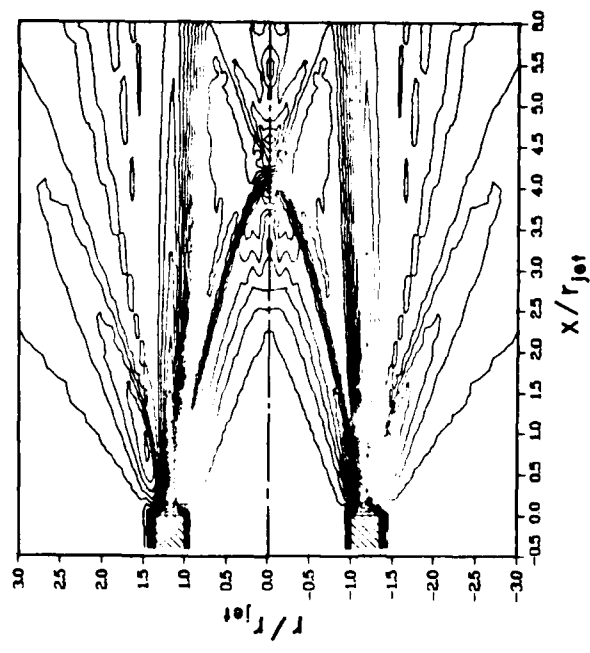
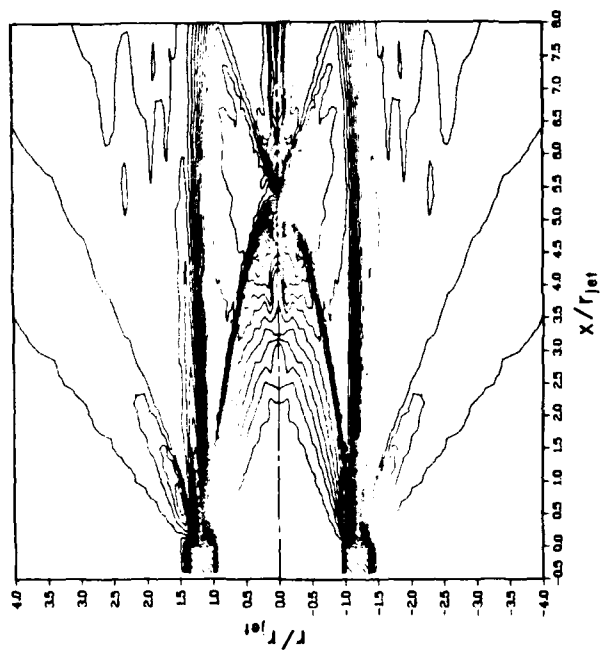


Figure 30. Axisymmetric Coflowing Nozzle Solution, $P_j/P_\infty = 1.03$.

COMPUTED MACH NUMBER CONTOURS



SCHLIFFEN PHOTOGRAPH

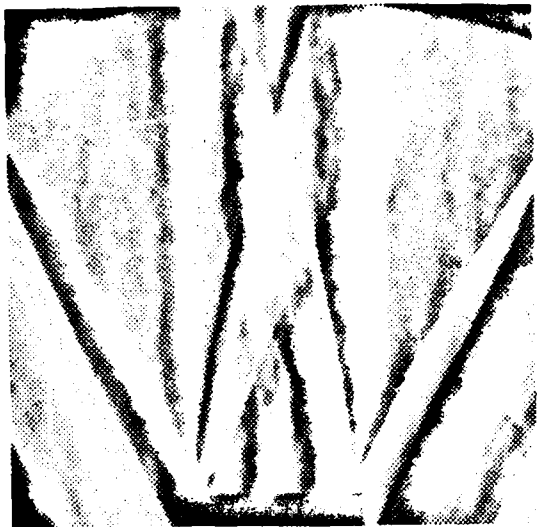


Figure 31. Axisymmetric Coflowing Nozzle Solution, $P_j/P_\infty = 1.59$.

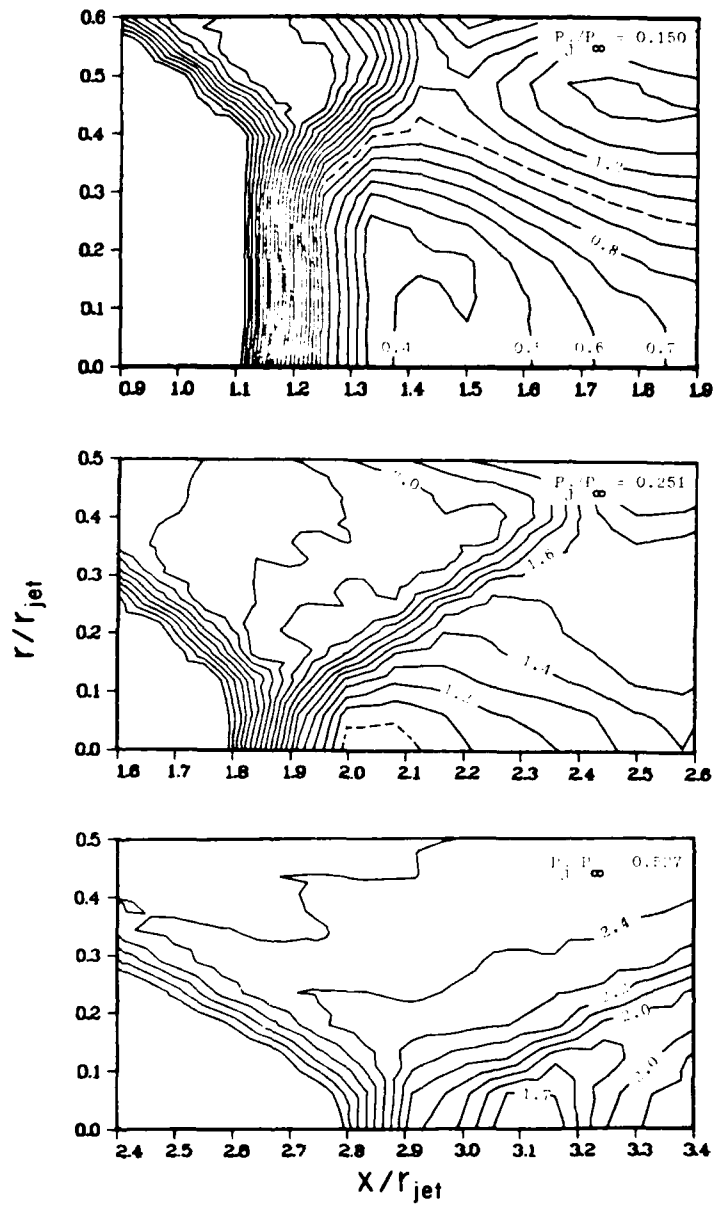


Figure 32. Computed Mach Number Contours in the Region Near the Shock Reflection at the Centerline.

region near the centerline. Since the v velocity components are very small near the centerline, a one-dimensional analysis based on the Rankine-Hugoniot relations across normal shocks can be applied. As shown in Table 3, the computational solution was within 2% of the exact one-dimensional analysis.

Table 3. Comparison Between a 1-D Analysis and the Computational Solution Across the Mach Disc for $P_j/P_\infty = 0.150$.

	M_j	M_2	P_2/P_j	ρ_2/ρ_j	T_2/T_j
Exact (1-D)	3.00	.475	10.33	3.857	2.679
Computational	3.00	.442	10.52	3.906	2.695
% Error	----	1.1	1.8	1.3	0.6

Several other phenomena associated with afterbody flows are evident in Figure 33, which displays computed velocity profiles at given axial stations for the large Mach disc case. The separated "deadwater zone" of recirculating flow is readily apparent in the near wake region, as is the development of the near wake to a far wake velocity profile. The existence of the strong Mach disc near the centerline is very evident, and the flow in the subsonic core region behind the shock accelerates in the correct manner to a slightly supersonic condition at the outflow boundary.

A closer look at the near wake region is shown in Figure 34 for two of the computational cases. This figure illustrates the change in the shape of the "deadwater region" from a predominantly symmetric nature at $P_j/P_\infty = 1.03$ to one with an asymmetric nature at $P_j/P_\infty = 0.150$. In this figure the dashed lines denote the dividing streamline and the streamlines through the stagnation point in the near wake flow for each case. As shown in Figure 35, the dividing streamline

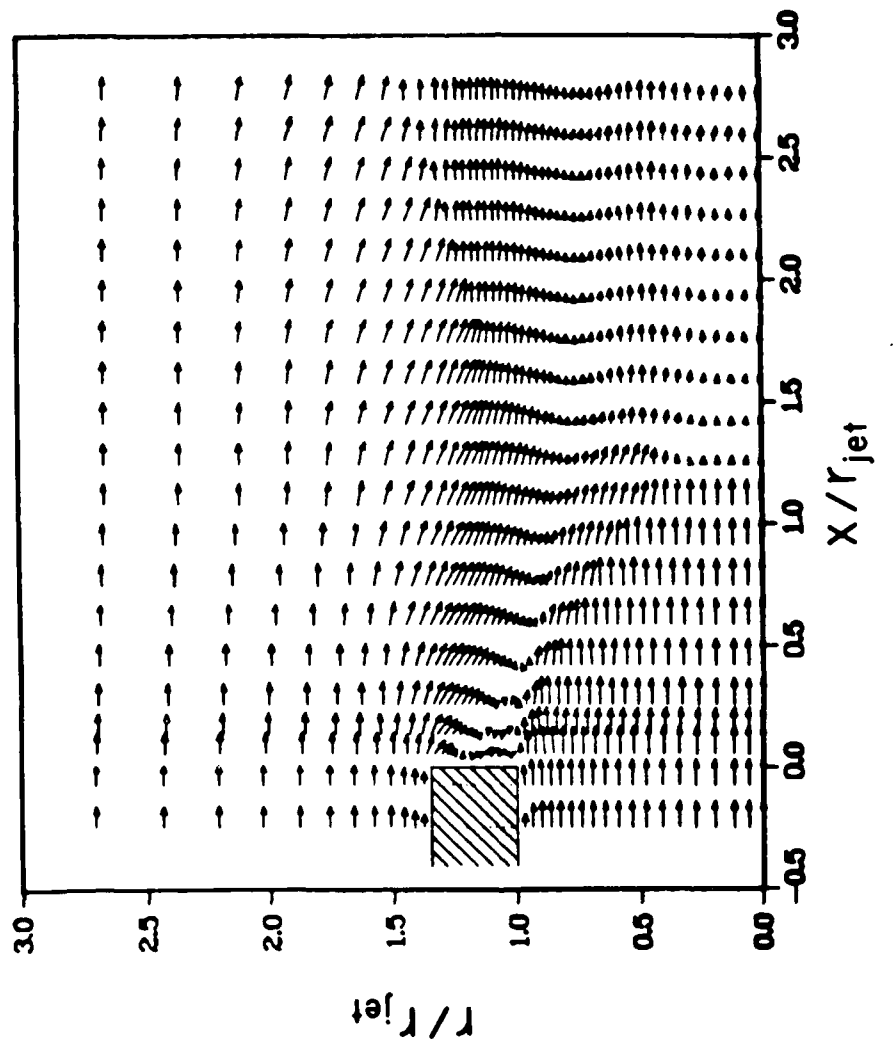


Figure 33. Computed Velocity Profiles, $P_j/P_\infty = 0.150$.

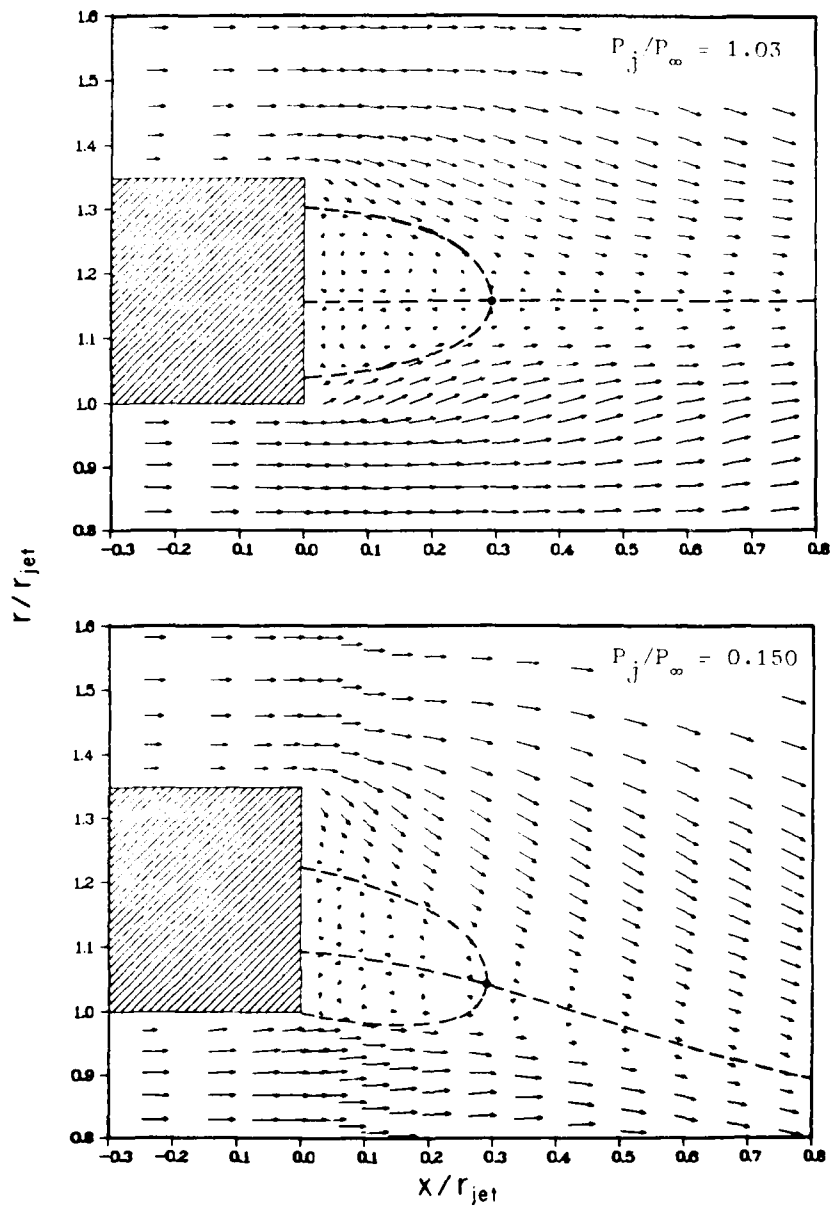


Figure 34. Computed Velocity Fields in the Near Wake Region of the Coflowing Nozzle.

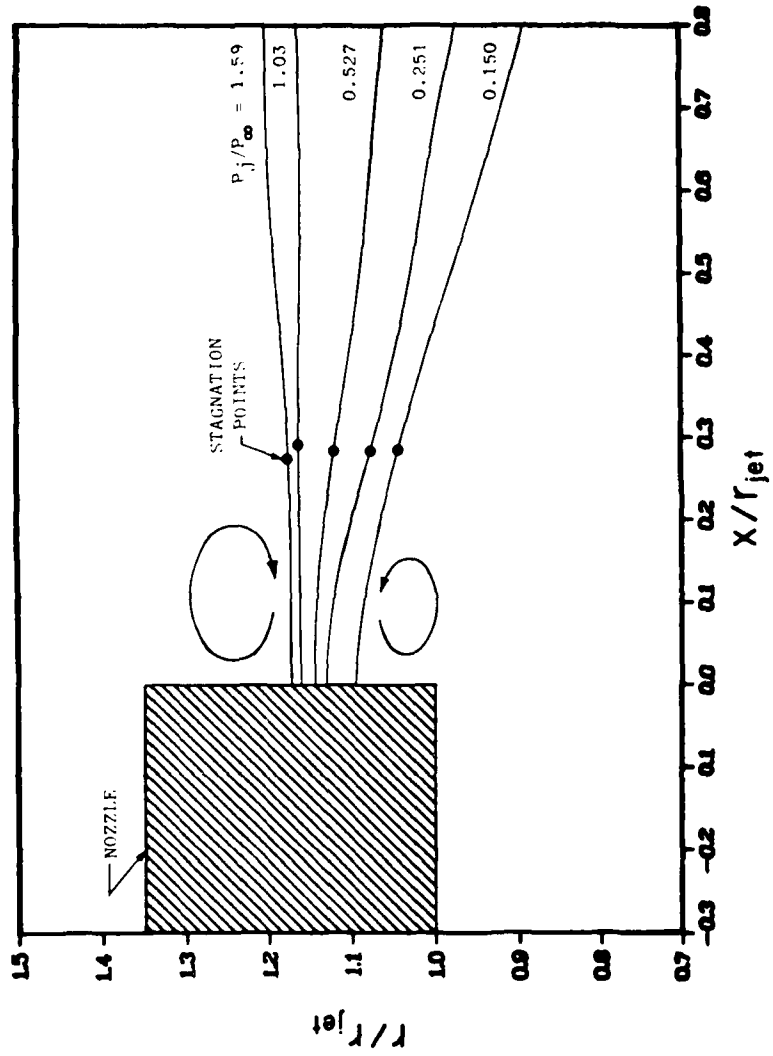


Figure 35. Position of the Dividing Streamline in the Computational Conflicting Nozzle Solutions.

moves toward the inner wall of the nozzle as the total pressure in the jet is decreased. Although the stagnation point in the near wake region moves radially as the jet stagnation pressure is changed, it remains in a relatively constant position axially for the cases computed.

Quantitative comparisons between the experimental data and the computed solutions are based primarily on two parameters: the axial distance along the centerline from the nozzle exit plane to the point of reflection of the incident shock wave at the line of symmetry, and the value of the nozzle base pressure coefficient. This reflection length, along with the type of shock reflection (either strong or weak), is a good indication that the inviscid flow features in the jet core caused by viscous-inviscid interaction are properly simulated. These computed shock reflection lengths are obtained by examining the axial variation in Mach number along the centerline as shown in Figure 38 for a typical case. As shown in this figure, the shock reflection is diffused over three cell lengths, with the computational value of the reflection length taken as being at the midpoint of these three cells. Comparisons between the experimental and computational values of these reflection lengths are shown in Figure 37 and Table 4. Excellent agreement was obtained, with the computational results being within 2% of the experimental data.

An additional quantitative comparison was also made of the computed and observed Mach disc radii for the two cases at which the Mach disc was observed. This comparison is listed in Table 5. The computed Mach radius was taken as the radial height of the

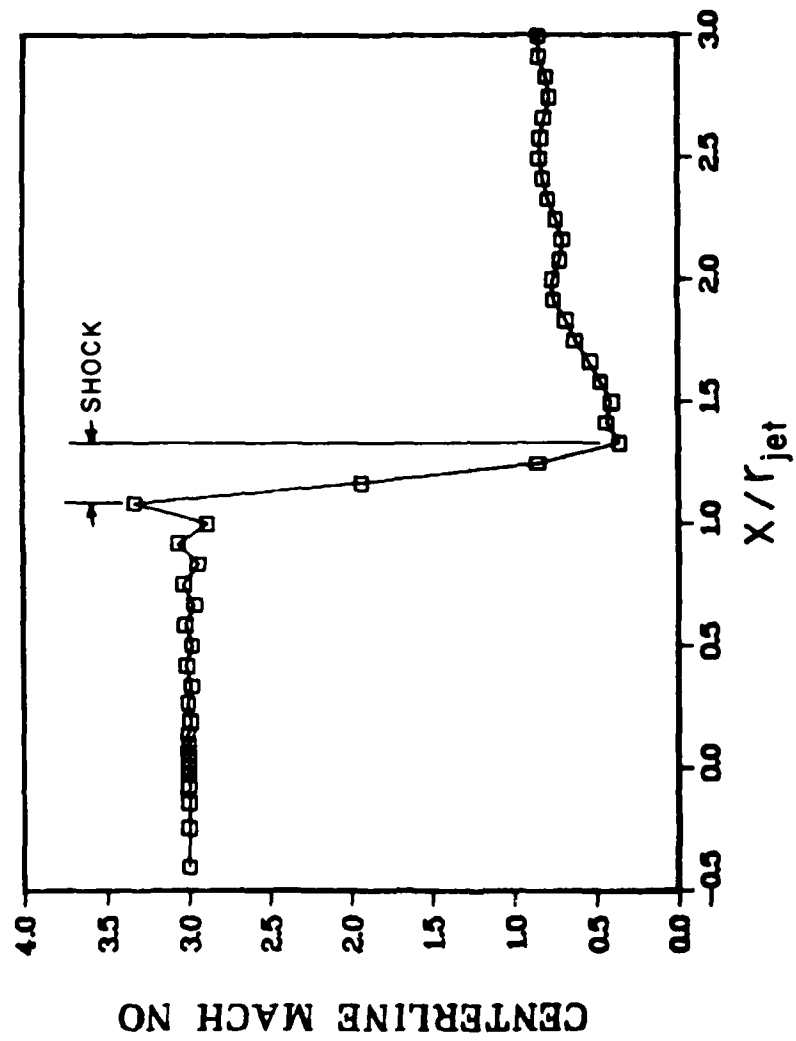


Figure 36. Axial Variation in Computed Centerline Mach Number, $P_j/P_\infty = 0.150$.

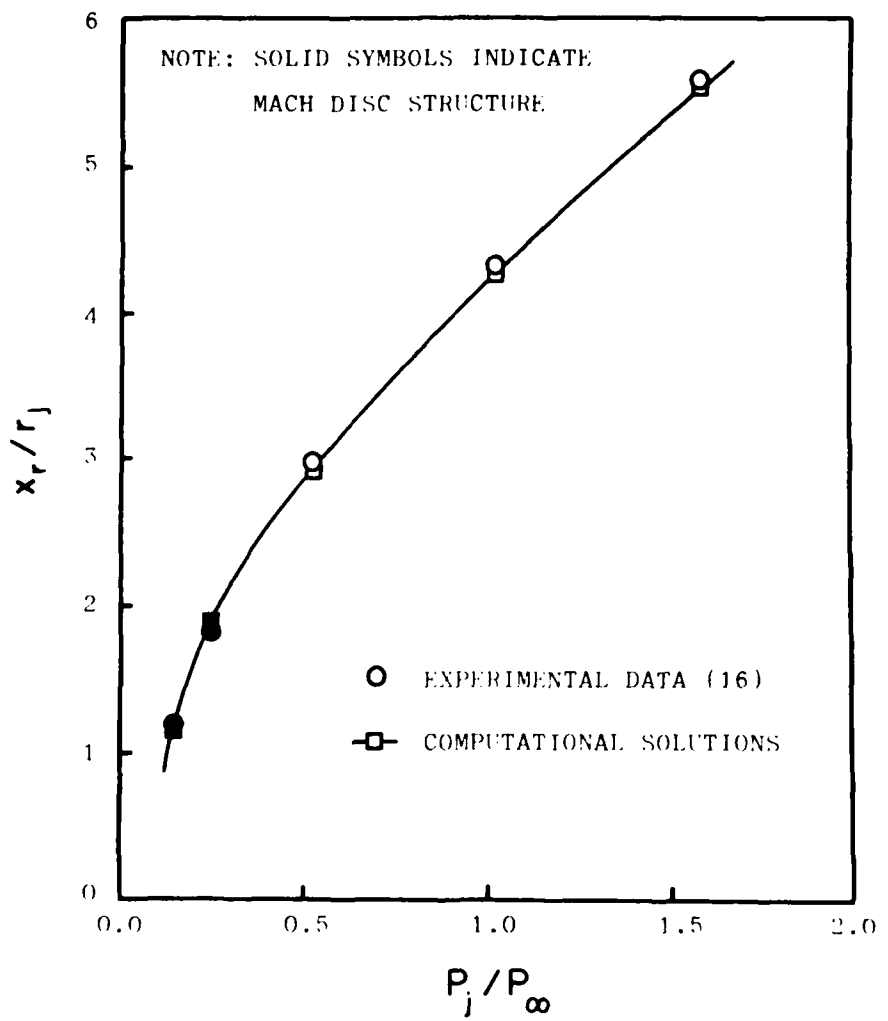


Figure 37. Shock Reflection Lengths Along the Nozzle Centerline vs Nozzle Pressure Ratio.

sonic line immediately behind the strong shock wave. Very good agreement was obtained for the highly overexpanded case ($P_j/P_\infty = 0.150$) in which a fairly large Mach disc occurs. Poorer agreement was obtained for the case that was much nearer to transition to a regular shock reflection, with a very small Mach disc radius ($r_m/r_{jet} = 0.17$). The first cell height adjacent to the centerline in the computational solution possessed a value of $r/r_{jet} = 0.06$, so that numerical truncation error played a large part in the discrepancy in Mach stem radius at this particular condition.

Table 4. Comparison of Shock Reflection Lengths

P_j/P_∞	Experimental $x/r_{jet} (+0.05)$	Computational $x/r_{jet} (+0.04)$	% Error
0.150	1.19	1.17	-0.3
0.251	1.88	1.91	+0.5
0.527	2.98	2.91	-1.2
1.030	4.37	4.26	-1.9
1.590	5.64	5.53	-2.0

Table 5. Comparison of Mach Disc Radii

P_j/P_∞	Experimental $r_m/r_{jet} (+0.05)$	Computational $r_m/r_{jet} (+0.04)$	% Error
0.150	0.45	0.44	-2.2
0.251	0.17	0.06	-24.

Table 6. Comparison of Base Pressure Coefficients

P_j/P_∞	Experimental* Γ_B (+0.003)	Computational Γ_B (+0.002)	% Error
0.150	-0.240	-0.310	-25.0
0.251	-0.280	-0.299	- 6.8
0.527	-0.265	-0.276	- 3.9
1.030	-0.237	-0.245	- 2.9
1.590	-0.226	-0.219	+ 2.5

*interpolated from existing values

Comparisons between the experimental and computational values of nozzle base pressure coefficient are shown in Figure 6.14 and Table 6. Since the experimental data points for the base pressure coefficients were not obtained at the same pressure ratio values as the schlieren data, experimental values for the base pressure coefficients in Table 6 were interpolated from the available data points at the five given nozzle pressure ratios. Values of the computed nozzle base pressure were in good agreement with the experimental data (3-7% error), with the exception of the highly overexpanded case at which $P_j/P_\infty = 0.150$. Figure 38 shows that as the pressure ratio of the nozzle is lowered, the decreasing trend in nozzle base pressure reverses at a value of approximately $P_j/P_\infty = 0.18$ and sharply increases as the pressure ratio is further reduced. This sudden reversal in behavior is apparently due to flow separation in the divergent portion of the nozzle which prevents the jet flow from expanding fully to its assumed Mach 3.0 state. For pressure ratio values less than $P_j/P_\infty = 0.135$, deterioration of the Mach disc formation to a regular shock reflection occurs as shown in Figure 39. This may

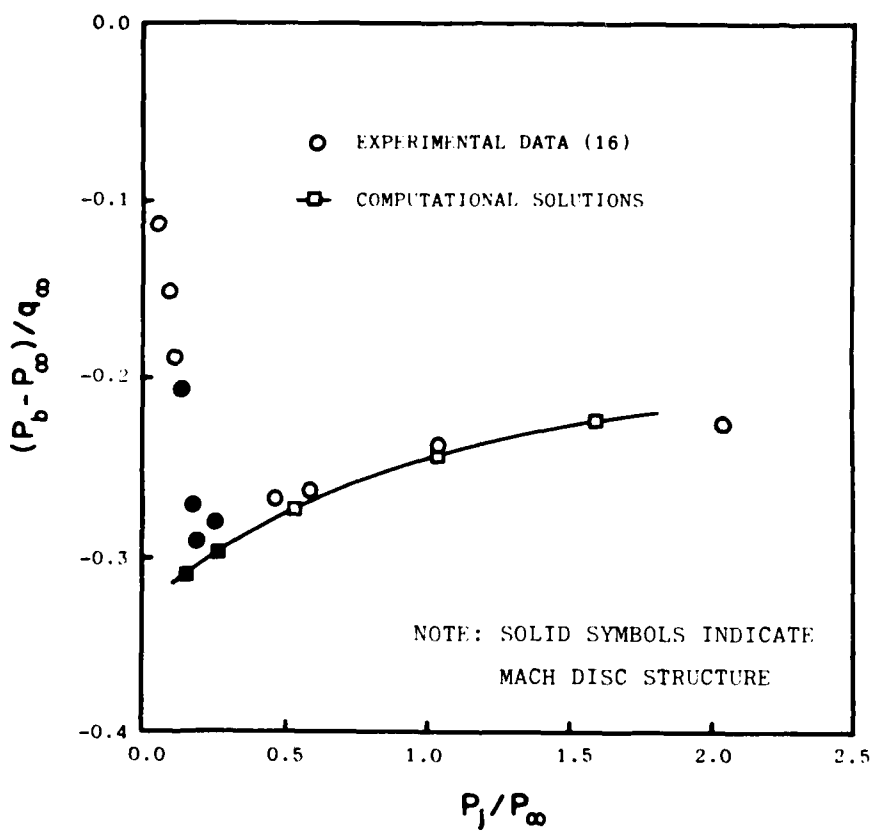


Figure 38. Base Pressure Coefficient vs Nozzle Pressure Ratio.



$$P_j/P_\infty = 0.124$$



$$P_j/P_\infty = 0.132$$



$$P_j/P_\infty = 0.135$$



$$P_j/P_\infty = 0.150$$

Figure 39. Schlieren Photographs (16) Showing the Eventual Deterioration of the Mach Disc with Decreasing Nozzle Pressure Ratio.

indicate that for values less than $P_j/P_\infty = 0.135$, either the jet Mach number is less than 1.48 and thus cannot support a Mach disc structure (8), or the increase in nozzle static pressure due to the reduced expansion cannot produce the deflection angle in the jet flow needed for a Mach disc to occur. A non-separated condition was assumed by the experimental investigators, since their value of P_j was determined using the jet total pressure and the final area ratio of the nozzle. Likewise, the computational solutions assumed non-separated Mach 3 flow just upstream of the nozzle exit plane. If some separation did occur and the nozzle flow did not fully expand to a Mach 3 condition, a substantial difference in base pressure could result.

This hypothesis of separation in the nozzle was partially confirmed by computationally solving a case where the jet total pressure corresponded to the attached case ($P_j/P_\infty = 0.150$), but with jet input profiles corresponding to an isentropic expansion of the jet flow to a Mach number of only 2.60 as detailed in Appendix E. A correct strong shock structure was obtained computationally, and the value of the base pressure coefficient increased to a value of -0.265. This was in much better agreement with the experimental data at this condition. A more accurate simulation of this pressure ratio condition would require extending the computational mesh back to the nozzle throat. Separation in the nozzle could then occur in a direct manner in the numerical solution. Since this would require extensive grid revisions as well as additional computer resources, it was considered to be beyond the scope of this investigation.

CHAPTER VII

CONCLUSIONS AND RECOMMENDATIONS

A numerical method of obtaining solutions to the Navier-Stokes equations for supersonic coflowing axisymmetric nozzles has been developed from a selection of appropriate techniques. Based on the numerical analysis and computational results obtained through this study, the following conclusions are drawn:

1. The numerical solution of the Navier-Stokes equations applied to supersonic coflowing nozzles successfully reproduced all of the essential flow features including boundary layers, corner expansions, recompression shocks, the recirculation region adjacent to the nozzle base wall and the evolution of the near wake to a flow with far wake behavior.
2. The numerical method achieved a correct transition from regularly reflected shock waves at the line of symmetry in the jet core flow to a strong Mach disc formation at the appropriate static pressure ratio condition of the nozzle. The subsonic embedded region immediately behind the Mach disc formation was simulated in a correct manner.
3. The application of an adaptive grid scheme in the wake region of the nozzle annulus successfully positioned the fine mesh region of the computational grid in the wake region which normally contains severe flow gradients. This allowed the accurate simulation of this high flow gradient region while conserving numerical resources.

4. The nozzle base pressure was heavily dependent on the eddy viscosity model applied in the region of the near wake. Once the model was tuned for the neutrally expanded case ($P_j/P_\infty = 1.03$), good agreement was obtained computationally for all cases where the flow obeyed the assumption of remaining attached in the divergent portion of the nozzle.
5. Boundary conditions must be carefully formulated and applied in order to prevent physically unrealistic results or numerical divergence of the solution. Both the centerline and downstream boundaries were sensitive where regions of subsonic flow occurred over a substantial portion of the boundary. Both the quadratic extrapolation used in regions of supersonic flow and a second order, zero gradient condition caused either divergence or unrealistic conditions at the boundary when applied to regions of subsonic flow. A first order zero gradient condition was used successfully in these regions of subsonic flow and found to be superior. Generalizations about the success of this first order boundary condition cannot be made, since the degree of success achieved is dependent on the specific numerical algorithm applied to the problem.
6. The final steady state solutions were found to be insensitive to the initial conditions applied over the computational domain. However, the time to converge to the final solution was highly dependent on the application of specific initial conditions. In particular, the region of subsonic recirculation in the near wake was the last region in the solution domain to converge. Solutions started using only the boundary layer profiles across

the domain required three hours to converge on a Cyber 175 (45 x 45 point mesh), whereas cases started from a previous different jet total pressure condition but with an established near wake structure required only 1.7 hours to converge (45 x 45 mesh).

7. To the author's knowledge, this is the first full Navier-Stokes solution that has accurately simulated the viscous-inviscid interactions present in a supersonic coflowing nozzle at off-design conditions where the strong Mach disc shock structure is present. Mikhail (8) previously was unsuccessful in reproducing the Mach disc reflection in a full Navier-Stokes solution due to the probable improper placement of the jet inflow boundary condition, which did not allow the jet plume to expand to the degree necessary to generate a Mach disc reflection.

Based on the numerical analysis and results obtained through this study, the following recommendations are made:

1. The present scalar computer code developed during the course of this investigation should be vectorized for use on the new generation of "supercomputers" such as the CRAY-1 or the Cyber 203. Although present solution times are on the order of two to four hours when run on a Cyber 175 computer, a fully vectorized version of the present computer code can be expected to converge within five minutes on a CRAY-1 computer (39). This will allow computation of more complex nozzle geometries and better resolution in the boundary layers through the application of finer mesh, while holding costs to a reasonable level.
2. The present numerical solver should be modified to include the

effects of a calorically imperfect gas with variable specific heat and thermal conductivity. This modification would allow accurate simulation of the temperature dependent effects for hot exhaust nozzles with gas temperatures less than 5000°R (19). Only minor revisions to the existing computer code would be required in order to include these temperature effects.

3. After the implementation of the two previous recommendations, it would be desirable to incorporate the effects of species mixing into the numerical solver. Many practical cases of interest involve a jet exhaust gas with a different species than that of the external stream. This modification would require a significant code revision, since the addition of the equation of mass diffusion would be required, as would the correct modeling of appropriate mass diffusion coefficients.

BIBLIOGRAPHY

1. Grossman, B., and Melnik, R. E., "The Numerical Computation of the Transonic Flow Over Afterbodies Including the Effect of Jet Plume and Viscous Interactions," AIAA Paper 75-62, Pasadena, California, Jan. 1975.
2. Cosner, R. R., and Bower, W. W., "A Patched Solution of the Transonic Flowfields about an Axisymmetric Boattail," AIAA Paper 77-227, Los Angeles, California, Jan. 1977.
3. Pergament, H. S., and Dash, S. M., and Wilmoth, R. G., "Prediction of Nearfield Jet Entrainment by an Interactive Mixing/Afterburning Model," AIAA Paper 78-1189, Seattle, Washington, July 1978.
4. Yaeger, L., "Transonic Flow Over Afterbodies Including the Effects of Jet-Plume and Viscous Interactions with Separation," AIAA Paper 77-228, Los Angeles, California, Jan. 1977.
5. Holst, T., "Numerical Solution of Axisymmetric Boattail Fields with Plume Simulators," AIAA Paper 77-224, Los Angeles, California, Jan. 1977.
6. Mikhail, A. G., "Numerical Solution of a Supersonic Nozzle Afterbody Flow with Jet Exhaust," AFFDL-TR-79-3078, June 1979.
7. Shapiro, A. H., The Dynamics and Thermodynamics of Compressible Fluid Flow, The Roland Press Co., 1954.
8. Henderson, L. F., and Lozzi, A., "Experiments on Transition of Mach Reflexion", Journal of Fluid Mechanics, Vol. 68, Part 1, 1975, pp. 139-155.
9. Adamson, T. C., and Nicholls, J. A., "On the Structure of Jets from Highly Underexpanded Nozzles into Still Air," Journal of the Aerospace Sciences, Jan. 1959, pp. 16-24.
10. Eastman, D. W., and Radtke, L. P., "Location of the Normal Shock Wave in the Exhaust Plume of a Jet," AIAA Journal, Vol. 1, No. 4, April 1963.
11. Abbet, M. A., "Mach Disc in Underexpanded Exhaust Plumes," AIAA Journal, Vol. 9, No. 3, March 1971, pp. 512-514.
12. Chang, I. S., "Mach Reflection, Mach Disc, and the Associated Nozzle Free Jet Flows," PhD Thesis, 1973, Dept. of Mechanical and Industrial Engineering, University of Illinois at Urbana-Champaign, Urbana, Illinois.
13. Jofre, R. J., "The Mach Disc in Axisymmetric Rocket Plumes," PhD dissertation, Louisiana State University, May 1971.

14. Sinha, R., Zakkay, V., and Erdos, J., "Flowfield Analysis of Plumes of Two-Dimensional Underexpanded Jets by a Time-Dependent Method," AIAA Journal, Vol. 9, No. 12, Dec. 1971, pp. 2362-2570.
15. Hankey, W. H., "Viscous Analysis of a Slip Surface , AIAA Journal, Vol. 10, No. 10, October 1972, pp. 1363-1364.
16. Bromm, A. F., and O'Donnell, R. M., "Investigation at Supersonic Speeds of the Effect of Jet Mach Number and Divergence Angle of the Nozzle upon the Pressure of the Base Annulus of a Body of Revolution," NACA RM L54116, Dec. 1954.
17. Roache, P. J., Computational Fluid Dynamics, Hermosa Publishers, Albuquerque, New Mexico, 1972.
18. Chapman, D. R., "Computational Aerodynamics Development and Outlook", AIAA Journal, Vol. 17, No. 12, December 1979, pp. 1293-1313.
19. Ames Research Staff, 'Equations, Tables and Charts for Compressible Flow", NACA Report 1135, 1953.
20. Rubesin, M. W. and Rose, W. C., "The Turbulent Mean-Flow, Reynolds Stress, and Heat Flux Equations in Mass Averaged Dependent Variables," NASA TMX-62, 248, March 1973.
21. Hirt, C. W., Nichols, B. D. and Romero, N. C., "SOLA - A Numerical Solution Algorithm for Transient Fluid Flows", Report LA-5852, Los Alamos Scientific Laboratory, April 1975.
22. MacCormack, R. W., "Numerical Solution of the Interaction of a Shock Wave with a Laminar Boundary Layer", Proceedings of the Second International Conference on Numerical Methods in Fluid Dynamics, Univ. of California, Berkely, September 15-19, 1970.
23. MacCormack, R. W. and Baldwin, B. S., "A Numerical Method for Solving the Navier-Stokes Equations with Application to Shock-Boundary Layer Interactions", AIAA Paper 75-1, Pasadena, Calif., January 1975.
24. Black, Roie, "Parabolized Navier-Stokes Solver", to be published as an AFWAL Tech Memorandum.
25. Shang, J. S., Hankey, W. L., and Dwoyer, D. L., "Compressible Turbulent Boundary Layer Solutions Employing Eddy Viscosity Models", ARL Report #73-0041, March 1973.
26. Blake, Charles R., "Numerical Solution of the Compressible Boundary Layer Equations Over Axisymmetric Surfaces", AFIT Master's Thesis GA/MA/76D-4, 1976.

- 27. Schlichting, H., Boundary Layer Theory, McGraw-Hill Book Company, New York, 1968.
- 28. Harsha, P. T., "Free Turbulent Mixing: A Critical Evaluation of Theory and Experiment", AEDC-TR-71-36, February 1971.
- 29. Cebeci, T., Smith, A., and Mosinskis, G., "Calculation of Compressible Adiabatic Turbulent Boundary Layers", AIAA Journal, Vol. 8, No. 11, November 1970, pp 1974-1982.
- 30. Dash, S. M., Wilmouth, R. G., and Pergament, H. S., "Overlaid Viscous/Inviscid Model for the Prediction of Near Field Jet Entrainment", AIAA Journal, Vol. 17, No. 9, September 1979, pp 950-958.
- 31. Pergament, H. S., Dash, S. M., and Varma, A. K. "Evaluation of Turbulence Models for Rocket and Aircraft Plume Flowfield Predictions", ARAP Report No. 370-1, February 1979.
- 32. Baldwin, B. S. and Lomax, H., "Thin Layer Approximation and Algebraic Model for Separated Turbulent Flows", AIAA Paper 78-527, Huntsville, Alabama, January 1978.
- 33. Toyoda, J., and Hirayama, N., "Turbulent Near Wake of a Flat Plate (Part 2, Effects of Boundary Layer Profile and Compressibility)", Bulletin of the JSME, Vol. 18, No. 120, June 1975, pp 605-611.
- 34. Rom, J., Seginer, A., and Kronzon, J., "The Flow Field in the Turbulent Supersonic Near Wake Behind a Two-Dimensional Wedge Flat Plate Model", TAE Report No. 54, August 1966.
- 35. Rom, J., Seginer, A., and Kronzon, J., "The Velocity, Pressure and Temperature Distributions in the Turbulent Supersonic Near Wake Behind a Two Dimensional Wedge Flat Plate Model", TAE Report No. 80, September 1968.
- 36. Lin, C. C. (editor), Turbulent Flows and Heat Transfer, Volume 5, High Speed Aerodynamics and Jet Propulsion, Princeton University Press, 1959.
- 37. Launder, B. E., and Spaulding, D. B., "The Numerical Computation of Turbulent Flows", Computer Methods in Applied Mechanics and Engineering, Vol. 3, pp. 269-289, 1974.
- 38. Peery, K. M., and Forester, C. K., "Numerical Simulation of Multi-Stream Nozzle Flows", AIAA Paper 79-1549, AIAA 12th Fluid and Plasma Dynamics Conference, Williamsburg, Virginia, July 1979.

39. Shang, J. S., Buning, P. G., Hankey, W. L., and Wirth, M. C., "Performance of a Vectorized Three-Dimensional Navier-Stokes Code on the CRAY-1 Computer", AIAA Journal, Vol. 18, No. 9, September 1980, pp. 1073-1079.
40. Kays, W. M., Convective Heat and Mass Transfer, McGraw-Hill, Inc, 1966.

APPENDIX A

NOZZLE WALL TEMPERATURE CALCULATION

The nozzle wall boundary condition applied during the numerical solution procedure assumes a constant nozzle wall temperature within the computational domain. The relatively high thermal conductivity of the stainless steel nozzle makes this assumption valid. This wall temperature can be calculated by applying a heat flux balance across the freestream boundary layer, the nozzle wall, and the jet boundary layer as shown in Figure 40. Conduction of heat in the axial direction is neglected due to the low temperature gradients in this direction.

Since both the freestream and the jet flow are of a high-velocity nature, the unit heat flux for either stream can be written as (40):

$$\dot{q}_{w_i} = h_i (T_{aw_i} - T_w) \quad (A-1)$$

where h_i is the heat conductance of each flowstream. The adiabatic wall temperature, T_{aw_i} , is defined by the expression:

$$T_{aw_i} = T_i \left(1 + \sqrt[n]{\text{Fr}} \left(\frac{\gamma-1}{2}\right) M_i^2\right) \quad (A-2)$$

where n is 1/2 for laminar flow and 1/3 for turbulent flow. Equating the heat flow out of the control volume for a steady state process gives:

$$\sum_i \dot{q}_i = 0 \quad (A-3)$$

or

$$2\pi r_o^{j_0} \dot{q}_\infty + 2\pi r_j^{j_0} \dot{q}_j = 0 \quad (A-4)$$

where j_0 is either 0 or 1 for two-dimensional or axisymmetric flow, respectively.

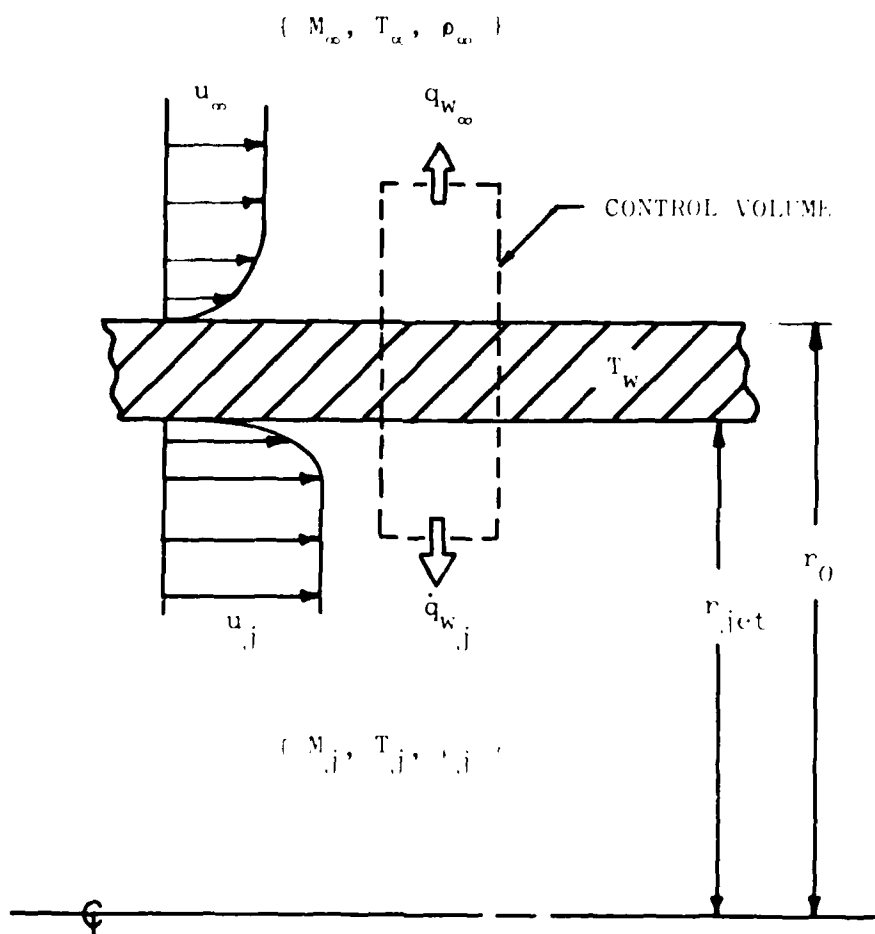


Figure 40. Heat Flux Balance Used to Determine the Nozzle Wall Temperature.

Applying equation A-1 to the values of the individual heat fluxes and solving for the wall temperature gives:

$$T_w = \frac{T_{aw_j} + (r_o/r_j)^{j^\circ} (h_\infty/h_j) T_{aw_\infty}}{[1 + (r_o/r_j)^{j^\circ} (h_\infty/h_j)]} \quad (A-5)$$

For flows involving a constant boundary layer edge velocity and a constant wall temperature, the conductances, h_i , can be defined by the following analytic expressions:

$$h_i = 0.332 C_p \rho_i u_i Re_{xi}^{-1/2} Pr^{-2/3} \quad (A-6)$$

for laminar flow, and

$$h_i = 0.0295 C_p \rho_i u_i Re_{xi}^{-1/5} Pr^{-2/5} \quad (A-7)$$

for turbulent flow (40). All of the quantities on the right-hand-side of equation A-5 are then known, and a value for the wall temperature can be calculated based on the states of the two flowfields adjacent to the nozzle wall.

APPENDIX B

ADAPTIVE FINITE DIFFERENCE MESH

It is desirable that the fine mesh region of the computational grid remain in the areas of relatively high velocity and temperature gradients as the solution progresses towards convergence. Hirt (21) has used a technique in the solution of free surface flows that allows the grid to adapt as the solution progresses. The following kinematic equation is applied in the region where the nozzle wake and shear layer develop:

$$\frac{\partial \mathbf{r}}{\partial t} = C_A (\mathbf{v} - \mathbf{u} \frac{\partial \mathbf{r}}{\partial \mathbf{x}}) \quad (B-1)$$

This equation ensures the condition that as the solution converges, the physical slope of the constant η finite difference cell boundaries is the same as that of the velocity vectors near each cell.

Equation (B-1) can be converted to the following finite difference form for application to a computational mesh:

$$r_{i,j}^{n+1} = r_{i,j}^n + C_A \Delta t [\bar{v}_{i,j}^n - \bar{u}_{i,j}^n \frac{(r_{i,j}^n - r_{i-1,j}^n)}{(x_{i,j}^n - x_{i-1,j}^n)}] \quad (B-2)$$

where

$$\bar{u}_{i,j}^n = 1/4 (u_{i-1,j}^n + u_{i+1,j}^n + u_{i,j-1}^n + u_{i,j+1}^n) \quad (B-3)$$

$$\bar{v}_{i,j}^n = 1/4 (v_{i-1,j}^n + v_{i+1,j}^n + v_{i,j-1}^n + v_{i,j+1}^n) \quad (B-4)$$

and where C_A is a constant used to damp the grid motion with respect to time. Spatial averaging of the velocity components is applied in order to reduce the effects of numerical velocity fluctuations at indi-

vidual mesh points in the flow. The upwind difference form of the cell aspect ratio term ($\Delta r / \Delta x$) is also utilized to achieve better stability in the finite difference equation.

Equation (B-1) is applied in the wake region of the flowfield for a line of constant η ($j=\text{constant}$), where the specific value of η corresponds to the nozzle inner wall for overexpanded flowfields, and to the nozzle outer wall for underexpanded flowfields. Once the position of this grid reference line is established, the fine mesh region corresponding to the wall thickness is computed. The exponential stretching scheme discussed in Chapter III is then applied for each value of ξ in the regions above and below the fine mesh region as shown in Figure 41. The first two grid points above the centerline were kept fixed at constant heights for all values of x . This prevented large numerical errors in axisymmetric cases involving the differencing of terms containing $(1/r)$, where r is a very small number.

The constant C_A was specified in the range of 0.3 - 0.6 in order to allow the grid to adapt smoothly as the solution converged. Larger values of C_A caused undesirable oscillatory motion of the grid reference line with respect to time.

The adaptive grid scheme was applied once during every iteration of the solution algorithm. The number of points allowed to "float" on the grid reference line could be varied during the course of the solution. This capability was utilized primarily during the start-up portion of the numerical solution, where only a limited number of points close to the nozzle were allowed to "float" until the shear layer was established. After the position of the shear layer across the complete

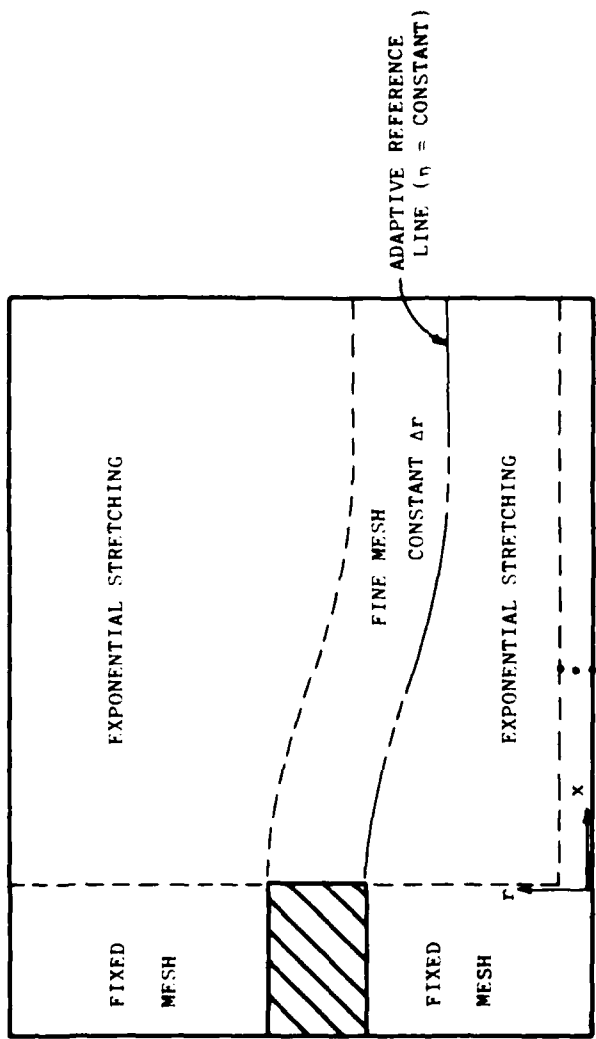


Figure 41. Adaptive Mesh Schematic.

computational domain was completely established, the adaptive grid scheme could be turned off in order to save computer time during the remainder of the solution.

APPENDIX C

TWO-DIMENSIONAL FLAT PLATE FAR WAKE SOLUTION

In order to test the validity of the turbulence model in the far wake region, a check case possessing known experimental data in this region was computed. The experimental data for this case is that of Toyoda and Hiriayama (33), which involved a two-dimensional thin flat plate at a Mach number of 1.60. The flat plate possessed a thickness of 1 mm and a trailing edge thickness of 0.1 mm.

The following flow quantities were given in the experimental data:

$$M_{\infty} = 1.60$$

$$P_{\infty} = 3.2 \text{ atm}$$

$$Re = 5300$$

A value for free stream stagnation temperature was not given experimentally. A stagnation temperature of 518.7°R was therefore assumed. Using the previous quantities, the value for the boundary layer momentum thickness at the trailing edge was computed as:

$$\delta_{TE} = .0895 \text{ mm}$$

The computational solution used the same numerical solver (MacCormack's explicit method) as that of the coflowing nozzle solutions. The eddy viscosity models utilized were identical with those used in the boundary layer and far wake regions of the coflowing nozzle. The boundary conditions utilized also closely resemble those of the coflowing nozzle. The inflow conditions were set by the experimental data and

remained fixed for the duration of the solution. The upstream u component of velocity near the trailing edge of the plate was matched to that of the experimental data as shown in Figure 42. Input conditions at the upstream boundary were then set as:

$$u(x_i, y, t) = 0.6295 u_\infty (y/\delta_{TE})^{1/5} \quad (C-1)$$

$$v(x_i, y, t) = 0.0 \quad (C-2)$$

$$\cdot(x_i, y, t) = r_\alpha / \{ 1 + \frac{(t-1)}{2} M_\alpha^2 [1 - (u(x_i, y, t)/u_\infty)^2] \} \quad (C-3)$$

$$P(x_i, y, t) = P_\infty \quad (C-4)$$

Both the upper and lower freestream boundaries utilize the characteristic condition applied at the upper boundary of the coflowing nozzle solutions. The outflow and wall boundaries used conditions identical to those utilized for the coflowing nozzle. The computational solution was initially started by applying the upstream profile across the computational domain:

$$T(x, z, 0) = T(x_1, y, 0) \quad (C-5)$$

This calculation utilized a 39x34 computational mesh, with exponential mesh stretching employed in both the x and y directions as shown in Figure 43. Minimum grid spacings in the x and y directions were 0.112mm and 0.100mm, respectively. The physical dimensions of the computational flowfield in the x and y directions were 38mm and 21mm, respectively. The rate of data processing on a CDC Cyber 175 computer was 0.0014 sec per grid point for each iterative time step. The solution was computed for a duration of four characteristic times (3200 iterations), at which time no significant change was detected in the dependent variables. The result was then taken to

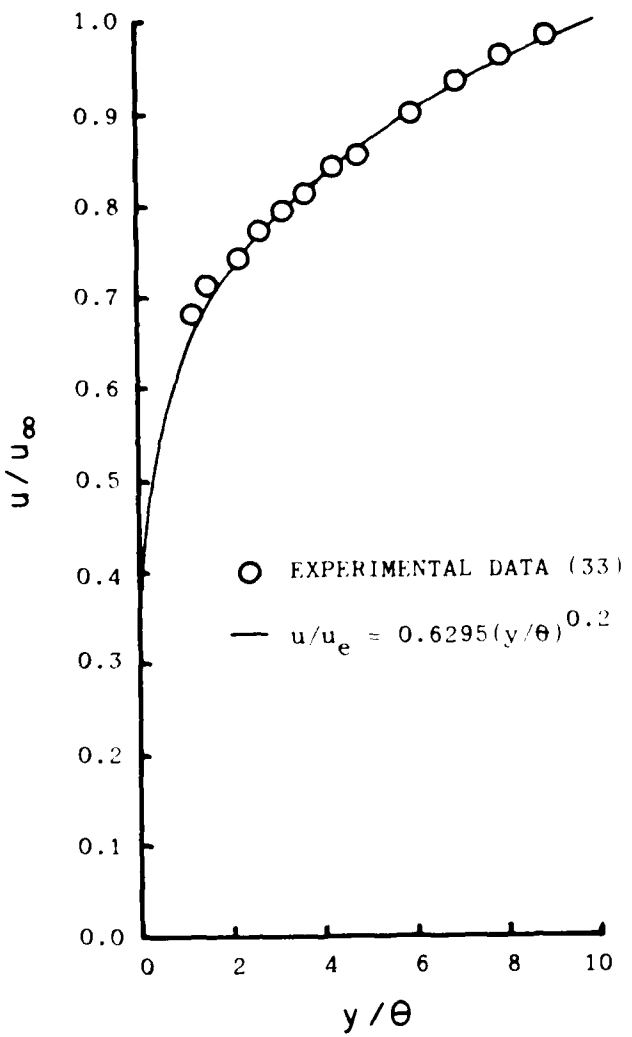


Figure 42. Velocity Profile at the Trailing Edge of the Two-Dimensional Flat Plate.

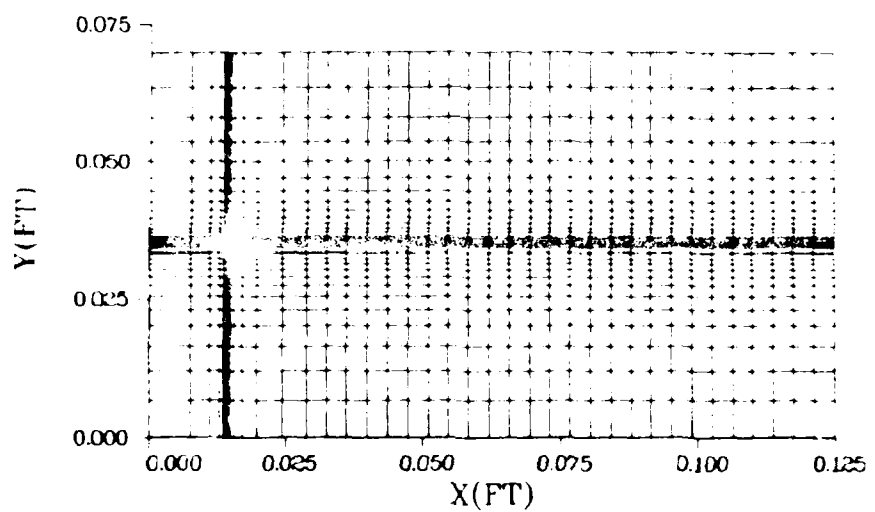


Figure 43. Computational Mesh Used in the Flat Plate Solution.

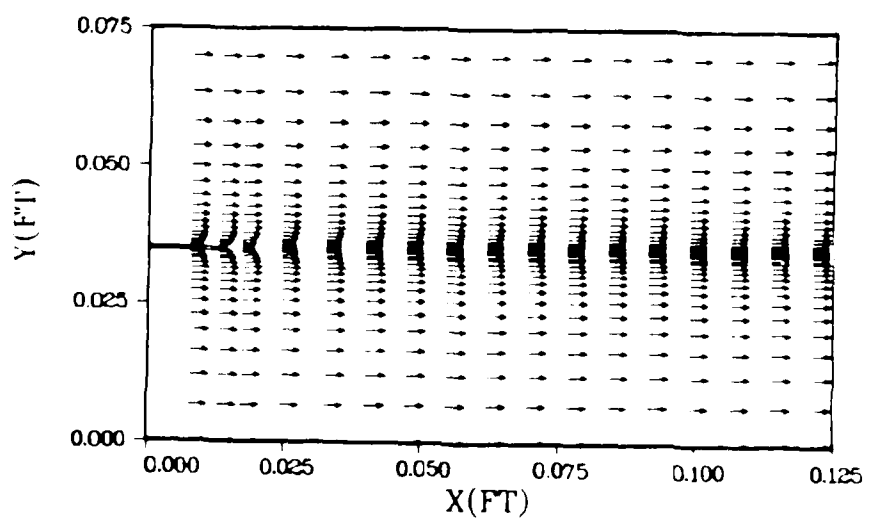


Figure 44. Computed Flat Plate Velocity Profile.

be the asymptotic solution.

The computational solution demonstrated that the eddy viscosity model gives good results in the far wake region. The maximum velocity defect generated computationally is in good agreement with the experimental data as shown in Figure 21. Figure 43 shows that the velocity field generated computationally evolves from the boundary layers on the plate to a classic wake solution very rapidly due to the turbulent nature of the flow.

APPENDIX D

TWO-DIMENSIONAL WEDGE-FLAT PLATE NEAR WAKE SOLUTION

In order to test the validity of the turbulence model utilized in the near wake region of the coflowing nozzle solutions, a check case exhibiting similar physical characteristics and possessing known experimental data in this region was solved numerically. The experimental case selected for this validation study is one obtained by Rom, Seginer and Kronzon (35) for a two-dimensional wedge-flat plate in a turbulent supersonic flowfield. The model used for this study consisted of a sharp 15° half angle wedge-flat plate with a base height of 10 mm and a chord of 44 mm. The following flow conditions were given in the experimental data:

$$M_{\infty} = 2.25$$

$$Re_c = 1.5 \times 10^6$$

$$P_{O_{\infty}} = 40 \text{ psig}$$

$$T_{O_{\infty}} = 492^\circ \text{ R}$$

A computed adiabatic wall temperature of 466.6° R based on the flow condition at the flat plate portion of the model was used in the computational solution.

The numerical solution used the same computational solver and turbulence model as that of the coflowing nozzle solutions. The boundary and initial conditions were also identical to those used in the coflowing nozzle with the exception of the jet centerline condition. As shown in Figure 45, this condition was replaced with a lower freestream boundary which utilized a characteristic scheme similar to that of the upper freestream boundary. Since a value for

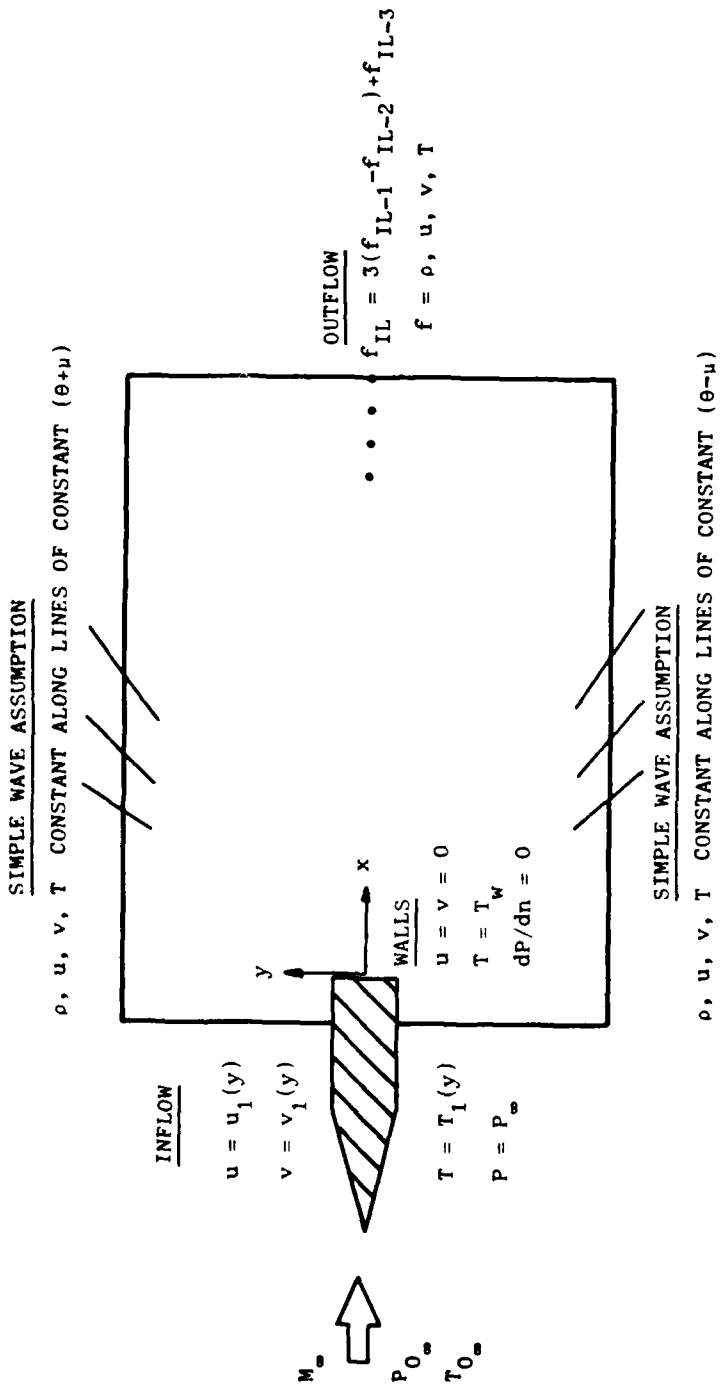


Figure 45. Computational Boundary Conditions for the Two-Dimensional Wedge-Flat Plate.

the boundary layer thickness near the trailing edge was given experimentally ($\delta/h = 0.15$), a two-dimensional boundary layer code was used to generate the velocity and temperature profiles on the upstream boundary. The boundary layer starting length was adjusted to give the correct boundary layer thickness. One additional condition was imposed on the line of symmetry for the wedge ($j = 23$). At this line of symmetry, a zero v velocity component was enforced to help stabilize the wake during the startup of the numerical solution and help accelerate convergence by damping any numerical shear layer oscillations in the wake.

The solution was calculated using a 45×45 point computational mesh with exponential stretching employed in both the x and y directions as shown in Figure 46. The physical dimensions of the computational flowfield in the x and y directions were 10cm and 7cm, respectively. Minimum grid spacing in the x and y directions was set at 0.5 mm. This gave a value of $u/u_e = 0.83$ for the first point in the boundary layer above the nozzle wall, which corresponds to an identical value in the jet boundary layer of the coflowing nozzle solutions. Thus, truncation error should be similar in this region for both the wedge-flat plate and the coflowing nozzle. The rate of data processing on a CDC Cyber 175 computer was 0.0014 sec per grid point for each iterative time step. The solution was allowed to progress for approximately four characteristic timesteps at which time the change in the dependent variables was less than 0.5% per characteristic time period. This condition was then considered to be the converged asymptotic solution.

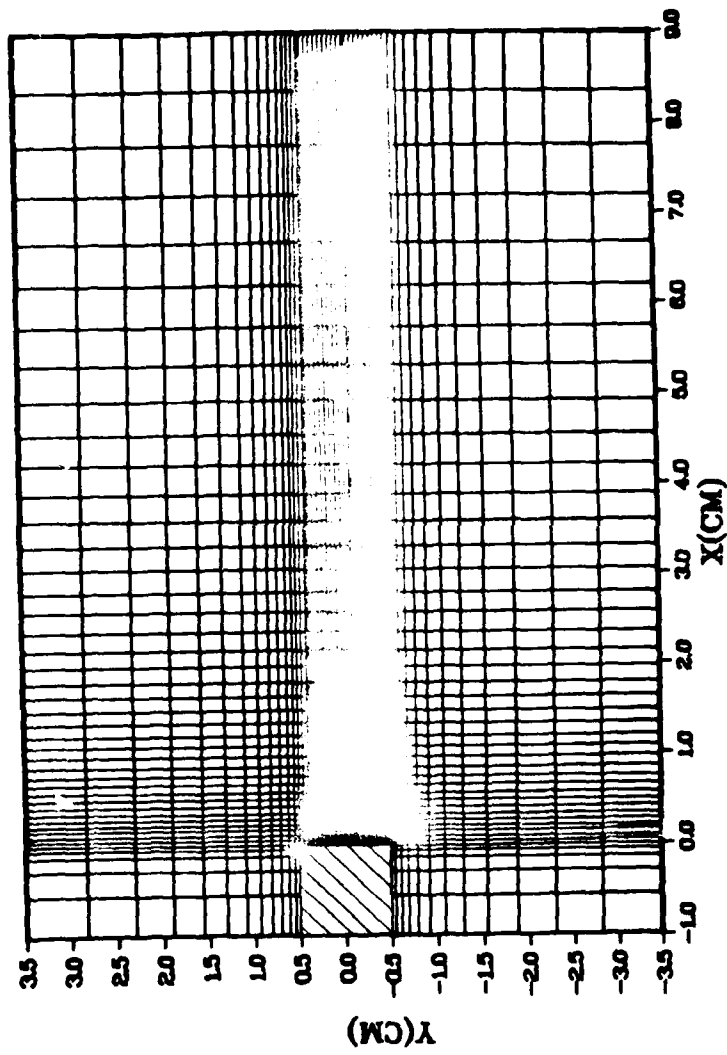


Figure 46. Computational Mesh used for the Two-Dimensional Wedge-Flat Plate Solution.

Specific features of the experimental flowfield in the near wake were reproduced in the computational solution and can be distinguished in the plots of Mach number contours and velocity profiles shown in Figures 47 and 48. Several flow features which were numerically observed include the existence of the boundary layers along the horizontal walls of the body, the turning of the flow through the corner expansion fans, the existence of the subsonic recirculating "dead water" region adjacent to the base of the body, flow recompression through the trailing shocks, and the evolution of the wake to a classic far wake flow. The weak lip shock evident in the experimental data was not readily evident in the numerical solution. This may be attributed to the fact that the numerical method tends to smear shocks, and thus has difficulty locating shocks which are very weak.

Quantitative accuracy of the numerical solution is identified through the use of the given experimental static pressure and pitot pressure data. A comparison of the axial static pressure distribution along the line of symmetry is shown in Figure 49. The computed static pressure distribution is within 5% of the measured values except in the region of recirculating flow ($x \leq 1.0\text{cm}$), where there is up to a 7% discrepancy between the experimental and computed values. However, static pressure probes like the one used to obtain the data are very sensitive to flow angularity, and thus less reliable in areas of recirculating flow. A more reliable comparison is that of the pitot-pressure surveys shown in Figure 50. These measurements are less susceptible to errors resulting from flow angularity. This

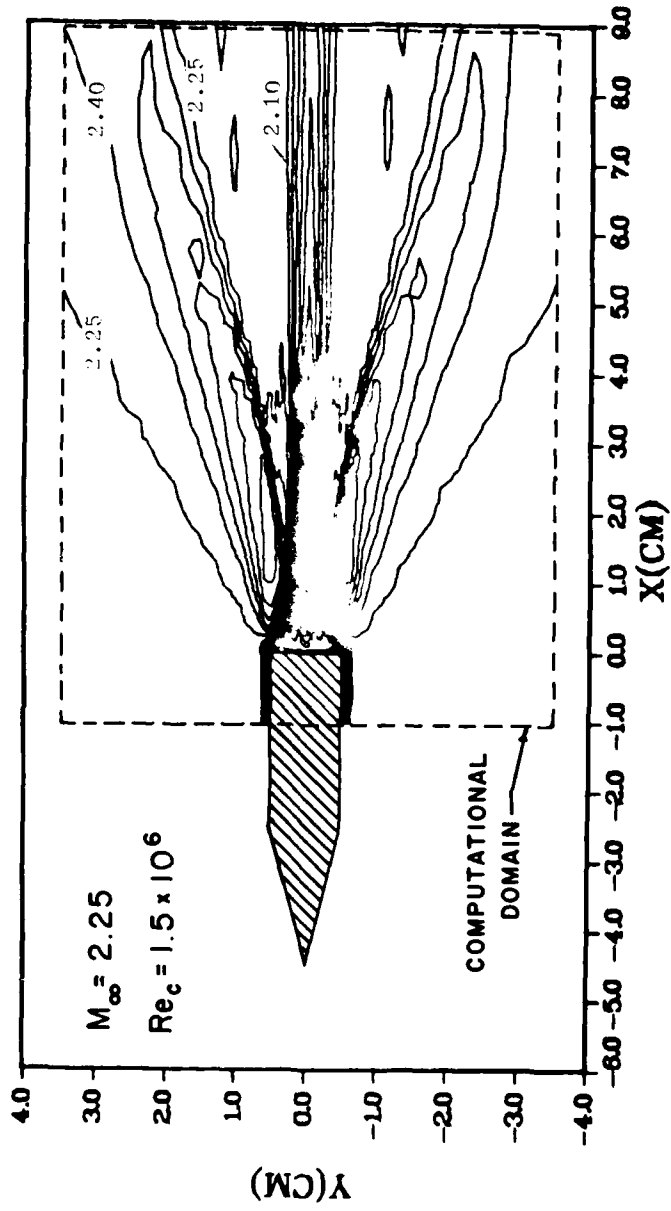


Figure 47. Two-Dimensional Wedge-Flat Plate with the Computed Mach Number Contours Shown.

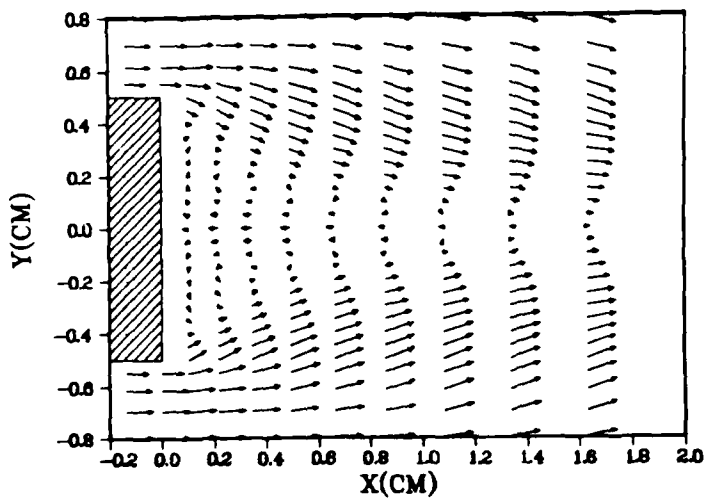


Figure 48. Computed Velocity Profiles in the Near Wake of the Two-Dimensional Wedge-Flat Plate.

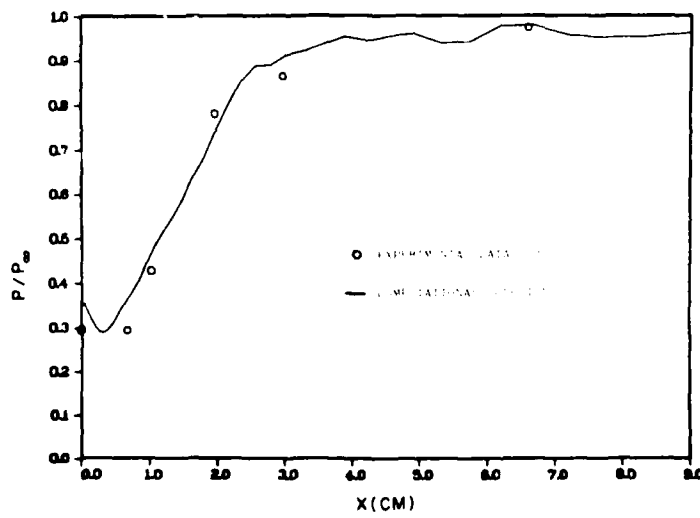


Figure 49. Static Pressure Along the Line of Symmetry in the Near Wake of the Two-Dimensional Wedge-Flat Plate.

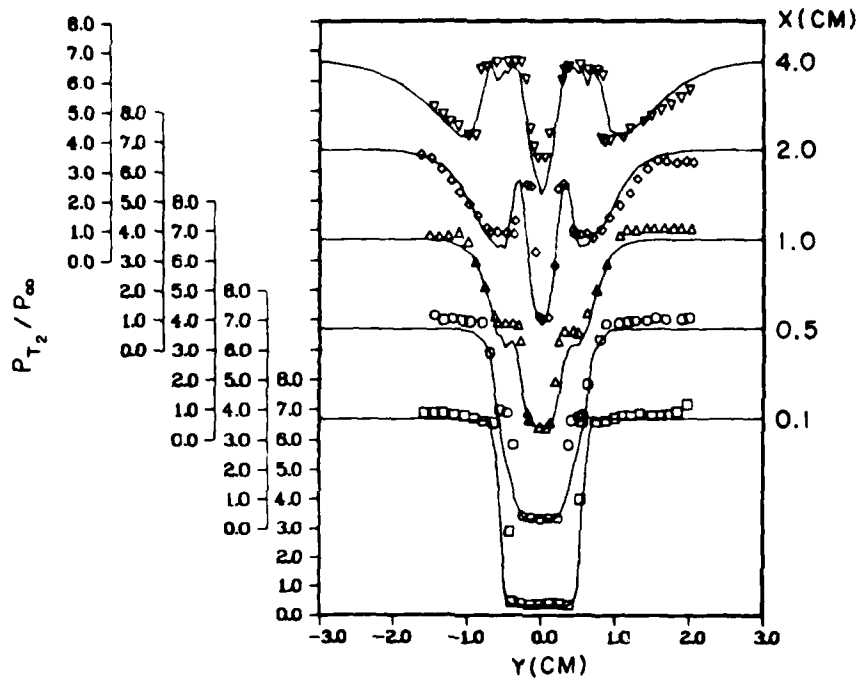


Figure 50. Pitot Pressure Profiles in the Near Wake of the Two-Dimensional Wedge-Flat Plate (Symbols - Experimental Data(34), Solid Lines - Computational Solution).

figure shows excellent agreement in the "deadwater" region of recirculating flow. The numerical solution smears the weak beginning of the recompression trailing shocks at 0.5cm, but correctly simulates them at the correct values further downstream ($x \geq 1.0$). This figure particularly demonstrates that the phenomena present in the near wake are accurately simulated by the present computational method and turbulence modeling.

APPENDIX E

AXISYMMETRIC COFLOWING NOZZLE SOLUTION SIMULATING INTERNAL SEPARATION OF THE NOZZLE

The peculiar reversal in the nozzle base pressure coefficient as the pressure ratio was lowered below $P_j/P_\infty = 0.18$ was believed to be caused by separation in the nozzle (Fig. 38). This was further substantiated through an examination of the schlieren photographs (16) which show a definite change in flow character near this value (Fig. 39). To test this hypothesis a numerical solution was computed for a case where the jet total pressure corresponded to that of the attached strong shock solution ($P_j/P_\infty = 0.15$), but where the jet Mach number equals 2.60 based upon an isentropic expansion in the nozzle. For this jet Mach number a reduction in nozzle area ratio was assumed from $A/A^* = 4.2$ at Mach 3 to $A/A^* = 2.9$ at Mach 2.60. This reduced expansion rate was intended to roughly simulate the effects of boundary layer separation in the nozzle, while retaining grid geometry and fineness identical to the previously calculated attached jet flow case.

The following jet flow parameters were used in this solution:

$$M_j = 2.60$$

$$T_{oj} = 580.5^\circ R$$

$$P_{oj} = 1636 \text{ psf}$$

These jet conditions produce an actual nozzle pressure ratio of $P_j/P_\infty = 0.276$ versus the calculated value of $P_j/P_\infty = 0.150$ which was assumed in Reference 16.

This solution was initialized using the solution for the attached strong shock case with a calculated nozzle pressure ratio equal to

115. Except for the upstream jet boundary, boundary conditions and mesh configuration identical to those of the attached case were utilized. At the upstream jet boundary the following velocity profile was fixed:

$$\begin{aligned} u &= 2002 \text{ ft/sec} & 0 \leq r/r_{jet} \leq 0.835 \\ u &= 0 & 0.835 < r/r_{jet} \leq 1 \\ v &= 0 & 0 \leq r/r_{jet} \leq 1 \end{aligned}$$

As shown in Figure 51, this velocity input profile increased the displacement thickness of the jet boundary layer in rough approximation to that caused by separation in the nozzle. In this case the jet flow is assumed to be turbulent in nature.

As shown in Figure 52, a strong shock solution was obtained, with a reflection length of $x_s/r_{jet} = 1.29$, about 2% greater than the experimental value at this jet total pressure case. The base pressure coefficient obtained was equal to -0.264, about 8% less than the experimental value and in much better agreement than that of the attached jet boundary layer case.

Although discrepancies in this solution such as the smaller diameter of the computational Mach disc and the appearance of a physically nonexistent secondary Mach disc further downstream are apparent, this case does demonstrate that separation and its effect on the flow expansion in the nozzle can significantly impact the resultant base pressure coefficient of the nozzle. Therefore, future computations for low pressure ratios should commence at the throat section to insure that nozzle separation is properly considered.

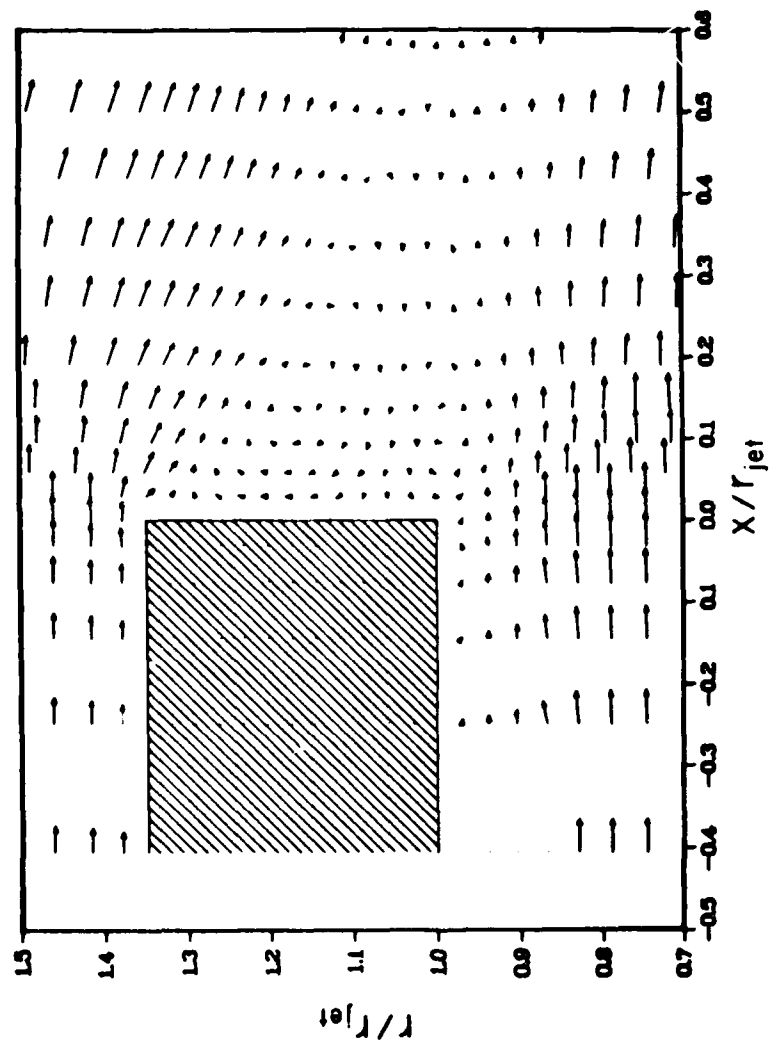


Figure 51. Computed Velocity Profiles Near the Nozzle Annulus for the Separated Flow Simulation.

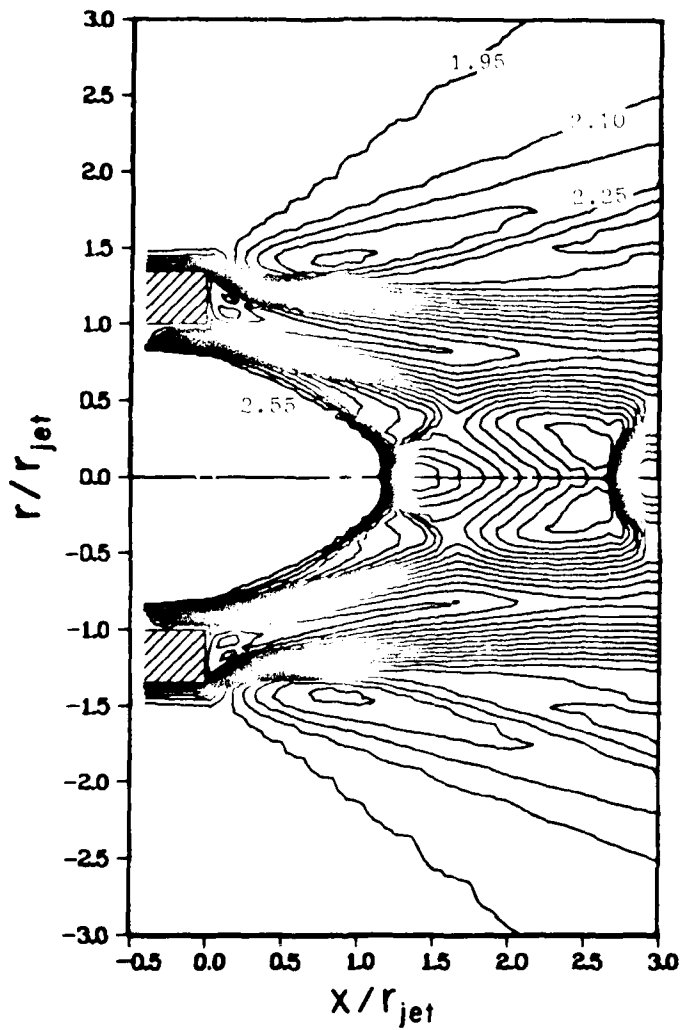


Figure 52. Computed Mach Number Contours for the Separated Flow Simulation.

APPENDIX F

INVESTIGATION OF NUMERICAL ERROR

Two error analyses were performed on the numerical technique used to obtain solutions for the coflowing nozzle. The first consisted of examining the error generated by the numerical algorithm used to solve the Navier-Stokes equations. The second was a study of the effect of repositioning first the downstream boundary, and subsequently the upper boundary to regions containing only minor flow gradients normal to each boundary. These analyses are discussed in detail in the following sections.

Truncation Error Analysis

MacCormack's explicit finite difference algorithm is an equivalent second order accurate numerical solver. The final converged solution for any case computed by this algorithm should then satisfy the Navier-Stokes equations at all interior node points with second order accuracy. A numerical check on this accuracy was conducted using a typical converged solution and the following procedure.

As shown in Chapter 2, the axisymmetric Navier-Stokes equations can be written as:

$$\frac{\partial U}{\partial t} + \frac{\partial F}{\partial x} + \frac{1}{r} \frac{\partial (rG)}{\partial r} - \frac{H}{r} = 0 \quad (F-1)$$

A nondimensionalized finite difference formulation of these equations can then be written as:

$$\left(\frac{t_c}{U_\infty} \right) \frac{\Delta U}{\Delta t} + \frac{t_c}{U_\infty} \left[\frac{\Delta F}{\Delta x} + \frac{1}{r} \frac{\Delta (rG)}{\Delta r} - \frac{H}{r} \right] = E = \text{Error} \quad (F-2)$$

where U_∞ is defined as:

$$U_\infty = \begin{bmatrix} P_\infty \\ \rho_\infty u_\infty \\ \rho_\infty v_\infty \\ \rho_\infty e_\infty \end{bmatrix} \quad (F-3)$$

and $t_c = 5 \times 10^{-6}$ sec is set to insure that the lead terms on the left hand side of equation (F-2) are of order one.

The particular check case selected was that containing the strong Mach disc shock structure ($P_j/P_\infty = 0.150$), since this case contains both substantial regions of subsonic and supersonic flow, and oblique as well as normal shock waves. The MacCormack solution for this case was used as input for equation (F-3), where the left hand side of the equation was computed at all interior grid points using a standard two-dimensional second order central differencing scheme applied on the transformed computational plane. The magnitude of the Error vector (E) is then an indication of how close MacCormack's method is to an alternate second order accurate solver. The following root mean square (RMS) values of E were obtained over the interior of the computational domain:

$$E_{rms} = \begin{bmatrix} E_p \\ E_{pu} \\ E_{pv} \\ E_pe \end{bmatrix} = \begin{bmatrix} 0.026 \\ 0.020 \\ 0.011 \\ 0.026 \end{bmatrix}$$

This result indicates that over the domain, MacCormack's algorithm and the two-dimensional difference scheme are equivalent to within three percent.

Finally, the Error vector E was examined over the computational domain to determine which regions generated the highest magnitude of error. Since the RMS error value of the continuity equation was one of the largest, and the error distribution was representative of that in the other equations, it is shown in Figure 53. In this figure, only error values greater than the RMS value are shown as contours. Regions containing the largest error consist of those containing shock waves and that containing the expansion fan near the sharp corner of the nozzle. In these shock regions, strong flow gradients exist over areas with fairly coarse finite difference mesh spacing. Although the wake region also contains strong gradients within the mixing layer, it lies within a fine mesh region of the grid that produces much less numerical error.

This analysis further demonstrates the desirability of utilizing adaptive mesh schemes that can align the grid with flow gradients as the solution progresses to convergence.

Boundary Position Analysis

Although the upstream boundary, the centerline boundary, and the position of the nozzle walls were fixed by the definition of the problem to be solved, the placement of both the downstream boundary and the upper boundary was left to the discretion of the computational investigator. It was desirable to place these boundaries as close to the nozzle as possible in order to achieve computational efficiency in a compact domain. In the coflowing nozzle solutions, both of these boundaries were located in regions in which flow gradients existed due to the presence of shock and expansion waves and viscous phenomena such as shear layers and wakes in the flowfield. The assumption is made that

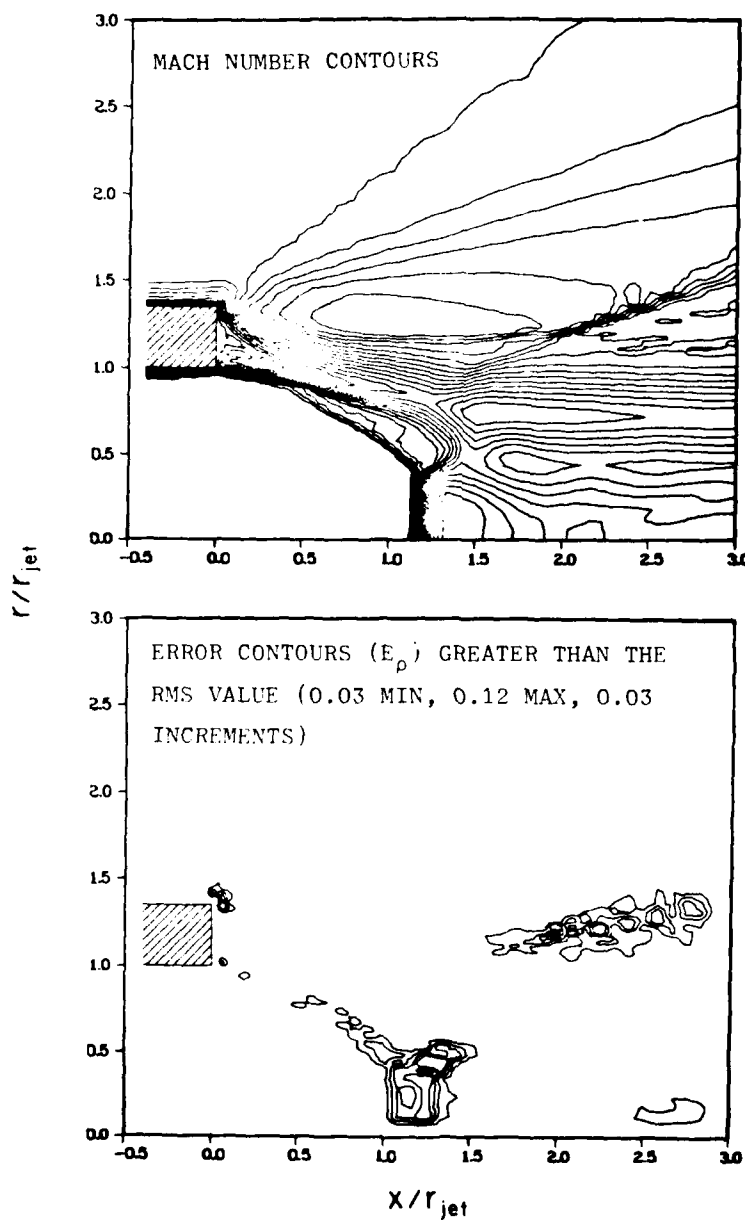


Figure 53. Comparison Between the Computational Solution and the Error Present in the Continuity Equation, $P_j/P_\infty = 0.150$.

positioning these two boundaries in flow gradient regions does not affect the computational solutions obtained. To validate this assumption, each of these boundaries was repositioned a greater distance from the nozzle to regions containing only minor flow gradients normal to each boundary. The resulting effect on the shock wave structure as well as on the nozzle base pressure coefficient in the numerical solution was then observed.

The coflowing nozzle case for which $P_j/P_\infty = 0.251$ was examined for this particular study. The downstream boundary contains primarily supersonic outflow with an embedded wake region of subsonic outflow. The downstream boundary was extended from its original position at $x/r_{jet} = 3.0$ to a new value of $x/r_{jet} = 6.0$. This stretching was achieved by the addition of twelve grid points axially to the original mesh. The outflow at this new position was totally supersonic in nature with only minor gradients in existence normal to the boundary. As shown in Figure 54, no changes were evident in the shock structure contained in the original domain. The computational base pressure coefficient remained unchanged at a value of $p_B = -0.299$.

The effect of repositioning the upper boundary to a radial distance at which flow gradients are not present was then examined. The upper boundary of the axially stretched case was extended from its original value of $r/r_{jet} = 3.0$ to a new value of $r/r_{jet} = 6.0$ as shown in Figure 55. In this case eight grid points were added radially to the axially stretched mesh. Again, no changes were evident in the numerical shock structure, and the computational value of the nozzle base pressure coefficient remained at $p_B = -0.299$.

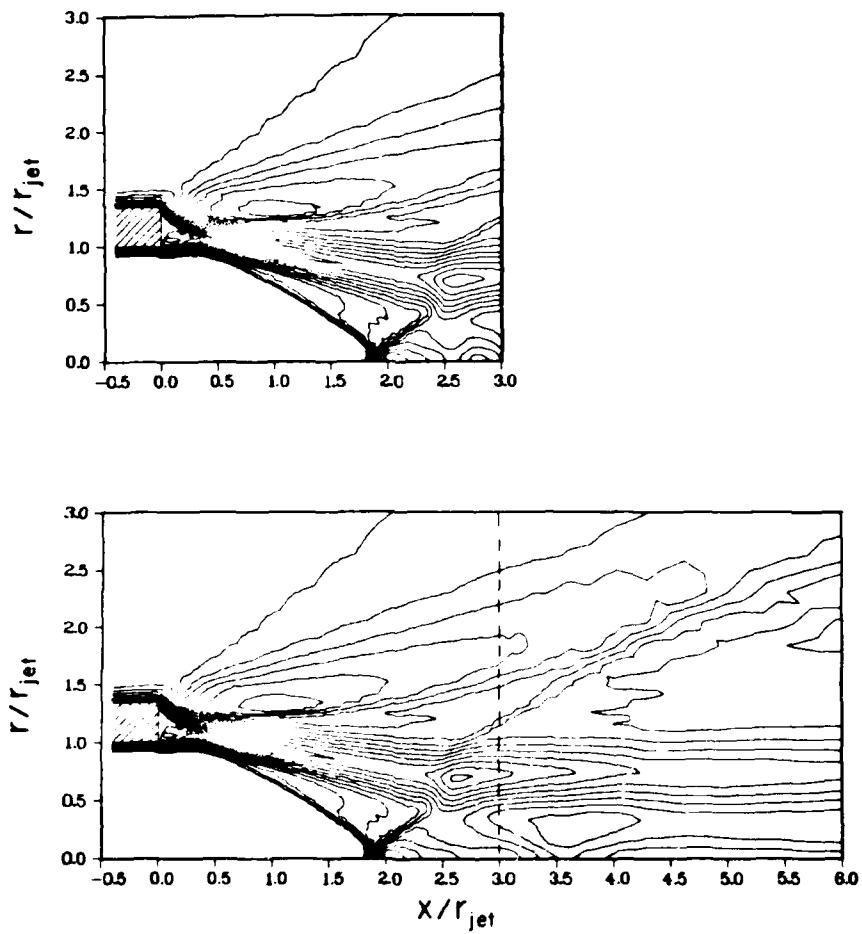


Figure 54. Extension of the Downstream Boundary Showing Computed Mach Number Contours, $P_j/P_\infty = 0.251$.

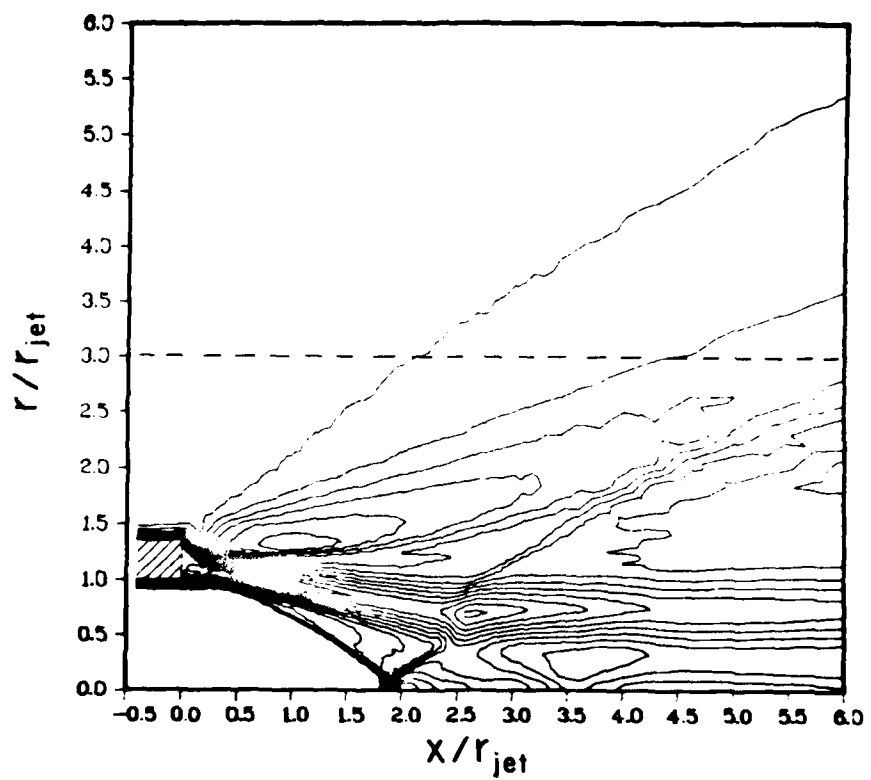


Figure 55. Extension of the Upper Boundary Showing Computed
Mach Number Contours, $P_j/P_\infty = 0.251$.

Since repositioning these boundaries had essentially no effect on the computational solution that was examined, the application of these boundary conditions in the original regions containing mixed supersonic-subsonic flow on the outflow boundary and substantial flow gradients on both boundaries was valid.

VITA

Gerald Alan Hasen was born on 19 April 1948 in Toledo, Ohio. He graduated from Pueblo High School in Tucson, Arizona in 1966 and attended the University of Arizona from which he received the degree of Bachelor of Aerospace Engineering in January 1971. Upon graduation, he was commissioned in the USAF through the ROTC program. He continued his education in the Graduate School of the University of Arizona and received a Master of Science in Aerospace Engineering Degree in January 1972. He was called to active duty in March 1972 as an aerodynamic propulsion systems analyst for the Foreign Technology Division, WPAFB, Ohio. He was married to Diane Lynn Youngs of Springfield, Ohio on 27 June 1975. He served as an aircraft propulsion performance engineer for the Aeronautical Systems Division, WPAFB, Ohio from July 1975 until his entry into the School of Engineering, Air Force Institute of Technology in August 1976. He is currently assigned to the Air Force Wright Aeronautical Laboratories as a computational aerodynamicist for the Computational Aerodynamics Group of the Flight Dynamics Laboratory.

Permanent Address: 111 N. Ann Street
Reading, Michigan 49274

UNCLASSIFIED

SECURITY CLASSIFICATION OF THIS PAGE (When Data Entered)

REPORT DOCUMENTATION PAGE		READ INSTRUCTIONS BEFORE COMPLETING FORM
1 REPORT NUMBER AFIT/DS/AA/81-2	2 GOVT ACCESSION NO. <i>AD-A100 827</i>	3 RECIPIENT'S CATALOG NUMBER
4 TITLE (and Subtitle) NAVIER-STOKES SOLUTIONS FOR A SUPERSONIC COFLOWING AXISYMMETRIC NOZZLE WITH A THICK BASE ANNULUS	5 TYPE OF REPORT & PERIOD COVERED PhD Dissertation	
7 AUTHOR(s) Gerald A. Hasen Captain, USAF	6 PERFORMING ORG. REPORT NUMBER	
9 PERFORMING ORGANIZATION NAME AND ADDRESS Air Force Institute of Technology (AFIT-EN) Wright-Patterson AFB, Ohio 45433	10 PROGRAM ELEMENT PROJECT, TASK AREA & WORK UNIT NUMBERS Project 2307-N6-03	
11. CONTROLLING OFFICE NAME AND ADDRESS Flight Dynamics Laboratory (AFWAL/FIRM) Air Force Wright Aeronautical Laboratories Wright-Patterson AFB, Ohio 45433	12 REPORT DATE April 1981	
14 MONITORING AGENCY NAME & ADDRESS (if different from Controlling Office)	13. NUMBER OF PAGES 159	
	15 SECURITY CLASS. (of this report) Unclassified	
	16a. DECLASSIFICATION DOWNGRADING SCHEDULE	
16. DISTRIBUTION STATEMENT (of this Report) Approved for public release; distribution unlimited		
17. DISTRIBUTION STATEMENT (of the abstract entered in Block 20, if different from Report) APPROVED FOR PUBLIC RELEASE AFR 190-17. APPROVED FOR PUBLIC RELEASE AFR 190-17.		
18. SUPPLEMENTARY NOTES		
19. KEY WORDS (Continue on reverse side if necessary and identify by block number) Navier-Stokes Numerical Solutions Axisymmetric Nozzle Mach Disc		
20. ABSTRACT (Continue on reverse side if necessary and identify by block number) Numerical solutions of the Navier-Stokes equations are obtained for a super-sonic coflowing axisymmetric nozzle ($M_\infty = 1.94$, $M_j = 3.0$, $Re_\infty = 2.2 \times 10^6$). Five jet pressure ratio conditions ranging from a highly overexpanded case which exhibits a Mach disc shock formation to a slightly underexpanded case are examined and solved numerically. MacCormack's explicit method is applied as the numerical algorithm. An adaptive grid is utilized in the nozzle wake to allow the fine mesh region of the computational grid to remain in areas containing relatively high flow gradients. Locally dependent eddy viscosity		

UNCLASSIFIED

SECURITY CLASSIFICATION OF THIS PAGE (When Data Entered)

modelling is applied in the form of a Cebeci-Smith two layer model in the boundary layer region on the nozzle walls, and a form of the Prandtl mixing length model in the nozzle wake. A two-dimensional wedge-flat plate validation case was computed using these models with good results. The computational results for the coflowing nozzle accurately reproduced the experimentally observed viscous effects on the nozzle base pressure and shock locations that are caused by the thick nozzle base annulus. Correct transition was achieved numerically from regularly reflected shock waves at the line of symmetry in the jet core to the Mach disc reflection at the appropriate nozzle pressure ratio.

UNCLASSIFIED

SECURITY CLASSIFICATION OF THIS PAGE (When Data Entered)

